



HAL
open science

Monte Carlo simulations and experimental characterizations of air microplasma inducing poration of cell membranes for gene transfection

Amel Zerrouki

► **To cite this version:**

Amel Zerrouki. Monte Carlo simulations and experimental characterizations of air microplasma inducing poration of cell membranes for gene transfection. Plasmas. Université Paul Sabatier - Toulouse III, 2016. English. NNT : 2016TOU30128 . tel-01489644

HAL Id: tel-01489644

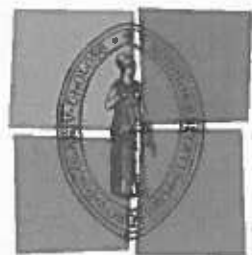
<https://theses.hal.science/tel-01489644>

Submitted on 14 Mar 2017

HAL is a multi-disciplinary open access archive for the deposit and dissemination of scientific research documents, whether they are published or not. The documents may come from teaching and research institutions in France or abroad, or from public or private research centers.

L'archive ouverte pluridisciplinaire **HAL**, est destinée au dépôt et à la diffusion de documents scientifiques de niveau recherche, publiés ou non, émanant des établissements d'enseignement et de recherche français ou étrangers, des laboratoires publics ou privés.

Université Fédérale



Toulouse Midi-Pyrénées

THÈSE

En vue de l'obtention du

DOCTORAT DE L'UNIVERSITÉ DE TOULOUSE

Délivré par :

Université Toulouse 3 Paul Sabatier (UT3 Paul Sabatier)

Cotutelle internationale avec "Ehime University, Japon "

Présentée et soutenue par :

Amel ZERROUKI

le lundi 29 août 2016

Titre :

SIMULATIONS MONTE CARLO ET CARACTERISATIONS D'UN MICROPLASMA
D'AIR INDUISANT LA PORATION DE MEMBRANES CELLULAIRES POUR LA
TRANSFECTION DE GENES

École doctorale et discipline ou spécialité :

ED GEET : Ingénierie des PLASMAS

Unité de recherche :

Laboratoire PLAsma et Conversion d'Énergie (LAPLACE), UMR 5213

Directeur/trice(s) de Thèse :

M. Yousfi, Directeur de Recherche au CNRS, LAPLACE Toulouse

M. Jinno Professeur à Ehime University, Plasma Science, Japon

Jury :

K. Kadowaki	Professeur à Ehime University, HV Engineering, Japon	Président
S. Shimomura	Professeur à Ehime University, Nano Electronics, Japon	Examineur
P. Bertoncini	MC HDR à Université de Nantes, IMN, France	Rapporteur
A. Talneau	Directeur de Recherche au CNRS, LPN, Marcoussis, France	Rapporteur
A. Rhallabi	Professeur à Université de Nantes, IMN, France	Co-encadrant
G. Zissis	Professeur à Université Paul Sabatier de Toulouse, France	Invité
M. Yousfi	DR au CNRS, LAPLACE, Toulouse, France	Directeur de thèse
M. Jinno	Professeur à Ehime University, Plasma Science, Japon	Co-Directeur de thèse

ABSTRACT

Gene transfection is a technique of deliberately introducing DNA into cells through the membrane. The cold atmospheric plasma CAP is potentially a new alternative, safe and damage-free technique. It can lead to a transient permeabilization of the cell membrane allowing processes of gene transfection in which DNA and cells are both exposed to fluxes of active plasma species (electrons, ions, and neutral radicals). The mechanisms of more particularly membrane poration are far to be clear and controlled. Therefore, the aim of this thesis is to numerically study the mechanisms of plasma-induced membrane permeabilization using a specific micro-air plasma. More precisely, is to develop and exploit a specific Monte Carlo poration model. This model is aimed to simulate the pore formation of few nm of width through cell membranes when irradiated by micro-air plasma. This developed model requires a prior input data on the density of charged particles and the temperature of gas and electrons. Thus, an experimental characterisation by OES of the micro-air corona discharge is performed. Rotation temperature was determined (between 700K to 2350K) even though under our non-equilibrium conditions T_g remains ~ 300 K. OES also has given the space variation from the high voltage tip to the grounded plate of vibration temperatures (between 3000K up to about 6500K) and T_e (about 6.75 eV down to 3.4 eV near the plate). A magnitude around 10^{15}cm^{-3} for the electron and ion densities have been also determined. Moreover, knowing that there are no literature simulations devoted to membrane permeabilization and pore formation when impacted by plasma actives species, we developed for the first time in literature a specific Monte Carlo poration model. In this framework, we assumed each plasma species (electrons, ions, and neutral radicals) as a super-particle grouping a large number of particles. The species fluxes were estimated from a plasma reaction kinetic model and OES study. The membrane layers were assumed as a simple membrane model superposing four layers of phospholipids and proteins. Each layer was constituted by a succession of super-sites subjected to specific super-processes (recombination, reflection, activation of a site, opening, etc). For an accurate exploitation of our model, the estimation of the probability of occurrence of the whole considered super-processes is absolutely necessary. Thus, a large parametric study is conducted. The aim is to evaluate the effects of the initial simulation parameters as well as the magnitude of the occurrence probabilities of each reaction process on pore formation. Several important results are emphasized. First, energetic electrons play a main role on site activations and openings due their strong anisotropy in the forward direction. In addition, due to their lower energy close to background gas, reflection processes due to ions, and radicals, have shown their role to widen and deepen the pore dimensions. Overall, it is more particularly shown that the initial particle number Np is the most efficient parameter of the membrane poration. We observed a direct correlation between Np and the exposure time of the cell membrane to the microplasma. This means that Monte Carlo poration model is an interesting tool of the prediction of the optimal exposure time versus the input data of the low-temperature plasma parameters, the cell membrane structure and the needed pore sizes. Under the specific chosen simulation conditions coming from the parametric study, it is shown a dynamics of formation of membrane pores having dimensions pore (diameters ~ 10 nm) compatible for the gene transfection. Our Monte Carlo simulation results are qualitatively validated from a first comparison with the measured transfected efficiency of DNA plasmid and the surviving cell rate in the case of mouse fibroblast cells. The present Monte Carlo method is, therefore, a very promising tool for a better understanding of the plasma gene transfection mechanisms.

RÉSUMÉ

La transfection est le processus de transfert de gènes (ADN) dans des cellules. L'utilisation des plasmas froids à la pression atmosphérique est un excellent vecteur pour la transfection de gènes. Cela peut conduire à une perméabilisation temporaire de la membrane cellulaire permettant ainsi le processus de transfection de gènes, dans lequel l'ADN et les cellules sont exposées aux flux des espèces actives du plasma (électrons, ions et radicaux neutres). Cependant beaucoup de questions restent sans réponse notamment sur les mécanismes de transfection par plasma, en particulier de formation de pores et de perméabilisation de la membrane par interactions avec les espèces actives du plasma. Ainsi, nous avons développé un modèle Monte Carlo simulant la formation de pores de quelques nm de largeur sous l'effet d'un microplasma d'air. Ce modèle nécessite a priori des données d'entrées sur la densité des espèces chargées et la température du gaz et des électrons. C'est pourquoi nous avons aussi effectué une caractérisation expérimentale par spectroscopie d'émission optique OES de la micro décharge couronne. On a estimé les températures rotationnelles de plusieurs espèces variant entre (700K-2350K) même si dans nos conditions de plasma hors équilibre la température du gaz demeure $\sim 300\text{K}$. Les variations spatiales de la température vibrationnelle T_{vib} et des électrons T_e le long de l'espace inter-électrode (de la pointe vers l'électrode de masse) ont aussi été estimées (T_{vib} :3000K-6500K et T_e :6.75 eV-3.4eV). Les densités des ions et des électrons ont été déterminées et valent environ 10^{15} cm^{-3} . Par ailleurs, sachant qu'il n'existe dans la littérature aucune modélisation consacrée à la perméabilisation de la membrane et la formation de pore par interactions avec les espèces actives du plasma, nous avons développé pour la première fois dans la littérature un modèle spécifique de simulation Monte Carlo pour la poration. Chaque espèce du plasma (électrons, ions, neutres radicaux) est considérée comme une macro-espèce (ou super-particule) représentant un grand nombre de particules. La proportion des espèces du plasma arrivant sur la membrane est estimée à partir de leurs flux, calculés à l'aide d'un modèle de cinétique réactionnelle et par mesures spectroscopiques. La membrane est supposée comme une simple structure multicouche de phospholipides et protéines. Les interactions avec les couches membranaires sont considérées comme étant des super-processus (recombinaison, réflexion, activation, ouverture). Une probabilité d'occurrence de chacun de ces super-processus est assignée à chaque super-particule sur la base d'une étude paramétrique. Le but est d'évaluer les effets des paramètres de simulation initiaux ainsi que l'effet des probabilités d'occurrence de chaque processus sur la formation de pores. Plusieurs résultats importants ont été obtenus. Les électrons jouent un rôle principal sur l'activation et l'ouverture des sites dus à leur forte anisotropie dans la direction avant. Malgré les faibles énergies, proche de celle du gaz, des ions et des radicaux, leur processus de réflexion est déterminant pour élargir et approfondir les dimensions des pores. Il a été montré que le nombre initial de particules N_p est le paramètre qui contrôle le plus efficacement la formation de pores. De plus, nous avons observé une corrélation directe entre N_p et la durée d'exposition de la membrane cellulaire au plasma. Dans les conditions actuelles de simulation, on a obtenu une dynamique de formation de pores avec des dimensions (diamètres $\sim 10\text{nm}$) compatibles pour la transfection de gènes. Les résultats de simulation Monte Carlo ont été qualitativement validés par une comparaison préliminaire avec les mesures des taux de transfection d'ADN et de survie de cellules fibroblaste de souris. La méthode de Monte Carlo développée dans ce travail représente un outil très prometteur pour une meilleure compréhension des mécanismes de transfection de gènes par plasma.

Acknowledgments

This Ph. D thesis was carried out in the framework of NESSIE exchanges program in a partnership with the Graduate School of Science and Engineering Ehime University (Matsuyama, Japan) and University Paul Sabatier (Toulouse, France). Moreover, it was under an agreement of an international joint supervision between Ehime University and Université Paul Sabatier. More precisely this thesis was achieved within the Electrical Energy Conversion Laboratories (EECL) and Laboratoire de Plasma et Conversion d'Energie (LAPLACE) under the supervision, respectively, of Masafumi JINNO, Professor at Ehime University (Matsuyama, Japan) and Mohammed YOUSFI, C.N.R.S Professorship (LAPLACE, Toulouse, France). Moreover it was achieved within the collaboration with Institut des Matériaux de Nantes Jean Rouxel (IMN), Université de Nantes (Nantes, France).

Foremost, I would like to express my sincere gratitude to my advisor Prof. Masafumi JINNO for his continuous guidance and critical supervision throughout this work. More specially, my deepest thanks go to my advisor Prof. Mohammed YOUSFI for his patience, motivation, enthusiasm, and immense knowledge. His guidance helped me in all the time of research and writing of this thesis. I could not have imagined having a better advisor and mentor for my Ph. D study.

My sincere thanks also go to Dr. Hideki MOTOMURA, Associate Professor, who gives me access to the laboratory and research facilities and for the conduction and co-operation in experiments. Without their precious support it would not be possible to conduct this research.

I also would like to express my sincere gratitude to Ahmed RHALLABI, Professor at Université de Nantes France, for his active implication in simulation part of this thesis, and without which, this work would not present the numerical simulation aspects that it contains. I would like to express my deep gratitude for all that he taught me and I enormously thank him for time that he invested, for his great patience and to make himself available for my defense. A warm thank to the members of Institut des Matériaux de Nantes Jean Rouxel IMN for their collaboration and cordial reception during my two stays. These stays were essential for the elaboration of the Monte Carlo Poration Model.

In addition, a thank you to Dr. Spiros KITSINELIS, to introduce me to Optical Emission Spectroscopy (OES). His assistance during my first experiments on OES measurements was invaluable. I also appreciate the help and assistance of Dr. Yoshihisa IKEDA, Assistant professor at Ehime University.

I am very grateful to Patricia BERTONCINI, lecturer at Université de Nantes (Nantes, France) and Anne TALNEAU, Research Director at C.N.R.S (Marcoussis, France), to have agreed to be reviewers of my thesis and for their critical reading of the manuscript and valuable comments.

I should like to express my thanks to Kazunori KADOWAKI and Satoshi SHIMOMURA, Professors at Ehime University and Georges ZISSIS, Professor at Université Paul Sabatier, for the honor that they made me while agree to examine this work and to make itself available for my defense.

I thank my fellow labmates : Melissa MAULOIS, Joseph-Marie PLEWA, Florian JUDÉE, Jérémy-Marie PLEWA, Julie CHAUVIN, Maeva COURREGÉ, Zoe LAFOREST, in LAPLACE laboratory and Yasuhito SONE, Hidetoshi MURAKAMI, Youhei IKEDA, in EECL laboratories, for the stimulating discussions and for all the fun we have had during my thesis preparation. Special thanks to all my friends from all over the world: Hanan ALAWADHI, Fred NELSON, Yousif ELSAMANI, Bernard KANO, Cindy KARINA, Alina BISTA, Lydie LAREXSISTE, Ikbal MARGHAD, for all the good moments spent together. In particular, I am grateful to Yuko MATSUSHITA of General Affairs Section Faculty of Engineering at Ehime University for her assistance, her support and her good mood throughout my stays in Japan.

Last but not least, I would like to thank my family: my husband, my sweetheart son Abdel-Karim (Bébé thèse), my parents and my sister, for their strong supports and the enormous motivation that they brought to me throughout these three years of thesis in order to undertake as well as possible this Ph. D thesis.

TABLE OF CONTENTS

GENERAL INTRODUCTION	1
CHAPTER 1: BIBLIOGRAPHIC OVERVIEW ON GENE TRANSFECTION AND CONTEXT	
1.1 Introduction.....	9
1.2 Overview on gene transfection	11
1.2.1 Applied fields of gene transfection.....	12
1.2.2 Description of different methods of gene transfection	14
1.2.2.1 Viral method.....	14
1.2.2.2 Chemical method.....	15
1.2.2.3 Physical method.....	18
1.2.2.4 Non-equilibrium cold atmospheric plasma discharge	21
1.3 Non-thermal plasmas at atmospheric pressure for gene transfection	21
1.3.1 Mechanisms of plasma gene transfection.....	22
1.3.1.1 Cell charging (plasma direct effect)	22
1.3.1.2 Chemical lipid peroxidation (indirect plasma effect).....	23
1.3.2 Overview on plasma setups used for gene transfection in literature	23
1.3.3 Overview on the different experimental setups tested at Ehime University for gene transfection	30
1.3.4 Comparative study on the different experimental setups tested at Ehime University for gene transfection: Transfection efficiency and cells viability.....	34
1.4 Parametric investigation on gene transfection efficiency using air microplasma for different protocols.....	38
1.4.1 Plasma treatment protocols.....	39
1.4.2 Discussion on plasma transfection protocols and effects	41
1.5 Conclusion	43
1.6 References.....	46

CHAPTER 2: EXPERIMENTAL CHARACTERIZATIONS BY OPTICAL EMISSION SPECTROSCOPY OF AIR MICROPLASMA USED FOR GENE TRANSFECTION

2.1	Introduction.....	53
2.2	Experimental setup used for plasma spectroscopy measurements	55
2.3	Results and discussion	57
2.3.1	Determination of rotational temperature T_{rot}	57
2.3.2	Estimation of T_{rot} from N_2 (SPS) and N_2^+ (FNS) emission spectra	58
2.3.2.1	Estimation of T_{rot} from OH ultraviolet band system	62
2.3.3	Determination of vibration temperature from N_2^+ (FNS) spectra at 388.4 and 391.4 nm.....	64
2.3.4	Determination of electron temperature T_e from N_2 (SPS) and N_2^+ (FNS) emissions	66
2.3.4.1	Reactions involved in creations and losses of upper levels of N_2 (SPS) and N_2^+ (FNS) emissions	68
A.	Electron impacts	69
B.	Radiative decays	70
C.	Quenching.....	70
2.3.4.2	Relations between N_2 (C) and N_2^+ (B) densities and rates of creations and losses.....	70
2.3.4.3	Relations between N_2 (C) and N_2^+ (B) densities and spectra intensities	71
2.3.5	Determination of densities of plasma charged particles.....	76
2.3.5.1	Electron density η_e from H_α line.....	76
A.	Instrumental broadening.....	79
B.	Doppler broadening	80
C.	Collisional broadening.....	82
D.	Stark broadening.....	83
2.3.5.2	Estimation of Nitrogen ion density from N_2 (SPS) and N_2^+ (FNS) spectra	85
2.4	Conclusion	89

2.5	References.....	92
-----	-----------------	----

CHAPTER 3: DESCRIPTION OF MONTE CARLO MODEL OF MEMBRANES PORATION BY PLASMA SPECIES FLUXES

3.1	Introduction.....	97
3.2	Overview on the numerical modeling of cold plasma interaction with cells membrane and tissues	99
3.2.1	MD works on electroporation of cell membranes for gene transfection	99
3.2.2	Reactive MD simulations of the interactions between plasma species and biomolecules	105
3.2.2.1	Reactive MD simulations for reactive species interacting with lipids	105
3.2.2.2	Reactive MD simulations for reactive species interacting with peptidoglycan.....	107
3.2.2.3	Reactive MD simulations for interaction of reactive species with DNA	109
3.2.2.4	Reactive MD simulations for interaction of reactive species with liquids	109
3.3	Monte Carlo poration model of cell membranes for application to plasma gene transfection	111
3.3.1	Descriptions of input data and Monte Carlo model.....	111
3.3.1.1	Estimation of fluxes of plasma species impacting the cell membrane	111
3.3.1.2	Reaction processes with cell membrane.....	115
3.3.1.3	Membrane structure and discretization domain	118
3.3.2	Description of Monte Carlo poration model.....	119
3.3.2.1	Flowchart of the Monte Carlo poration model	119
3.3.2.2	Identification of the targeted super-particle neighbours.....	121
3.4	Conclusion	123
3.5	References.....	124

CHAPTER 4: RESULTS AND DISCUSSION ON MONTE CARLO SIMULATIONS OF MEMBRANES PORATION BY GASEOUS PLASMA SPECIES

4.1	Introduction.....	129
4.2	Computational simulation conditions	130
4.3	Reaction probabilities in the case of each super-particle.....	132
4.4	Results and discussion	135
4.4.1	Effect of the initial incidence angle of ions, and radicals	136

4.4.2	Effect of electron energy distribution.....	137
4.4.3	Effect of the reflection processes in the case of ions, and radicals	141
4.4.4	Role of the processes of electron opening of an activated site.....	143
4.4.5	Effect of the initial particle number N_p	144
4.5	Experimental validation of the Monte Carlo stochastic simulations of the membrane poration	145
4.5.1	Simulation and experimental conditions	145
4.5.2	Correlation between particle number and plasma irradiation exposure time	146
4.6	Conclusion	149
4.7	References.....	150
	GENERAL CONCLUSION.....	151

GENERAL INTRODUCTION

The transfection of nucleic acids into cells through their membranes is one of the most valuable and frequently used tools of biological science. Transfection methods are used for a range of applications, including gene function studies, modulation of gene expression, and production of recombinant proteins. The transfection techniques which are commonly used to introduce a foreign gene into host cells can be classified into three groups. In the first group, methods that make use of genetically engineered viruses, particular viruses have been selected as gene delivery vehicles because of their capacities to carry foreign genes and their ability to efficiently deliver these genes associated with efficient gene expression. In general, the achieved transfection efficiencies in primary cells and cell lines are high. However, only cell types carrying a viral specific receptor can be transferred. The first step in the infection cycle of a virus is the interaction between the virus and a cellular receptor on the surface of a target cell, resulting in the fusion of the viral and the cellular membrane. Cells which are not carrying such a receptor cannot be infected by the virus. Other limitations of viral gene transfer are the time consuming and laborious production of vectors, elevated laboratory costs due to higher biosafety level requirements, limitation of insert size, variability in infection potencies of the generated virus particle preparations and possible immunogenic reaction. For the second group, there are chemical methods or methods that rely on carrier molecules to overcome the cell membrane barrier. In fact, there are no chemical reactions taking place between the carrier molecule and the nucleic acid or any cellular component. The principle consists of the interaction of negatively charged nucleic

acids with positively charged carrier molecules, like polymers or lipids, enabling the nucleic acid to come into contact with the negatively charged membrane components and incorporating the gene into the cell by endocytosis and later releasing it into the cytoplasm. This transfection technique is able to transfect a wide range of cell types (mainly adherent cell lines) with high efficiency, and relatively low costs. Additionally, it offers advantages like the successful delivery of DNA of all sizes, delivery of RNA and protein, as well as the applicability to use this technique for both transient and stable protein production. Despite these advantages, there are several drawbacks, including low efficiencies in most primary cells, as well as its cytotoxicity and its dependence on cell division. In the case of the third group, physical methods or methods that deliver nucleic acids directly to the cytoplasm or nucleus by physical or mechanical means and without the usage of foreign substances like lipids. Generally, it is based on the application of an electric field (electroporation) or acoustic field (sonoporation) or magnetic field (magnetoporation) or even photon (laser) to destabilize the membrane. The electroporation is a frequently used physical gene transfer method. The high voltage pulses of electricity applied to the cells create a potential difference across the membrane, as well as charged membrane components, and induces temporary pores in the cell membrane for DNA entry. With this physical method, it is possible to transfect large DNA fragments and the efficiencies achieved in cell lines are good. Unlike the chemical reagents, there is no reagent-induced cytotoxicity towards the cells. However, the drawbacks are low efficiency in primary cells and high mortality rates caused by the high voltage pulses or by only partially successful membrane repair. The technique requires fine tuning and optimization for duration and strength of the pulse for each type of cell used. As a consequence of the compromise between efficiency and mortality, usually 50% of the cells are lost. Thus, not all transfection methods can be applied to all types of cells or experiments, and there is wide variation

with respect to the achieved transfection efficiency, viability, level of gene expression etc. Thus the development of a new method for safe and high efficiency gene transfer is an important subject in medical and biological fields. The reader interested by more details on these different methods used for gene transfection can consult the references given in chapter 1.

The cold atmospheric plasma irradiation is potentially a new safe and damage-free gene transfection method. It can lead to a transient permeabilization of the cell membrane allowing processes of gene transfection in which DNA and cells are both exposed to fluxes of active plasma species (electrons, ions and neutral radicals) and also to the plasma-induced electric field. The mechanisms leading to membrane permeabilization during plasma species/cell interactions are cell charging, lipid peroxidation and the well-known membrane electroporation provided a high enough plasma-induced electric field. However, the mechanisms of more particularly membrane poration are far to be clear and controlled. Therefore, the aim of this thesis is to study the mechanisms of plasma-induced membrane permeabilization using a specific air microplasma that is also characterized in the framework of this thesis. This aim is achieved by numerically simulate the membrane permeabilization and pore formation when the cells are impacted by the active species of the micro air plasma.

The thesis is divided into four chapters that follow this general introduction.

The first chapter is devoted to a bibliographical synthesis including the various existing or potential applications of gene transfection in the biomedical domain. Thereafter, the different common main transfection methods, as well as the new ones based on atmospheric plasma irradiation are described. In the second part of the first chapter, I begin by a bibliographic overview on the different developed and used plasma setups for gene transfection. This is aimed to underline that the cold plasma irradiation is an effective tool for gene transfection. However, one of the most

serious problems of the plasma transfection method is a difficulty in keeping simultaneously both high transfection efficiency and low cell damage. Another serious problem is the reproducibility: even if the plasma generation conditions such as applied voltage, waveform, frequency, etc. are identical, the transfection efficiency varies shot by shot. To solve this problem, the researchers of electrical engineering department of Ehime University have evaluated four different plasma configurations: arc plasma discharge, an atmospheric pressure plasma jet (APJ) using helium carrier gas and equipped with 4 jets, a dielectric barrier discharge (DBD) plasma using also helium flow, and last an air microplasma discharge. Thus in the continuation of this first chapter, I describe the different experimental setups used for each plasma source. This is followed by some important results coming from a comparative study between rates of plasmid transfection and cell viability obtained in the case of each plasma setup. Finally, the most promising, safe and high efficiency plasma configuration, which is the micro air plasma discharge, will be focused on. For this purpose, an experimental parametric investigation on the involved process and gene transfection mechanism by using this reliable air microplasma discharge as well as the most important obtained results will be discussed. Through all of that, I will discuss the state of the knowledge of the various mechanisms involved in the plasma gene transfection. This thus allows the reader to a better understand the motivations of the present research work which are aimed to more precisely develop and exploit a specific Monte Carlo poration model. This model is aimed to simulate the pore formation of few nanometre of width through cell multilayer membranes when irradiated by the air microplasma discharge generated in ambient air.

The second chapter is devoted to the spectroscopic characterizations of the air microplasma. Such plasma characteristics are needed as input data for the developed Monte Carlo poration model that requires the *a priori* knowledge of more particularly the fluxes and the energy of the main

plasma species arriving to the cell membrane. This concerns more particularly the knowledge of the density of charged particles (electrons and N_2^+ ion), and the temperatures of gas T_g and electrons T_e . In fact, the micro air plasma used for gene transfection is a corona discharge generated in ambient air from the tip of a pulsed high voltage microtube placed 2 mm in front of a petri dish containing deionized water and set over a grounded copper plate. The rotational temperature T_{rot} is estimated from comparison of synthetic and experimental spectra of OH(A-X), N_2^+ (FNS: 0, 0) at 391.4 nm, and N_2 (SPS: 0, 0) at 337nm. Based on N_2^+ (FNS: 0, 0) and N_2^+ (FNS: 1, 1) head bands spectra at 391.4 nm and 388.4 nm. The vibrational temperature T_{vib} is estimated along the plasma axis between the tip electrode up to the grounded plate. Moreover, the electron temperature T_e is estimated from an interesting approach based on the experimental ratio of the closest nitrogen emission spectra of N_2^+ (FNS: 0, 0) at 391.4nm and N_2 (SPS: 2, 5) at 394.3 nm. This is based on one hand a balance equation between creations and losses of excited upper levels of these two UV spectra and on the other hand on the electron impact rates of the creation of these upper levels calculated from a solution of multi-term Boltzmann equation. Then using the measured $H\alpha$ spectra, electron density n_e has been estimated from Stark broadening versus the inter-electrode position. Last, the spatial variation along z axis of the nitrogen ion density has been determined from the relative intensities of the same close wavelength spectra (N_2 (SPS: 2, 5) at 394.3 nm and N_2^+ (FNS: 0, 0) at 391.4 nm). The present experimental plasma characteristics are used to better understand the mechanisms and the processes involved during plasma gene transfections when using the Monte Carlo poration model developed in the present work.

The third chapter begins with a review on the progress made so far on the numerical modeling of cold plasma interactions with cells and tissues. I underlined that there are no literature simulations devoted to membrane permeabilization and pore formation when impacted by plasma

actives species. This is why I developed for the first time in literature a specific Monte Carlo poration model based on the concepts of super-particles interacting with super-sites of the membrane following super-reaction processes. The present Monte Carlo poration model is aimed to statistically simulate, at a global (or macro) scale, the pore formation during atmospheric pressure plasma interactions with cell membranes. In the framework of this simulation model, each plasma species was assumed as a super-particle grouping a large number of particles. Three kinds of plasma active species are considered: electrons, ions and neutral radicals, with fluxes estimated from a plasma reaction kinetic model and the OES study conducted in chapter 2. The membrane layers were assumed as a simple membrane model superposing four layers of phospholipids and proteins. Moreover, each layer was constituted by a succession of super-sites subjected to specific super-processes (recombination, reflection, activation of a site, opening) during the membrane impacts by the plasma super-particles.

The last chapter (chapter 4) is first devoted to a description of the computational simulation conditions as for instance the initial particle number, the simulation domain geometry and the fraction of the initially activated super-sites. The different occurrence probabilities of each super-process between a given plasma super-particle and a membrane super-site that are considered in the Monte Carlo model are also defined and described. These reaction probabilities are selected in a suitable way based on some biophysical considerations; as for example the magnitude of the layer density (either protein or lipid layer), the plasma super-particle type and the energy magnitude of the electrons. In addition, the super-site state is also considered as a factor determining the choice of reaction probabilities. Furthermore, for an accurate exploitation of our Monte Carlo poration model, the good estimations of the different probabilities of occurrence of the whole considered super-processes are absolutely necessary. This is why a large parametric

study is conducted in the second part of chapter 4. This is aimed to evaluate the effects of the initial simulation parameters as well as the magnitude of the occurrence probabilities of each reaction super-process on the cell membrane permeabilization and pore formation. More precisely, I discuss the effects of the initial incidence angle of ions, and radicals, the effect the energy distribution of the electrons, as well as the effects of reaction as for instance the role of the reflection process in the case of ions, and radicals, and the importance of the electron energy and processes in the super-site opening process. This parametric study enabled to underline several important and original results. Moreover, a comparison with the measured transfected efficiency of DNA plasmid and the surviving cell rate in the case of mouse fibroblast cells are used to discuss the validation of the present Monte Carlo poration model.

Last, these discussions and analyses of Monte Carlo simulations of membrane poration using air microplasma generated at atmospheric pressure are followed by a general conclusion summarizing the main results obtained in the framework of this thesis and giving some future orientations to the present research thesis.

CHAPTER 1

BIBLIOGRAPHIC OVERVIEW ON GENE TRANSFECTION AND CONTEXT

1.1 Introduction

As underlined in the general introduction, Gene transfection, the process of inserting using a vector a foreign genetic material, such as DNAs and RNAs, into cells, has origins as far back as the 1950s [1]. Transfection is one of the most valuable and frequently used tools of biological science. It is an important tool used in studies investigating gene function and the modulation of gene expression, thus contributing to the advancement of basic cellular research and drug discovery. The insertion of DNA into a cell enables the expression of proteins using the cells own machinery [2] in the aim to correct a cellular dysfunction, to modify genetic inheritance in order to treat pathology, to provide a new cellular function or to manufacture programmed cells able to grow and to become designed organs [3] (cf. Figure 1-1). Various approaches, such as viral, chemical and physical methods with non-viral vectors, have been developed to make gene delivery safer and more efficient [4]. However all these reliable methods are limited to a few experimental systems and can have known drawbacks. Therefore, the development of a new safe and damage-free technique of gene transfection is an interesting complementary technique to the existing ones. To this purpose, gene transfection based on low-temperature atmospheric pressure plasmas can lead to a transient permeabilization of the cell membrane allowing processes of gene transfection.

Nevertheless, one of the most important issues for the plasma irradiation technique when used for gene transfection is to find an optimal relationship between transfection efficacy and cell damages. In fact, under the condition of high transfection rates, the cells can also be damaged. Thus in the aim to optimize this trade-off relationship, several types plasma sources with different designs and configurations as well as gene transfection protocols were developed. Moreover, the mechanisms and the processes of plasma gene transfection, more precisely membrane poration are far to be clear and controlled. Therefore fundamental understanding on plasma-induced membrane permeabilization is required for further progress in the field of plasma gene transfection.

The aim if this first chapter will be, in first part, to make a short bibliographical synthesis including the various applied and potentially applied fields of gene transfection in the biomedical domain. Thereafter, the different common main transfection methods as well as the new ones based on atmospheric plasma irradiation will be reviewed, while detailing the main advantages and the drawbacks of each method.

In the second part of the chapter, on the one hand, a bibliographic overview on the various developed and used plasma setups for gene transfection in literature will be reviewed. On the other hand a detailed overview on the plasma setups developed in Ehime University (arc plasma discharge, an atmospheric pressure plasma jet (APJ) using helium carrier gas and equipped with 4 jets, a dielectric barrier discharge (DBD) plasma using also helium flow, and last an air microplasma), will be described, followed-up by some important results derived from a comparative study based on transfection and cells viability rates obtained in the case of each plasma setup. Finally, the most promising, safe and high efficiency plasma configuration, which is the air microplasma discharge, will be focused on. To this aim, an experimental parametric investigation on the involved process and gene transfection mechanism by using this reliable

microplasma discharge as well as the most important obtained results will be discussed based on different gene transfection protocols. Through all of that, it is discussed the state of knowledge of the various mechanisms imply in the plasma gene transfection, and the importance of their better understanding to make further improvements and progresses in gene transfection technique.

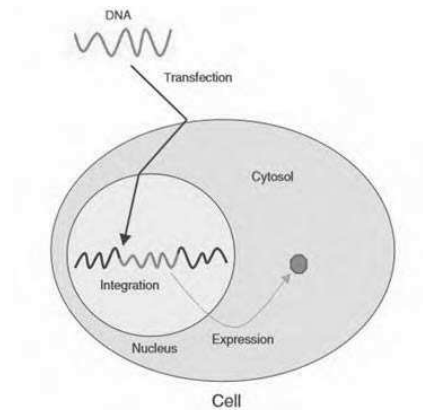


Figure 1-1 Schematic diagrams of gene transfections principle by using virus vector. Foreign DNA (red-wave) is delivered to nucleus by passage through the cell and nuclear membranes. Foreign DNA is integrated into the host genome (black-wave) and expressed sustainably [5].

1.2 Overview on gene transfection

Genes have long been considered as medicines [6]. During the past decade, the field of gene therapy has grown into a dynamic and exciting interdisciplinary research that not only impacts on the development of innovative cures but also provides significant added value by applying gene transfection tools to study and manipulate biological systems. It is widely anticipated that improved gene transfection approaches will yield new treatments and cures of a wide range of human diseases [7]. There are some of the most urgent unmet medical needs, such as hereditary immune deficiencies, neurodegenerative and neuromuscular disorders, hemophilia, cardiovascular disease, congenital blindness, infectious diseases and cancer [4]. In the absence of effective drugs or alternative therapies, the advances in gene therapy technology represent the best hope for the many patients and families that are blighted by these various diseases.

1.2.1 Applied fields of gene transfection

The diverse applications of gene transfection are categorized under four strategies:

The gene replacement therapy for monogenic diseases: Many human genetic diseases are clearly defined by a single gene defect, and gene replacement is a straightforward approach to treating these diseases. Not surprisingly, the majority of the most advanced clinical gene therapy development falls into the category of gene replacement, because the conceptually simple design leads to extensive investigation. Gene replacement can take place either directly *in vivo* or through *ex vivo* cell therapy [8]. The promising gene replacement clinical trials involve treating of respiratory diseases [9][10], leukodystrophies (degeneration of the white matter in the brain)[11], life threatening inflammation in pancreas [12] and blood disorders. Taken together, these human gene replacement applications have pioneered the gene therapy field.

Gene addition for complex disorders and infectious diseases: In contrast to a single gene defect underlying monogenic diseases, the combination effects of multiple genes and environmental factors cause complex disorders such as cancer and heart diseases rendering gene replacement not feasible for these disorders. Complex disorders are often common, and represent the most urgent unmet medical needs. In addition to genetic disorders, infectious diseases also debilitate or kill a large population worldwide. Therefore, significant efforts of gene therapy development have been devoted to these diseases [8]. Including heart disease [13], cancer [14], cardiovascular diseases [15] and neurodegenerative diseases [16], as well as infectious diseases. Indeed gene therapy vaccines are being developed and trialed for tackling infectious diseases, including tuberculosis [17], malaria[18], HIV [19] and influenza [20].

Gene expression alteration targeting RNA: RNA can be an intermediate (e.g. messenger RNA) or final (e.g. microRNA) gene product, with diverse functions in biology and disease. Due to the

versatile roles of RNA molecules in controlling gene expression, gene therapy strategies specifically designed to target RNA or to produce effector RNA molecules deserve close attention [8]. Here, two commonly utilized gene therapy strategies based on RNA biology; Gene knockdown by RNA interference (RNAi)[10][21][22] and Reprogramming messenger RNA (mRNA) [23].

Gene editing to introduce targeted changes in host genome: The potential of genome editing in human gene therapy applications is evident, as a number of successful studies in human cells and model organisms have been reported [24][25]. However, the specificity of editing needs to be rigorously tested to address possible off-target effects before widespread clinical use [26]. In addition, editing efficiency needs to be further improved to meet therapeutic needs, particularly in *in vivo* gene therapy settings that require gene editing in an enormous number of cells throughout an organ or the whole body.

Furthermore, the manipulation of gene expression is a core technique in more research areas such as drug development and tissue engineering [27][28]. However, although the gene transfer field is rapidly progressing, is still far from providing enough tools for the treatment of the previously mentioned diseases. Moreover, many gene transfer technologies still remain highly unexplored both experimentally and theoretically [29]. The most pressing issue that the field of gene therapy has to address is the development of efficient and safe gene delivery methods. Indeed, one of the main difficulties with gene transfection is how to effectively and safely deliver the genetic material to different cells, organs and tissues. For instance, this is achieved by using gene delivery vehicles, namely vectors which carry the material into the cell, and it can be categorized into two classes: DNA (non-viral) vectors and viral vectors [7][30]. However side effects such as the carcinogenesis and leukemia occurred by the gene therapy using the virus vector, it is not in practical use. And, in the gene therapy using the DNA vector, it is also not in use as a gene therapy because demerits such

as cytotoxicity, low gene transfection and integration efficiency are exist. To be in practical use of gene therapy, it is necessary to develop the safe and high efficiency gene transfection method in substitution for viral vector method.

1.2.2 Description of different methods of gene transfection

Transfection can be accomplished using many developed methods, for instance, biological methods based on the virus as delivery vector of the nucleic acid. As well as , the common main methods for non-viral delivery, which are broadly classified into chemical and physical methods [5]. Many types of genetic material, including plasmid DNA, siRNA, proteins, dyes, and antibodies, may be transfected using any of these methods. However, a single method cannot be applied to all types of cells; transfection efficiencies and cytotoxicity may vary dramatically and depend on the method, cell type being utilized, and types of experiments being performed [5]. Therefore, to obtain high transfection efficiencies, low cell toxicity, minimal effects on normal physiology, and be easy to use and reproducible, all relevant factors should be considered for planning and selecting the appropriate transfection method.

1.2.2.1 Viral method

The most commonly used method in clinical research is virus-mediated transfection. This process named transduction can be applied to several biological models and represents the most efficient approach to achieve good gene expression levels in many cells [31]. The use of viral vectors was employed as early as the late 1970's to express functional mRNA and protein [32]. Many mammalian viruses have been explored as gene delivery vectors [33][34] [35]. Thus, virus-mediated transfection is highly efficient and it is easy to achieve sustainable transgene expression *in vivo* owing to the viral nature of integration into the host genome for example, retrovirus murine leukemia virus (MLV) has been used as a viral vector to establish sustainable transgene expression

in humans [36]. MLV integrates its DNA into the host genome and the integrated DNA is expressed in the host. The integrated MLV DNA replicates as the host genome does. Consequently it segregates into daughter cells, which enables sustainable transgene expression. The major drawbacks of virus-mediated transfection are immunogenicity and cytotoxicity. Introduction of a viral vector may cause an inflammatory reaction and an insertional mutation, because viral vectors integrate into the host genome randomly, which may disrupt tumor suppressor genes, activate oncogenes, or interrupt essential genes [9]. Another disadvantage of this method is that a virus package has limited space for a foreign gene to keep infectivity as well as the high costs due to biosafety requirements[5][37]. For these reasons, much effort has been made to develop non-viral transfection methods even though virus-mediated transfection is highly effective and easy to use [5].

1.2.2.2 Chemical method

Chemical transfection methods are the most widely used methods in contemporary research and were the first to be used to introduce foreign genes into mammalian cells [38]. These methods commonly use compounds such as cationic polymer (one of the oldest chemicals used), calcium phosphate and cationic lipid (the most popular method), to name a few [38][39]. The elementary principle of chemical methods is similar. Positively charged chemicals make nucleic acid/chemical complexes with negatively charged nucleic acids. These positively charged nucleic acid/chemical complexes are attracted to the negatively charged cell membrane. The exact mechanism of how nucleic acid/chemical complexes pass through the cell membrane is unknown but it is believed that endocytosis and phagocytosis are involved in the process [5]. Transfected DNA must be delivered to the nucleus to be expressed and again the translocation mechanism to the nucleus is not yet known[5].

Calcium phosphate represents the oldest and most inexpensive chemical method for transfecting nucleic acids. It has been a popular transfection method since its introduction in the early 1970s by Graham and van der Eb [40]. Furthermore, the technique is easy to master, it is effective with many types of cultured cells, and it can be used for both transient and stable transfection of a variety of cultured cell types. However, calcium phosphate co-precipitation is prone to variability due to its sensitivity to slight changes in pH, temperature, and buffer salt concentrations, and can be cytotoxic to many types of cell cultures, especially of primary cells. In addition, it is unsuitable for *in vivo* transfer of nucleic acids to whole animals, and it shows relatively poor transfection efficiency compared to other chemical transfection methods such as lipid-mediated transfection [41].

Cationic lipid-mediated transfection is one of the most popular methods for introducing foreign genetic material into cells. Although first generation of lipid-based transfection reagents relied on artificial liposomes that could envelop nucleic acids and then fuse with the cell membrane to deposit their cargo inside [42], newer cationic lipid-based reagents spontaneously form condensed nucleic acid-cationic lipid reagent complexes via electrostatic interactions between the negatively charged nucleic acid and the positively charged head group of the synthetic lipid reagent. These complexes are believed to be taken up by the cell through endocytosis and then released in the cytoplasm. Once in the cell, transfected DNA is translocated to the nucleus to be expressed by a yet unknown mechanism [43][44]. The advantages of cationic lipid-mediated transfection are the ability to transfect a broad range of cell lines with high efficiency, and its ability to deliver DNA of all sizes, as well as RNA and proteins. In addition, this method can be applied to both stable (Stable viral delivery systems that provide long-term, mid-level production of protein or gene expression) and transient expression (express the foreign gene without its integration into their

genome, for a finite period of time, usually several days, after which the foreign gene is lost through cell division or other factors). Moreover, unlike other chemical methods, it can be used for *in vivo* transfer of DNA and RNA to animals and humans[30]. The main drawback of cationic lipid-mediated transfection is the dependence of transfection efficiency on the cell type and culture conditions, requiring the optimization of transfection conditions for each cell type and transfection reagent [30].

Another chemical method based on cationic polymers, which differ from cationic lipids in that they do not contain a hydrophobic moiety and are completely soluble in water. Although they differ dramatically in their degree of transfection efficiency and cytotoxicity. Among the cationic polymers used for the transfection of cultured mammalian cells, DEAE-dextran was one of the first studied [30]. This reagent has been successfully used to deliver nucleic acids into cells for transient expression and short-term expression analyses but is not suitable for stable transfection studies [45]. The primary drawback of the DEAE- dextran system is the cytotoxicity. Therefore, the effects of concentration and exposure times need to be determined before transfection for individual cell lines. Other synthetic cationic polymers have been used to transfer DNA into mammalian cells. The polymers include protamine, intact and fractured polyamidoamine dendrimer [46][47][48], more recently, polyethylenimine (PEI) [49][50] which appears to be better than cationic liposomes at delivering DNA across the nuclear envelope [51][52].

Despite that these methods have merits of relatively low cytotoxicity, no mutagenesis, no extra-carrying DNA, and no size limitation on the packaged nucleic acid, the transfection efficiency of chemical methods is largely dependent on factors such as nucleic acid/chemical ratio, solution pH, and cell membrane conditions, so the process results in low transfection efficiency, especially *in vivo*, compared with virus-mediated methods [31].

1.2.2.3 Physical method

The physical transfection methods are the most recent methods. It uses diverse physical tools to deliver nucleic acids [5]. It depends neither on viral vehicles and their receptors nor on biochemical structures or features of target cell membranes required for uptake of a vehicle-DNA complex [30]. These methods directly deliver nucleic acids into the cytoplasm or the nucleus of the cell. I can cite for instance, direct micro injection, biolistic particle delivery, laser-based transfection, electroporation [53], sonoporation [54], and other methods using for instance magnetic field to destabilize the cell membrane. Finally, I can also cite, the novel transfection method using cold gas plasma [55] [56].

Briefly, the direct micro injection delivers nucleic acids into the cytoplasm or the nucleus [57], one cell at a time by means of a fine needle; therefore, this method is limited to *ex vivo* applications such as the transfer of genes into oocytes to engineer transgenic animals or the delivery of artificial chromosomes [57]. Although direct microinjection is nearly 100% efficient, it demands considerable technical skills, is extremely labor-intensive, and often causes cell death. Moreover, this method is not appropriate for studies requiring the transfection of large number of cells.

Moreover, the relatively new physical method of gene transfer is biolistic particle delivery, also known as particle bombardment technique [58]. It involves projecting of microscopic heavy-metal particles (often gold or tungsten) coated with nucleic acids into recipient cells at high velocity using a ballistic device (i.e., “gene gun”)[59][60]. Biolistic particle delivery can be used to transiently transfect dividing and non-dividing cells in culture as well as cells *in vivo*, and it is often used for genetic vaccination and agriculture applications [61]. While this technique is reliable and fast, it requires costly equipment, causes physical damage to the samples, and necessitates a large number of cells due to high mortality.

Furthermore, the laser-mediated transfection, also known as phototransfection, laserfection, or optoporation, uses a laser pulse to transiently permeabilize the cell membrane [62][63]. When the laser induces a pore in the membrane, the osmotic difference between the medium and the cytosol facilitates the entry of nucleic acids or other desired substances in the medium (ions, small molecules, proteins, semiconductor nanocrystals, etc.) into the cell. Advantages of laser-mediated transfection include high transfection efficiency and the ability to make pores at any location on the cell. However, the method requires an expensive laser-microscope system and the cells have to be attached to a substrate.

In addition to the methods mentioned above, electroporation is the most widely used physical delivery technology [30]. The exact mechanism is unknown, but it is supposed as shown in Figure 1-2 [64] that a short electrical pulses at an optimized voltage and lasting only a few microseconds to a millisecond generates an electrical field, which disturbs the cell membrane capacitance and creates transient membrane pores through which small particles can pass into cells (further details on the mechanisms of electroporation of cell membranes in chapter 3, sub-section 3.2.1. This technology was initially developed for *in vitro* DNA delivery but has expanded to include transfection of other nucleic acids (e.g., oligos, mRNA, siRNA, and miRNA), drug delivery, cell-cell fusion (i.e., electrofusion), and membrane protein insertion (i.e., electro-insertion)[5].

Indeed, electroporation can be an effective and efficient alternative to chemical transfection. Its main advantage consists on its applicability for transient and stable transfection of all cell types. In fact, it provides a robust and universal approach for transfecting various cell types including bacterial, mammalian, yeast, and plant cells, with any type of nucleic acid [5]. Furthermore, because electroporation is easy and rapid, it is able to transfect a large number of cells in a short

time once optimum electroporation conditions are determined [5]. However, the major drawback of electroporation is substantial cell death caused by high voltage pulses and only partially successful membrane repair, requiring the use of greater quantities of cells compared to chemical transfection methods [30]. The high cell mortality can be minimized through optimization of experimental conditions and may be counterbalanced by increased transfection efficiencies: Conditions similar to chemical transfection (e.g., nucleic acid amount and cell density) or parameters unique to electrical methods (e.g., voltage and pulse types).

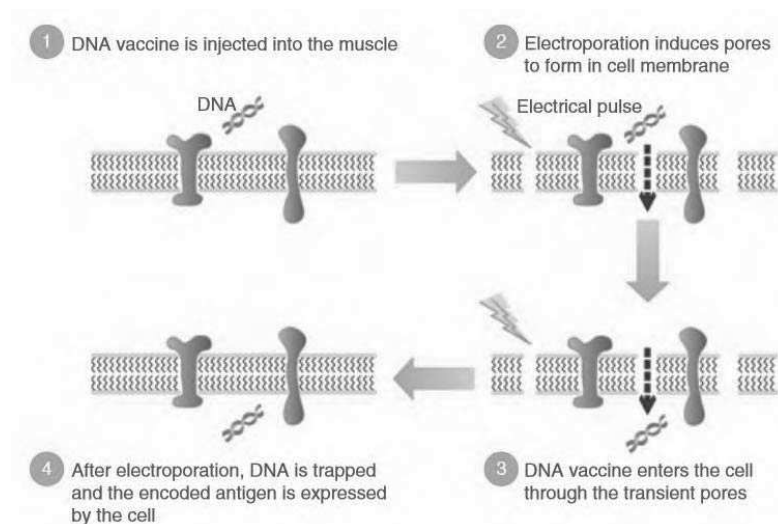


Figure 1-2 DNA vaccination and schematic representation of the effect of electroporation at the cell membrane level [64].

As already emphasis and with a burgeoning interest in transfection, particularly for therapeutic purposes, advances in the field of transfection are spurred by the need to increase efficiency, to broaden the range of transfectable target cell or tissue types, and to address specific workflow requirements. Therefore, the improvement of these current techniques of gene transfection or the development of new safe and damage-free techniques is in demand.

1.2.2.4 Non-equilibrium cold atmospheric plasma discharge

The emergence of plasma medicine field proves that the non-equilibrium plasmas are able to initiate, promote, control, and catalyze various complex behaviors and responses in biological systems. For instance apoptosis, cell detachment [65], and cell permeabilization [66]. More importantly, it showed that the non-thermal plasma effects can be tuned to achieve various desired medical purposes, especially in medical sterilization and treatment of different kind of skin diseases, such as wound healing, tissue regeneration and gene transfection [67][57]. Indeed, a method of interesting efficiently of transferring numerous selected molecules into various cells by using cold gas plasma was patented by Miyoshi *et al.* [68] in 2002 and was then reported by Ogawa *et al.*[55] . The plasma, which is generated by discharge contains a large number of charged and uncharged particles such as ions, electrons, and radicals and could easily provide an appropriate impact on the samples and mediate gene transfer as well as electroporation [57][67][69]. On the one hand, it was shown that the plasma can transfer the genes even into primary neuronal cells without a loss of function of the cells, into which electroporation cannot sufficiently do it [57]. On the other hand, since this technique is free from adverse effect associated with viruses, there is no risks compared to the others methods mentioned above [69].

1.3 Non-thermal plasmas at atmospheric pressure for gene transfection

As already highlighted, gene transfection induced by low-temperature plasmas can be an interesting alternative to the previous conventional methods. It was once shown in the literature that the plasma irradiation leads to a transient permeabilization of the cell membranes allowing gene transfection (ref Ogawa *et al.* [55], Sakai *et al.*[56] Leduc *et al.* [65][70], Nakajima *et al.*[66], Jinno *et al.* [67] [69] [71] [72] [73] and Sasaki *et al.* [74]) in which DNA and cells are

both exposed to fluxes of active plasma species (such as electrons, ions and neutral radicals) and also to plasma-induced electric field [66]. Thus, the non-thermal plasmas are already well-known for their gene transfer ability; however, the mechanisms of this gene transfection are under debate. Short and long-living active species and radicals produced by plasma, and bombardment by charged particles are all listed as potential candidates for cell membrane poration and permeabilization.

1.3.1 Mechanisms of plasma gene transfection

The mechanisms leading to membrane permeabilization during plasma species/cell interactions are partly evoked in the literature [70] as twofold mechanisms: cell charging (direct plasma effect) and lipid peroxidation (indirect plasma effect). Obviously, the well-known membrane electroporation could be the third mechanism provided high enough plasma-induced electric field is present.

1.3.1.1 Cell charging (plasma direct effect)

In fact, in physical cell charging, the electrons accumulated on the cell membrane can generate Coulomb forces at the membrane surface high enough to deform the cell from its ellipsoidal form to a spherical form. This deformation of the cells could create a shear stress high enough to partially disrupt the wall of the cell thus creating transient pores. Experiments on poration indicate that direct plasma exposure is effective for gene transfection [56]. It is also evoked the possibility of a significant role of electric charging in this poration phenomena. Anyway, the contribution of cell surface charging is not really quantified. This is why cell detachment and poration in interactions with active plasma species should be further investigated using numerical models of the plasma membrane poration.

1.3.1.2 Chemical lipid peroxidation (indirect plasma effect)

The active species of the plasma reaching the cell membrane can react with the lipid bilayer and ultimately enable creation of transient pores. The hydroxyl radical OH is the most probable active species to initiate lipid peroxidation. Indeed, OH is known to react rapidly with organic molecules which is the pathway leading to lipid peroxidation. The propagation of the lipid peroxidation leads to the cross-linking of the fatty acid side chain which can lead to formation of transient pores [65].

In the aim to investigate experimentally the potentiality to use of non-thermal plasmas generated at atmospheric pressure for the gene transfection applications, different plasma devices in terms of configuration, generation, and irradiation of plasma have been used for gene transfection. An overview of these different existing plasma setups in literature as well as those tested at Ehime University, with the corresponding obtained results is an essential step and it is presented in the following sub-section.

1.3.2 Overview on plasma setups used for gene transfection in literature

In 2005, Ogawa *et al.* [55] followed by Sakai *et al.* [56] presented a novel transfection method for eukaryotic cells using a type of atmospheric pressure discharge plasma jet. The plasma generation and irradiation was carried out as follows: a high air flow (around 90 slm) provided by an air pump, blown-off between electrodes powered by a pulsed high frequency (20 kHz) generating, on the downstream side, a U-shaped active gas plasma jet that impacts the sample mixtures of cells and plasmid placed under the electrodes (See Figure 1-3). The height (H) of the electrodes is adjusted to 22mm from the dish bottom so that the lower end of the flare can reach the target cells. The turntable under the electrodes was designed to rotate at 2 rounds per second

during electric discharges, and the distance between the two electrodes was adjusted to the half diameter of the 6 cm dish so that the whole cells on the sample dish could be homogeneously exposed to the gas plasma during transfection.

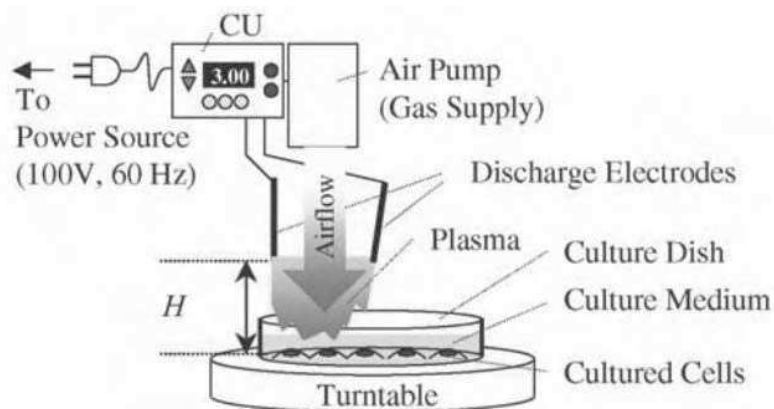


Figure 1-3 Schematic diagram of the plasma generation and the treatment of the cultured cells with the plasma generator [56].

The experimental conditions of the considered cells (HeLa-S3 and other cell lines), the transfected DNA (pEGFP-C1 plasmid at a concentration of $0.5\mu\text{g}/\mu\text{l}$), the solution used for cell and DNA immersion (phosphate buffered saline PBS), the method of cell evaluation (fluorescence microscopic observation and the flow cytometry analysis) are already described elsewhere [56]. The obtained results (cf. Figure 1-4) establish an optimum exposure time around (1–3s) of the treated cells to the plasma irradiation with a favorable transfection efficiencies (17.8-21.6%) and relatively low cell mortalities (0.65-2.86%). Indeed, the results of transfection clearly show that the cells became transiently permeable for plasmid DNA during the plasma exposure, suggesting that the plasma-mediated transfection may involve similar mechanisms that accounts for electroporation.

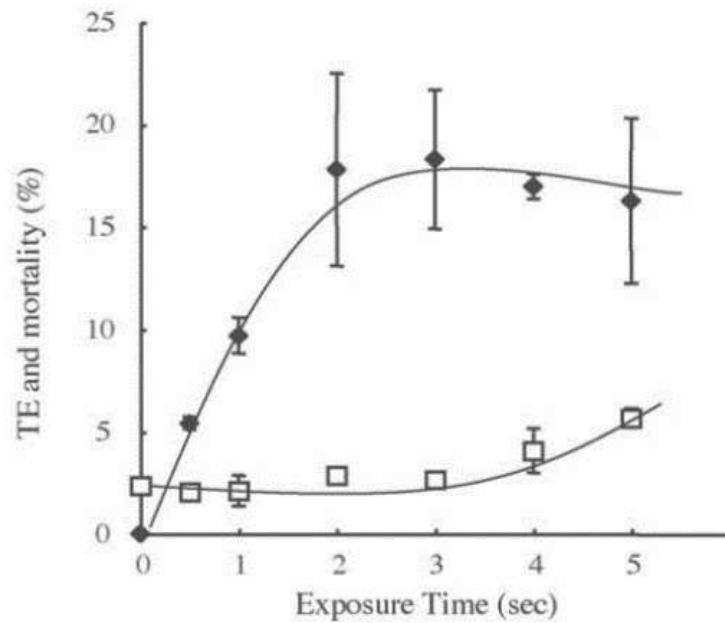


Figure 1-4 Transfection efficiencies with various lengths (0–5 s) of plasma exposures at the DNA concentration of $0.5\mu\text{g}/\mu\text{l}$. Filled diamonds, transfection efficiency; and open squares, mortality rate. TE, transfection efficiency [56].

Leduc *et al.*, in 2009 [70] used another plasma jet, referred to atmospheric pressure glow discharge torch (APGD-t). This last, is formed by the injection of a plasma-forming helium gas (at 0.5 slm) inside an annular space defined by a central capillary electrode (connected to RF power supply at 13.56 MHz) and a quartz confinement tube itself coated with a conductive paste (see Figure 1-5). The end of the nozzle is positioned 3mm away from the bottom of the Petri dish containing a mixture of cells (HeLa cells) and plasmid (hrGFP-II-1 at a concentration of $0.05\mu\text{g}/\mu\text{l}$). A motorized X–Y platform is used to move the sample and treat each plate in a selected pattern. The obtained results, show that the APGD-t is capable of including temporary cell permeabilization allowing a local transfection efficiencies as high as 35%. Moreover, the maximum radius of macromolecules able to enter into HeLa cells following a plasma treatment, was evaluated below 6.5 nm. On the other hand, it was show that no degradation occurs when the

plasmid DNA suspended in culture media is plasma-treated at the operating conditions leading to cell permeabilization [65].

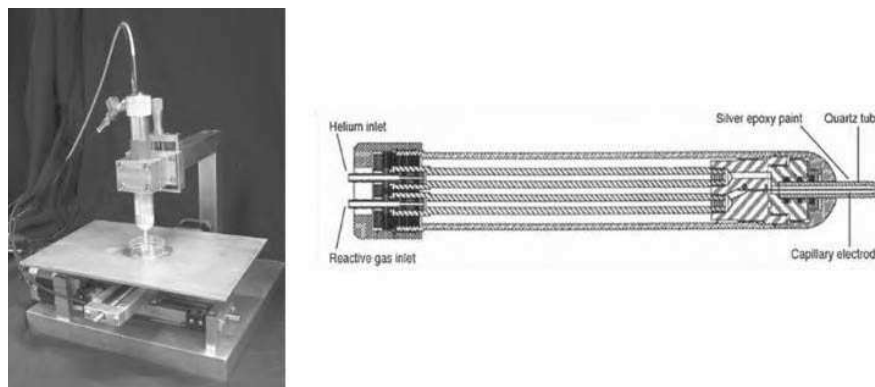


Figure 1-5 Picture of the APGD-t mounted over a Petri dish placed on the X–Y motorized platform and schematic drawing [70].

There is also low frequency (at 2.5kHz pulsed) plasma jet used by Nakajima *et al.*, in 2010 [66]. It's generated by argon gas (at 2 slm) in an outer glass tube with a stainless wire electrode covered with another glass tube and the outer glass tube is covered by a grounded mesh electrode. The gap between the tip of the generator and the surface of the agar medium or the water surface was 20 mm (Figure 1-6).

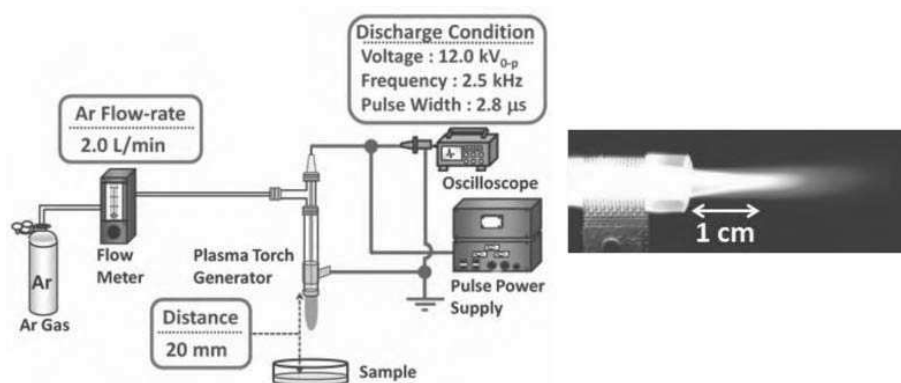


Figure 1-6 A schematic of the experimental setup for plasma exposure and Photograph of the generated plasma torch [66].

The plasma jet was exposed to the mixture of *E. coli* strain MV1184 cells and plasmid pUC19 DNA, and the transfection was clearly demonstrated [66].

Moreover, we can also refer to different types of dielectric barrier discharge DBD (ref Leduc *et al.*, in 2010 [65] and Sasaki *et al.*, 2014 [74]). Figure 1-7 shows both the photography and schematic drawing of the DBD plasma sources used by Leduc *et al.* [65]. It is based on a helium carrier gas flow (at 1 slm) passing through a mesh electrode and reaching to a glass plate placed over grounded electrode. The mesh electrode is powered by an AC high-voltage (10 kHz) (cf. Figure 1-7). On the other hand, it was found that based on the typical configuration of the used plasma sources, the plasma exposure to cells can be direct (DBD [65]) or indirect (APGD-t [70]). A comparison between both plasma sources was conducted in the aim to assess the possible negative effects of direct and indirect plasma treatment of mammalian cells (HeLa cells ATCC CCL-2) and naked DNA (hrGFP-II-1 at a concentration of 0.05 $\mu\text{g}/\mu\text{l}$) [65]. It was found that, the direct plasma treatment using DBD caused an oxidative stress to the cells, and both the direct and indirect plasma sources were able to fragment naked DNA. No lipid peroxidation was found in the treated samples [65]. From the obtained results we conclude that the plasmas may have unintended negative effects on cells which require a deep understanding of the mechanism of plasma-biological surface interactions.

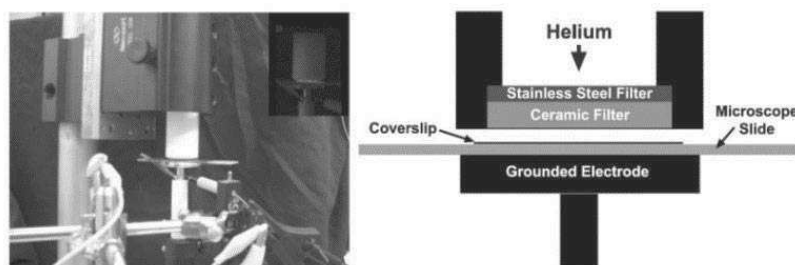


Figure 1-7 Picture of the DBD and schematic drawing [65].

In the aim to investigate the mechanism of gene transfer by plasma irradiation, Sasaki *et al.*, in 2014 [74] used another non-equilibrium atmospheric pressure plasma jet (APPJ). The last, is based on a helium carrier gas flow (at 3 slm) crossing a glass tube wrapped by two copper cylindrical electrodes that are powered by an AC high-voltage (10 kHz) (See Figure 1-8).

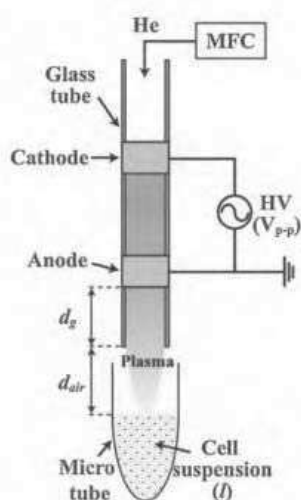


Figure 1-8 Schematic of the experimental setup [74].

The generated DBD plasma flows out from the nozzle quartz glass tube. The living cells in suspension consisting of genes (fluorescent dye YOYO-1) are irradiated with the plasma. The distance between the downstream electrode and the edge of the glass tube is defined as $d_g = 73\text{mm}$ and the distance between the edge of the glass tube and the surface of the cell suspension as $d_{air} = 5\text{mm}$. The cells after direct plasma irradiation under various conditions (suspension volume $l = 100$ or $150\mu\text{L}$ and plasma irradiation time $t_d = 0\text{--}60\text{s}$) are evaluated by simultaneous analysis of transfection efficiency and cell viability. As a result (see Figure 1-9), the efficiency has a maximal value at a short plasma irradiation time (3–5s) while maintaining a very high cell viability, and the volume of irradiated cell suspension changes the time dependence of the efficiency. Indeed, the non-monotonically increase of the efficiency predicted a mechanism of gene transfer based on a

competition between various factors such as reactive oxygen species ROS and electric field stimulation [74].

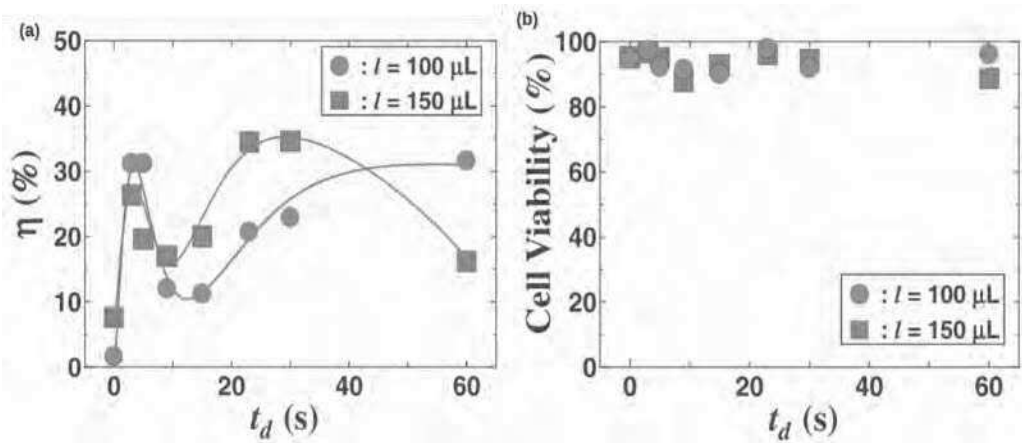


Figure 1-9 (a) Transfection efficiency η (%) of YOYO-1 and (b) cell viability (%) as a function of plasma irradiation time t_d (s) when the final volume of cell suspension l is 100 or 150 μL [74].

From this overview, one notes that one of the most important issues for the plasma irradiation technique when used for gene transfection is a trade-off relationship between transfection efficacy and cell damages. In fact, under the condition of high transfection rate, the cells can also be damaged [65]. Another most important issue is the transfection reproducibility [55][56]. For a given plasma source, even if the operating parameters of the power supply used to generate the plasma (e.g. applied voltage, waveform, frequency, etc.) are chosen identical, the transfection rates can vary significantly shot by shot [69][67]. Since the size and the spatial position of the plasma irradiations changes randomly in time, in some trials the genes and the cells are heavily damaged and reach necrosis or apoptosis by being exposed to the high density part of plasma, while in some other trials, the plasma irradiations do not reach the cells and transfection is not efficient. It was assumed that these important issues can be associated more particularly to the plasma instability [69]. In order to solve such instability, several types of plasma sources with

different designs and configurations were tested from 2002 until 2011 at Ehime University. An overview on these different tested plasma setups as well as the obtained results issue from a comparative study, are presented in the sub-section 1.3.3.

1.3.3 Overview on the different experimental setups tested at Ehime University for gene transfection

Four different types of plasma sources were developed and used at Ehime University: A an arc plasma discharge, an atmospheric pressure plasma jet (APJ) using helium carrier gas and equipped with 4 jets, a dielectric barrier discharge (DBD) plasma using also helium flow, and last an air microplasma discharge [69] [73].

The arc plasma configuration was identical to Ogawa *et al.*[55], which have a custom made HV power supply (Pearl Kogyo) for discharge initiation, (see Figure 1-10 (a)). The output voltage was pulse modulated sinusoidal waveform (20 kHz). The modulation frequency range was 10–200 Hz (typically 25 Hz) and its duty ratio range was 0–100%. The amplitude voltage could be set up to 15 kV. Argon or helium gas can be supplied to the discharge space with controlled flow rate using a MFC (mass flow controller, Advanced Energy, FC7710C). Two copper wire electrodes (diameter 1 mm) were attached in line on the bottom of a ceramic head (25 mm wide \times 22 mm deep \times 30 mm high). The head had a vertical hole (cross section of $4.3 \times 8.3 \text{ mm}^2$) for working gas supply. A 3.5 cm dish was on a rotation stage. The distance between the electrode and the sample solution in the dish was set at 12 mm. A flare-like plasma was initiated between the electrodes and the dish, as shown in the bottom of Figure 1-10 (a). The plasma irradiation area on the sample solution was about 30 mm in diameter, although it was perturbed because of waving of the flare.

In addition, a continuous working sinusoidal power supply (Rogie electronic, LHV-13AC) was used for plasma jet configuration (cf. Figure 1-10 (b)). The frequency was 14 kHz and the maximum amplitude of the output voltage was 10 kV. Four thin glass tubes (3 mm of external diameter and 1.25 mm of internal diameter) were used as nozzles. Copper tapes were attached on the outside surface of the nozzles as electrodes. The HV electrodes were placed near the tip of the nozzles, whereas the GND (ground) electrodes were placed towards 17 mm upstream from the HV electrodes. The four nozzles were placed in line as shown in Figure 1-10 (b), and the electrodes were connected in parallel (same voltage was applied to all nozzles). Helium working gas was distributed to each nozzle from one MFC. A plasma plume of up to 1 cm was constructed at the tip of each nozzle. The plasma irradiation area on the sample solution was line shape of about 15 mm long.

On the other hand, a positive polarity pulsed power supply (Suematsu electronic, MPC3010S-50SP) was used for dielectric barrier discharge DBD configuration (cf. Figure 1-10 (c)). The frequency was 100 Hz, pulse width was 100 ns and the maximum amplitude of the output voltage was 30 kV. An acrylic tube (20 mm of external diameter and 4 mm of internal diameter) was used as a gas nozzle. As HV and GND electrodes, two Teflon-covered copper wires were placed at the outlet of the nozzle. The gap length between the electrodes was set at 3 mm. The working gas was helium and its flow rate was controlled by the MFC. By applying the voltage and the working gas, a plasma plume was generated between the nozzle tip and the electrodes. In this configuration, the plasma did not propagate toward the downstream very much. Therefore, the electrodes were placed near the sample solution: the gap length between the electrodes and the solution was set at 0.1 mm. The plasma irradiation area on the sample solution was about 4 mm in diameter.

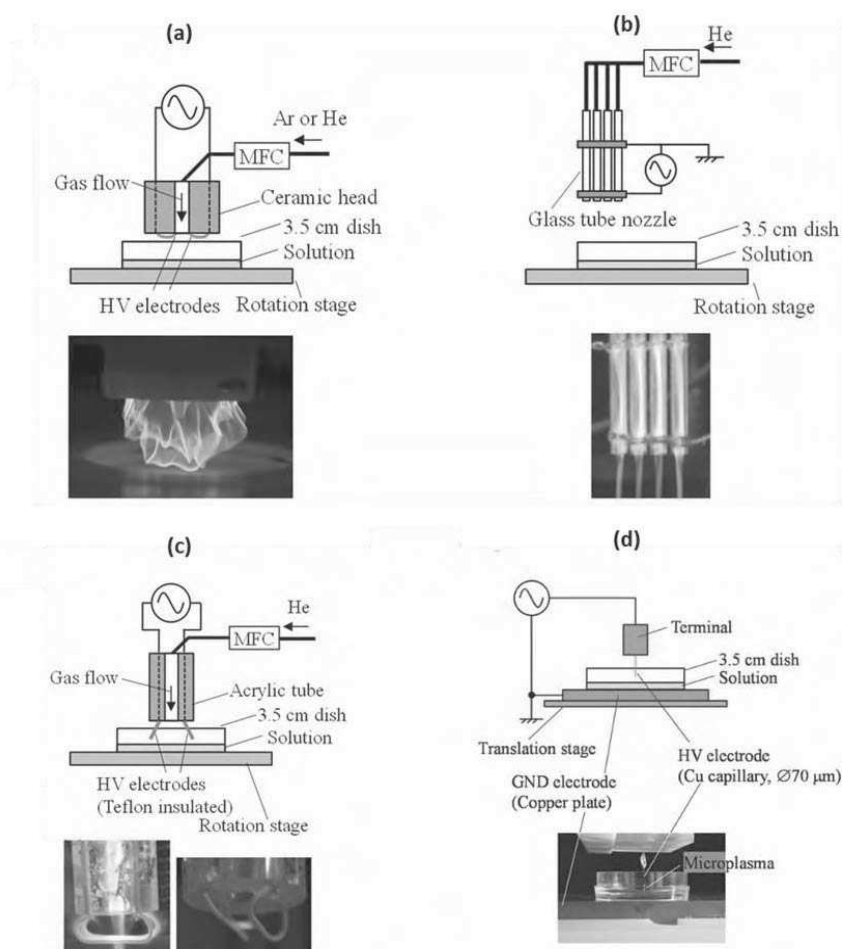


Figure 1-10 A schematic of the experimental setup for the different plasma configuration and Photograph of the generated plasma. (a) Arc plasma, (b) APJ plasma, (c) DBD, and (d) Microplasma [73].

Finally, the low-temperature microplasma configuration (cf. Figure 1-10 (d)). The HV power supply was identical to that for the arc plasma configuration. A thin copper tube was employed as the HV electrode. The outer and inner diameters of the tube were 70 and 20 μm respectively. A grounded copper plate was used as the counter electrode and was placed under the dish in order to stabilize the discharge. Without the counter electrode, the discharge becomes spatiotemporally

unstable. The distance between the HV electrode tip and the sample solution was set as 2 mm. The HV electrode was a capillary tube structure in order to flow discharge gas inside it. However, since the gas flow rate was too low and the discharge did not show gas dependency, we did not flow any gas into the capillary tube in this study. A microplasma was generated at the tip of the HV electrode as shown in the photo in Figure 1-10 (d).

In order to obtain an averaged exposure of the sample to the plasma, the used dish was rotated by 75 rpm, in the following three configurations (Arc plasma, plasma jet, and DBD). On the other hand, since the microplasma seems to be spatially and temporarily stable, the solution sample was not rotated and was fixed after alignment using an XYZ translation stage. The microplasma irradiation area was about 1 mm in diameter.

Moreover, the target cells used in the fourth considered plasma configuration were COS-7 cells, which were taken from African green monkey kidney. The cells were seeded onto a 3.5 cm dish at a density of 26,000 cells/cm² and 1.5 ml of medium (The medium consisted of D-MEM (Wako, 044-29765), penicillin-streptomycin solution (Wako, 168-23191) and fetal bovine serum (Invitrogen, 26140-079)). The cells were incubated for more than 24 h until the number of cells reached the sub-confluent under the ambient temperature of 37°C and the CO₂ concentration of 5%. After the incubation, it was confirmed that the number of cells was in a sub-confluent state and the medium was aspirated and washed 2 times with phosphate buffered saline (PBS). In addition, for plasma irradiation, the sample was made by pouring into this dish, 4.0 µg of pCX EGFP plasmid coded with GFP (Green Fluorescent Protein) diluted with 120 µl of PBS (0.033 µg/µl). Just after plasma irradiation, 1.5 ml of the same medium was added to the dish and the cells were incubated

for 24 h under the same condition mentioned above. Then they are observed by microscope (bright field and fluorescence images).

1.3.4 Comparative study on the different experimental setups tested at Ehime University for gene transfection: Transfection efficiency and cell viability

A comparative study was achieved at Ehime University in the aim to characterize the most suitable plasma configuration for gene transfection, based on the high gene transfection and cells viability rates obtained for each plasma sources [73]. For each of the plasma sources, the voltage amplitude, pulse modulation frequency, duty ratio, irradiation time, and gas flow rate were optimized, and as for the gene transfection efficiency and cell viability, the highest values were obtained. The main experimental conditions for the highest transfection efficiency and cell viability for each plasma source are listed in Table 1-1.

Figure 1-11 and Figure 1-12 show respectively; bright field/fluorescence images and experimental results of viability/transfection efficiency of the plasma treated COS-7 cells with GFP plasmid, obtained in the case of each plasma sources; (arc plasma, APJ, DBD plasma, and microplasma). In these captured images (see Figure 1-11) , the number of living cells (η_l) as well as the number of cells emitting fluorescence (η_f) were counted. The cell emitting green fluorescence which is detectable by naked eye are counted as transfected cells. Knowing that the auto fluorescence was considered to be negligible because green fluorescence was not detected when COS-7 cells without the plasmid DNA were exposed to the air microplasma. Since only shrunk or fused cells were categorized to dead cell, apoptosis-mediated cell death was not considered. The cell death was also evaluated with trypan blue stain and there was no difference between viabilities derived with and without trypan blue-stain. On the other hand, a control sample

without plasma irradiation was also prepared, incubated for 24 h, and observed, then the number of cells was counted (n_0). Finally, the average rates of survival (n_l) and the transfection (n_f) were calculated based on the following:

$$\text{Survival rate} = \frac{n_l}{n_0} \tag{Eq-1-3}$$

$$\text{Transfection rate} = \frac{n_f}{n_0} \tag{Eq-1-4}$$

Table 1-1 Experimental conditions for each plasma source

	Arc plasma	Plasma jet	DBD plasma	Microplasma
Electrical conditions				
Voltage waveform	Pulse-modulated sinusoidal	CW sinusoidal	Sub μ s-pulse	Pulse-modulated sinusoidal
Frequency (kHz)	20	14	0.1	20
Modulation frequency (pps)	25	/	/	25
Duty ratio (%)	60	/	10^{-3}	1
Voltage amplitude (kV)	2.9	3.2	18.5	6
Irradiation time (s)	1.2	15	60	5
Geometric and flow gas conditions				
Gap length between the HV electrode and the solution surface (mm)	12	6	0.1	2
Gas carrier	Argon	Helium	Helium	/
Flow rate (slm)	19.6	3.4	2.4	/

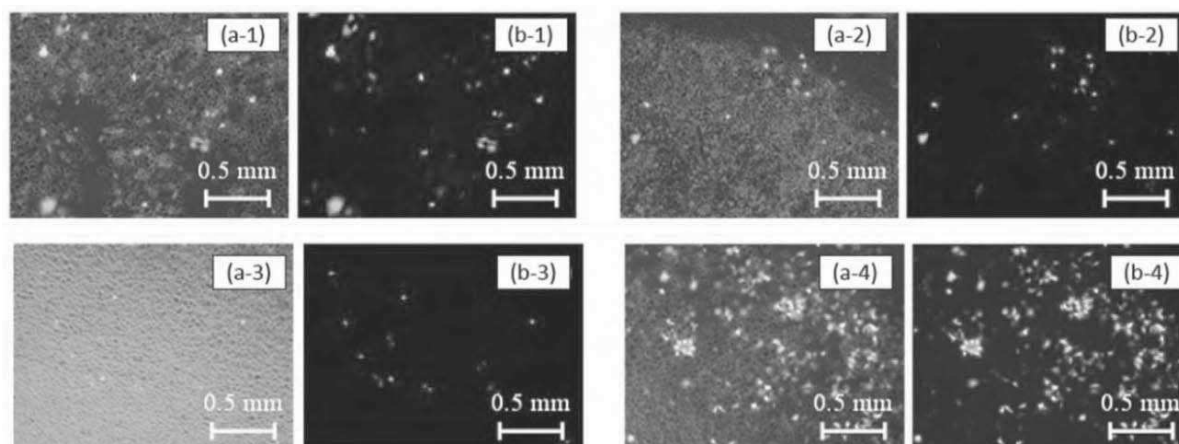


Figure 1-11 Bright-field (a) and fluorescence (b) images taken with both visible and UV light illuminations after 24 h incubations from plasma irradiation. (a-1) and (b-1) Arc plasma configuration, (a-2) and (b-2) APJ configuration, (a-3) and (b-3) DBD plasma configuration, (a-4) and (b-4) microplasma configuration [73].

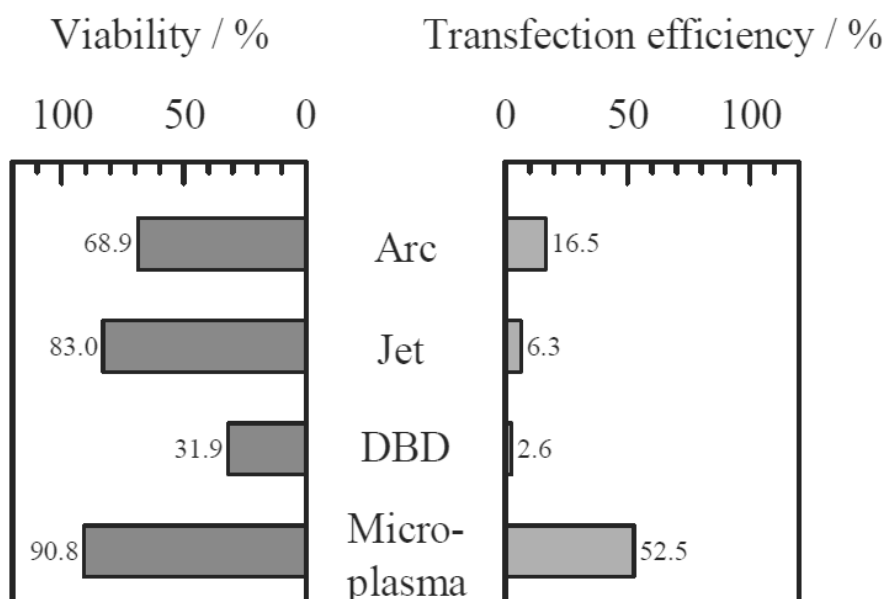


Figure 1-12 The cell viability (left) and the transfection efficiency (right) for four different plasma configurations (arc plasma jet, APJ, DBD plasma, and microplasma) [73].

It is noteworthy that each plasma source has been separately considered in order to compare the corresponding viability and transfection rates. Moreover, the considered results, were obtained under the conditions where the highest transfection rates were observed.

In the case of arc plasma irradiation, Figure 1-11 (a-1) and (b-1) show several exfoliated cells and some fused ones with each other. Indeed, it was found that the plasma irradiation gave damages to the cells, however, gene transfection rate was about 16.5% (cf. Figure 1-12). In addition, both exfoliation and fusion of cells were observed in the case of plasma jet and DBD plasma irradiation (cf. Figure 1-11 (a-2), (b-2), (a-3), and (b-3)). However, gene transfection efficiency were less than 3% (cf. Figure 1-12). On the other hand, high transfection efficiency around 52.5% was obtained by the microplasma configuration. Indeed, Figure 1-13 shows an example of fluorescent image of whole 3.5 cm dish after the microplasma irradiation. In order to obtain a wide area image, an LED transilluminator with amber filter (Wako) was used instead of the microscope.

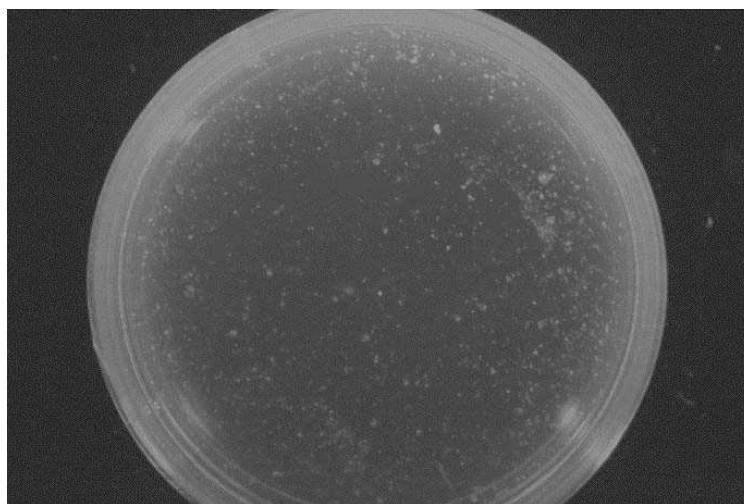


Figure 1-13 Fluorescence image of whole 3.5 cm dish after microplasma irradiation. In order to obtain a wide area image, an LED transilluminator with amber filter was used instead of the microscope. Although the microplasma irradiation area was limited (the center of the dish, ~1 mm of diameter), transfection occurred in the wide area in the dish. [73].

The experimental condition was identical to Figure 1-11 (a-4) and (b-4). Although the microplasma irradiation area was limited (the center of the dish, ~1 mm of diameter), transfection occurred in a wide area of the dish. The obtained results from the comparative study on the different plasma configurations, show that by using microplasma electrode, spatially and temporary stable microplasma can be obtained. Thus, the best rates of transfection rates 52.5% and cells survival 90.8 % were realized simultaneously [73].

1.4 Parametric investigation on gene transfection efficiency using air microplasma for different protocols

The comparative study shows that the air microplasma configuration is one of the promising gene transfection method for safe and high efficiency gene transfection. These encouraging results were attributed to the potential space and time stability of this microplasma air discharge in comparison to the other plasma sources. However, the mechanisms of gene transfection are far from to be clear and controlled. Therefore a parametric investigation on gene transfection mechanisms by microplasma discharge is conducted at Ehime university. To this purpose, several factor effects and gene transfection timing were investigated, by changing the experimental gene transfection protocols.

Recently, an investigation on gene transfection process with the air microplasma was carried out based on different experimental protocols [69]. A detailed description on the different tested protocols is presented in the following sub-section 1.4.1. As a result of this first investigation, it was found that the transfection occurs not only during plasma irradiation but also after that, suggesting the possible effects of residual radicals, the radical-induced active species or surface charges after plasma irradiation [69].

Furthermore, a more specifically investigation on the timing in which the above species are effective on the transfection was achieved [67]. In other word, is to look at the time periods where the factors become more effective. To this purpose, the samples was treated in seven different experimental protocols as show in Figure 1-15.

1.4.1 Plasma treatment protocols

Figure 1-14 displays an overview on the scheme of plasma discharge and the experimental setup used for gene transfection. As already underlined, the used plasma irradiation source was the microplasma configuration which was already described, and more detailed elsewhere [67] [69].

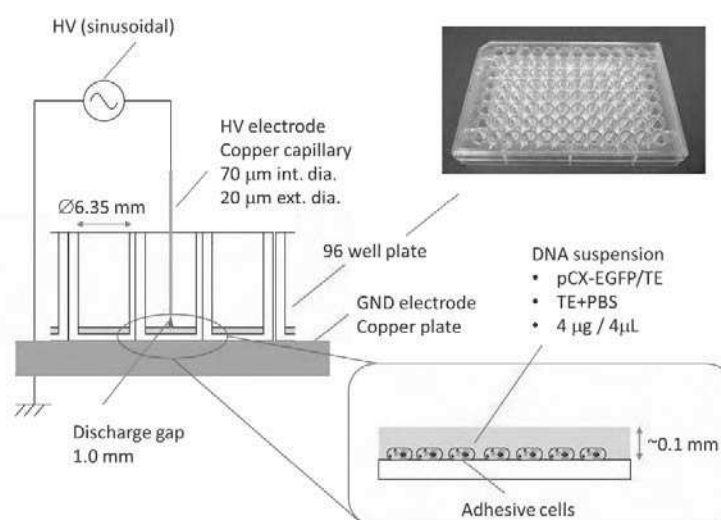


Figure 1-14 Overview on the experimental setup and conditions.

The applied voltage between the electrodes was 14 kV. The output voltage had a 20 kHz sinusoidal waveform which was pulse modulated (width =0.4 ms) at 25 Hz with a duty ratio of 1%. For the benchmark purpose of this study, a 96 well containing the cells were used instead of the petri dish previously used.

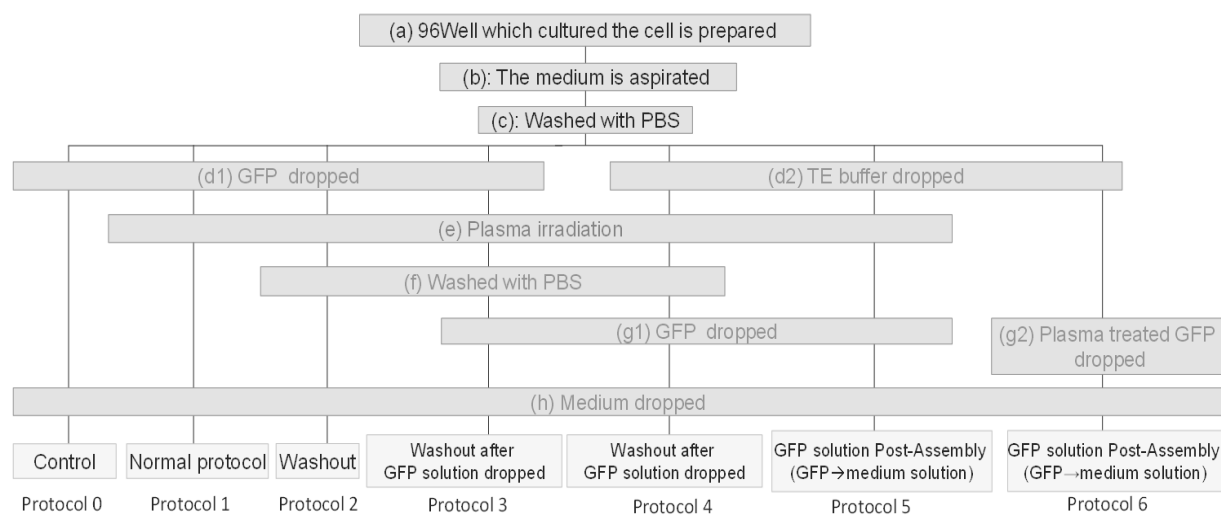


Figure 1-15 Organigram of sample treatment protocols [67].

As already noted, Figure 1-15 illustrates the 7 different protocols. The Protocol 0 represents the control samples, that is, without plasma irradiation. The Protocol 1, represents the standard plasma treatment, where both the cells and DNA plasmid are irradiated by the plasma discharge. The Protocol 2, consists on the washing out of the samples with the PBS after the plasma treatment. The aim of this washing out process is to suppress any effective factor (without After Effect) on the gene transfection after plasma treatment. Otherwise, is to consider only the direct effects of the plasma treatment. During protocol 3, after plasma treatment of both cells and DNA plasmid, and the washing out with the PBS, the GFP plasmid is re-dropped in the sample. For the Protocols 4 and 5, only cells are treated by the plasma irradiation, and the DNA plasmid is added just after the plasma irradiation (Protocol 5) (After Effect Only) or after the plasma irradiation and the washing out (Protocol 4). Finally, for the Protocol 6, just like the control (Protocol 0), no cells plasma irradiation is considered. Instead of that only the post-plasma treated DNA is poured in sample for the 24h incubation.

On the other hand, the common process steps for all the 7 protocols consists on; (a) the incubation of the COS-7 cells at 37°C under 5% carbon dioxide in D-MEM medium, (b) the aspiration of the medium, and then (c) the washing out with the PBS (phosphate buffered saline, 0.1 M, pH 7.4). In addition, after the common processes, and in the Protocols 0, 1, 2 and 3, GFP plasmid diluted with TE buffer (0.4 µg/µl) is poured into each well in Process (d1). Then in the Protocols 1, 2, and 3, each well is treated by the plasma irradiation in Process (e). After the Process (e), in the Protocol 1 the medium is poured into each well in Process (h). In the Protocols 2 and 3, after the Process (e) each well is washed by PBS in Process (f). Moreover, for the protocol 3 and after the washing process (process (f)), the GFP plasmid is re-dropped in Process (g1).

After the Process (c) in the Protocols 4, 5 and 6, 4µl of TE buffer without plasmid is poured into each well in Process (d2). In the Protocols 4 and 5, plasma treatment is done in Process (e). Following the plasma treatment in the Protocols 4 the TE buffer plasma treated solution is washed with the PBS in Process (f), and the GFP plasmid is dropped in Process (g1) in both Protocols 4 and 5. Finally, in the Protocol 6, after the Process (d2), GFP plasmid treated by the plasma irradiation is poured into the well in Process (g2). In the end of each protocol, the samples are incubated for 24 hours in Process (h), then followed by the microscope observations.

1.4.2 Discussion on plasma transfection protocols and effects

In order to estimate quantitatively the differences between the protocols in the transfection efficiency, transfection rates were calculated from the fluorescent and bright field images (cf. Figure 1-11). Then, the average transfection efficiency was estimated from the obtained results of 15 wells for each protocol (cf. Figure 1-16).

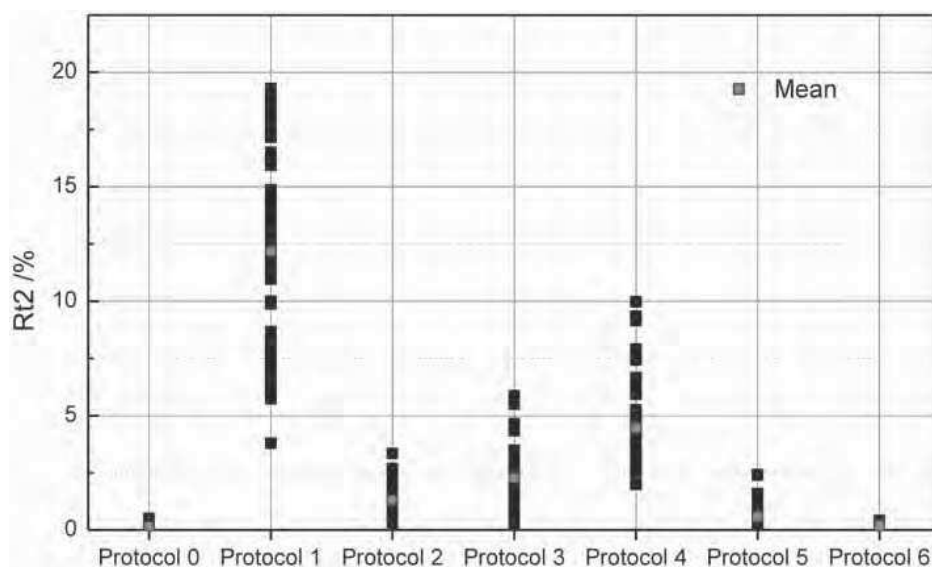


Figure 1-16 Transfection efficiency Rt_2 for each Protocol [67].

From the considered results, we notice that the standard plasma irradiation protocol (Protocol 1) shows a transfection rate around 12.2%, whereas only 0.1% transfection was obtained without plasma irradiation (Protocol 0). This difference clearly confirmed that the plasma treatment is effective to gene transfection. On the other hand, by washing out the plasma irradiated sample (Protocol 2), the transfection rate drastically dropped to 1.3%. The obtained result, gives us a quantitative estimation of the contribution rates of both direct (e.g., electric field, discharge current, charged particle, etc.) and after plasma effects (chemically reactive species, bio-chemical reactions, etc.) on gene transfection. For instance, the direct effect was estimated to be 1/10 of all the effects induced by plasma irradiation. Whereas, the major remainder 9/10 was contributed to the indirect effects (after effect) of the plasma irradiation.

By adding the GFP plasmids again after washing out (Protocol 3), the transfection rate increases double (2.3%) compared to that of Protocol 2. One possible reason for the enhancement is that residual chemical species (after effect) exist even after washing out process which induces

transfection of the GFP plasmids that are dropped after washing out. However, if GFP plasmids are not dropped before plasma irradiation (Protocol 4), the transfection rate re-increases double (4.5%) compared to that of Protocol 3. A possible reason of this enhancement is that existence of GFP plasmids decreases the stress to the cells during plasma irradiation. In addition, if the washing out process is omitted (Protocol 5), the transfection rate dropped to 0.6%. Besides the instability of washing out process mentioned above, there is a possibility that this process itself has some effect such as endocytosis enhancement. Finally, by pouring the plasma-irradiated GFP plasmids solution to the cell (Protocol 6) it does not result in the transfection (0.5%). From the comparison between Protocols 1, 2, 5 and 6, we notice that, the “after effect” is effective only when both GFP plasmids and cells are irradiated by plasma. Therefore, the “after effect” is caused not only by the residual chemically reactive species, but also by plasma irradiation stress to cells and plasmids (possibly charging effect or oxidation stress).

While summarizing, the results suggest that the principal mechanism of the gene transfection is due 9/10 to the indirect irradiation effect of plasma (chemically reactive species, electric charge and bio-chemical reactions). However, it also shows that the direct effect (e.g., charged particles) can play a second role around 1/10 of all plasma effect in the gene transfection. In other words, the gene transfection occurs effectively only with the presence of two effects direct and indirect during the treatment of both GFP plasmids and cells, suggesting a synergetic relationship between the direct and indirect effect on plasma gene transfection.

1.5 Conclusion

During this first chapter, the technique of gene transfection was presented. Indeed, this chapter was first of all devoted, on the one hand, to different applied fields of gene transfection. We realized that the manipulation of gene expression is a core technique in more research areas such

as for instance regenerative medicine, genetics therapies, cardiovascular diseases as well as the various pharmaceutical aspects. On the other hand, we presented a detailed review on the various developed gene transfection methods. For instance, the viral method which is the most commonly used method in clinical research, chemical transfection methods, most widely used in contemporary research, and the physical transfection methods, the most recent ones, using diverse physical tools to deliver nucleic acids to the target cell. For example, the electroporation is regarded as the most widely used physical technology. It's based on the application of an electric field over the cells, allowing the creation of transitory pores through which nucleic acid can pass into cells. However, it proved that each one of these used methods are limited to minority experimental systems and can have serious known drawbacks. Moreover, knowing that one of the major difficulties with gene transfection is how to effectively and safely deliver the genetic material to different cells types, we encircled the most pressing point that the field of gene transfection has to address, which is the development of efficient and safe gene delivery methods. Therefore, we were interested to the potentiality of using cold plasmas generated at atmospheric pressure for the gene transfection applications. An overview on the different plasma sources used for gene transfection, which have emerged in literature (APJ, DBD, etc., based on using helium or argon gas carrier), confirmed clearly that the cold plasma irradiation is effective to gene transfection. Indeed, it shows that the cells became transiently permeable for plasmid DNA during the plasma exposure, suggesting that the possible cold plasma transfection mechanisms by which pores are created in the cell membrane are twofold mechanisms; cell charging and lipid peroxidation. On the other hand, further literature results, predicted that the possible mechanisms of gene transfection are based on a competition between various factors such as reactive species, and plasma-induced electric field stimulation. However, it also showed us, that the plasmas may

have unexpected negative effects on cells which require a deeper understanding on the mechanism of plasma-cells interactions. More generally, I understand that, any cold plasma setup used for gene transfection, must fulfil to various criteria's, such as be able to reach the treatment zone by a stable propagation in time and space and do not damage the treated cells. In other words, is to achieve the best trade-off relationship between transfection efficacy and cell damages.

To this aim, the research team of Ehime University, developed several types of plasma sources with different designs and configurations (arc plasma discharge using argon carrier gas, atmospheric pressure plasma jet (APJ) using helium and equipped with 4 and 9 jets, dielectric barrier discharge (DBD) plasma using also helium flow, and last an air microplasma), in the aim to characterize the most suitable plasma configuration for gene transfection, based on the high gene transfection and cells viability rates. A comparative study on the different plasma setups, shows that, the best results (52.5% of transfection rate and 90.8 % of cell viability rate) are obtained in the case of air microplasma. These encouraging results were attributed to the potential space and time stability of this microplasma air discharge in comparison to the other plasma sources. Moreover, an experimental parametric study on gene transfection focused on the application of microplasma discharge, showed that nearly 1/10 of transfections occur during plasma irradiation and that the last 9/10 of transfections occur after plasma irradiation is stopped. Suggesting that, the second stage transfection is caused not only by the residual chemically reactive species, but also by plasma irradiation stress to cells and plasmids, i.e., possibly charging effect.

Thus, in the perspective to contribute to a better understanding of mechanism and the processes involved during plasma gene transfection, this thesis work will be interested, to numerically simulate the membrane permeabilization and pore formation when the cells are impacted by the air microplasma fluxes. This is achieved by developing a specific Monte Carlo poration model.

However, this model requires a prior an input database on the fluxes and the energy of the main plasma species arriving to the cell membrane. This concerns more particularly the knowledge of the density of charged particles (electrons and N_2^+ ion), and the temperature of gas and electrons. This is why the aim of the following chapter is to experimentally measure these plasma characteristics from OES in the case of air microplasma.

1.6 References

- [1] J. A. Wolff and J. Lederberg, “An Early History of Gene Transfer and Therapy,” *Hum. Gene Ther.*, vol. 5, pp. 469–480, 1994.
- [2] F.M. Wurm, “Production of recombinant protein therapeutics in cultivated mammalian cells,” *Nat. Biotechnol.*, vol. 22, pp. 1393–1398, 2004.
- [3] K. Culver, “Gene Therapy—A Handbook for Physicians,” *Nat. Med.*, vol. 1, p. 479, 1994.
- [4] A.P. Cotrim and B.J. Baum, “Gene Therapy : Some History , Applications , Problems , and Prospects,” *Toxicol. Pathol.*, vol. 36, pp. 97–103, 2008.
- [5] T. K. Kim and J. H. Eberwine, “Mammalian cell transfection: The present and the future,” *Anal. Bioanal. Chem.*, vol. 397, pp. 3173–3178, 2010.
- [6] T. Wirth, N. Parker, and S. Ylä-herttua, “History of gene therapy,” *Gene*, vol. 525, pp. 162–169, 2013.
- [7] D. Wang and G. Gao, “State of the art human gene therapy: Part I. Gene delivery technologies,” *Discov. Med.*, vol. 18, pp. 67–77, 2015.
- [8] D. Wang and G. Gao, “State of the art human gene therapy: Part II. Gene therapy strategies and applications,” *Discov. Med.*, vol. 18, pp. 151–161, 2015.
- [9] U. Griesenbach and E. W. F. W. Alton, “Moving forward: cystic fibrosis gene therapy,” *Hum. Mol. Genet.* , vol. 22 , pp. R52–R58, Oct. 2013.
- [10] C. Mueller and T. R. Flotte, “Gene-Based Therapy for Alpha-1 Antitrypsin Deficiency,” *J. Chronic Obstr. Pulm. Dis.*, vol. 10, pp. 44–49, 2013.
- [11] A. Biffi, P. Aubourg, and N. Cartier, “Gene therapy for leukodystrophies,” *Hum. Mol.*

- Genet.*, vol. 20, pp. 42–53, 2011.
- [12] D. Gaudet, J. Méthot, and J. Kastelein, “Gene therapy for lipoprotein lipase deficiency,” *Curr. Opin. Lipidol.*, vol. 23, 2012.
- [13] M. B. Sikkil, C. Hayward, K. T. Macleod, S. E. Harding, and A. R. Lyon, “SERCA2a gene therapy in heart failure: an anti-arrhythmic positive inotrope,” *Br. J. Pharmacol.*, vol. 171, pp. 38–54, 2014.
- [14] M. K. Brenner, S. Gottschalk, A. M. Leen, and J. F. Vera, “Is cancer gene therapy an empty suit?,” *Lancet Oncol.*, vol. 14, pp. 1–19, 2014.
- [15] A. C. Bradshaw and A. H. Baker, “Gene therapy for cardiovascular disease : Perspectives and potential,” *Vascul. Pharmacol.*, vol. 58, pp. 174–181, 2013.
- [16] M. Simonato, J. Bennett, N. M. Boulis, M. G. Castro, D. J. Fink, W. F. Goins, S. J. Gray, P. R. Lowenstein, L. H. Vandenberghe, T. J. Wilson, J. H. Wolfe, and J. C. Glorioso, “Progress in gene therapy for neurological disorders,” *Nat. Publ. Gr.*, vol. 9, pp. 277–291, 2013.
- [17] D. Yu, X. Hu, and H. Cai, “Efficient tuberculosis treatment in mice using chemotherapy and immunotherapy with the combined DNA vaccine encoding Ag85B , MPT-64 and MPT-83,” *gene Ther.*, vol. 15, pp. 652–659, 2008.
- [18] M. M. Rodrigues and I. S. Soares, “Gene-therapy for malaria prevention,” *Trends Parasitol.*, vol. 30, 11, pp. 511–513, 2014.
- [19] A. B. Balazs, J. Chen, C. M. Hong, D. S. Rao, L. Yang, and D. Baltimore, “Antibody-based protection against HIV infection by vectored immunoprophylaxis,” *Nature*, vol. 481, pp. 81–84, 2012.
- [20] A. B. Balazs, J. D. Bloom, C. M. Hong, D. S. Rao, and D. Baltimore, “Broad protection against influenza infection by vectored immunoprophylaxis in mice,” *Nat Biotech*, vol. 31, pp. 647–652, Jul. 2013.
- [21] C. Fellmann and S.W. Lowe, “Stable RNA interference rules for silencing,” *Nat. cell Biol.*, vol. 16, pp. 10–18, 2014.
- [22] C. Mueller, Q. Tang, A. Gruntman, K. Blumenkamp, J. Teckman, L. Song, P. D. Zamore,

- and T. R. Flotte, “Sustained miRNA-mediated Knockdown of Mutant AAT With Simultaneous Augmentation of Wild-type AAT Has Minimal Effect on Global Liver miRNA Profiles,” *Mol. Ther.*, vol. 20, pp. 590–600, 2009.
- [23] C. Madocsai, S. R. Lim, T. Geib, B. J. Lam, and K. J. Hertel, “Correction of SMN2 Pre-mRNA Splicing by Antisense U7 Small Nuclear RNAs,” *Mol. Ther.*, vol. 12, pp. 1013–1022, 2005.
- [24] M. Li, K. Suzuki, N. Y. Kim, G.-H. Liu, and J. C. I. Belmonte, “A cut above the rest: targeted genome editing technologies in human pluripotent stem cells,” *J. Biol. Chem.*, vol. 289, pp. 4594–4599, 2013.
- [25] H. Lisa Li, T. Nakano, and A. Hotta, “Genetic correction using engineered nucleases for gene therapy applications,” *Dev. Growth Differ.*, vol. 56, pp. 63–77, 2014.
- [26] J. P. Guilinger, V. Pattanayak, D. Reyon, S. Q. Tsai, J. D. Sander, J. K. Joung, and D. R. Liu, “Broad specificity profiling of TALENs results in engineered nucleases with improved DNA-cleavage specificity,” *Nat Meth*, vol. 11, pp. 429–435, 2014.
- [27] M. Yamamoto and Y. Tabata, “Tissue engineering by modulated gene delivery B,” *Adv. Drug Deliv. Rev.*, vol. 58, pp. 535–554, 2006.
- [28] T. Kushibiki and Y. Tabata, “Future Direction of Gene Therapy in Tissue Engineering,” *Top. tissue Eng.*, vol. 2, 2005.
- [29] R. Gaetano, C. Pacilio, and A. Giordano, “Gene Transfer Technology in Therapy : Current Applications and Future Goals There is an enormous variety of possible applications of gene transfer in therapy .,” *Stem Cells*, vol. 17, pp. 191–202, 1999.
- [30] A. Colosimo, K. K. Goncz, A. R. Holmes, K. Kunzelmann, M. J. Bennet, and D. C. Gruenert, “Review Transfer and Expression of Foreign Genes in Mammalian Cells,” *Biotechniques*, vol. 29, pp. 314–331, 2000.
- [31] A. Pfeifer and I. M. Verma, “GENE THERAPY: Promises and Problems,” *Annu. Rev. Genomics Hum. Genet.*, vol. 2, pp. 177–211, 2001.
- [32] D. H. Hamer, K. D. Smith, S. H. Boyert, and P. Leder, “SV40 Recombinants Coding Sequences Carrying Rabbit P-Globin Gene,” *Cell*, vol. 17, pp. 725–735, 1979.

- [33] M. Giacca and S. Zacchigna, "Virus-mediated gene delivery for human gene therapy," *J. Control. Release*, vol. 161, pp. 377–388, 2012.
- [34] M. A. Kay, "State-of-the-art gene-based therapies: the road ahead," *Nat Rev Genet*, vol. 12, pp. 316–328, 2011.
- [35] L. Vannucci, M. Lai, F. Chiuppesi, L. Ceccherini-nelli, and M. Pistello, "Viral vectors : a look back and ahead on gene transfer technology," *new Microbiol.*, vol. 36, pp. 1–22, 2013.
- [36] J. Roesler, S. Brenner, A. A. Bukovsky, N. Whiting-Theobald, T. Dull, M. Kelly, C. I. Civin, and H. L. Malech, "Third-generation, self-inactivating gp91^{phox}lentivector corrects the oxidase defect in NOD/SCID mouse–repopulating peripheral blood–mobilized CD34⁺ cells from patients with X-linked chronic granulomatous disease," *Blood*, vol. 100, pp. 4381–4390, 2002.
- [37] N. Woods, A. Muessig, M. Schmidt, J. Flygare, K. Olsson, P. Salmon, D. Trono, C. Von Kalle, and S. Karlsson, "Lentiviral vector transduction of NOD / SCID repopulating cells results in multiple vector integrations per transduced cell : risk of insertional mutagenesis," *gene Ther.*, vol. 101, pp. 1284–1289, 2003.
- [38] E.T. Schenborn and V. Goiffon, "DEAE-Dextran Transfection of Mammalian Cultured Cells," *Methods Mol. Biol.*, vol. 130, pp. 147–153, 2000.
- [39] P. Washbourne and A. K. Mcallister, "Techniques for gene transfer into neurons," *Curr. Opin. Neurobiol.*, vol. 12, pp. 566–573, 2002.
- [40] F. L. Graham, and A. J. Van Der EB, "A New Technique for the Assay Adenovirus of Infectivity of Human Adenovirus 5 DNA," *Virology*, vol. 52, pp. 456–467, 1973.
- [41] Y. Chen, "Calcium Phosphate Transfection of Eukaryotic Cells," *bio Protoc.*, vol. 1, pp. 5–7, 2011.
- [42] R. Fraley, S. Subramani, P. Berg, and D. Papahadjopoulos, "Introduction of liposome-encapsulated SV40 DNA into cells," *J. bio Chem.*, vol. 255, pp. 10431–10435, 1980.
- [43] J. Zabner, A. J. Fasbender, T. Moninger, and K. A. Poellinger, "Cellular and Molecular Barriers to Gene Transfer by a Cationic Lipid," *J. Biol. Chem.*, vol. 270, pp. 18997–19007, 1995.

- [44] I. Mortimer, P. Tam, I. Maclachlan, R. W. Graham, E. G. Saravolac, and P. B. Joshi, "Cationic lipid-mediated transfection of cells in culture requires mitotic activity," *Gene Ther.*, vol. 6, pp. 403–411, 1999.
- [45] Y. Gluzman, "SV40-transformed simian cells support the replication of early SV40 mutants," *Cell*, vol. 23, pp. 175–182, 1981.
- [46] J. Haensler and F. C. Szoka Jr, "Polyamidoamine cascade polymers mediate efficient transfection of cells in culture," *Bioconjug. Chem.*, vol. 4, pp. 372–379, 1993.
- [47] J. F. Kukowska-latallo, A. U. Bielinska, J. Johnson, R. Spindlert, D. A. Tomaliat, and J. R. Baker, "Efficient transfer of genetic material into mammalian cells using Starburst polyamidoamine dendrimers," *Proc. Natl. Acad. Sci.*, vol. 93, pp. 4897–4902, 1996.
- [48] M. X. Tang, C. T. Redemann, and F. C. Szoka, "In Vitro Gene Delivery by Degraded Polyamidoamine Dendrimers," *Bioconjug. Chem.*, vol. 7, pp. 703–714, 1996.
- [49] A. Baker, M. Saltik, H. Lehrmann, I. Killisch, V. Mautner, G. Lamm, G. Christofori, and M. Cotten "Polyethylenimine (PEI) is a simple , inexpensive and effective reagent for condensing and linking plasmid DNA to adenovirus for gene delivery," *gene Ther.*, vol. 4, pp. 773–782, 1997.
- [50] O. Boussif , F. Lezoualc'h, M.A. Zanta, M. D. Mergny, D. Scherman, B. Demeneix, J. P. Behr, "A versatile vector for gene and oligonucleotide transfer into cells in culture and in vivo: Polyethylenimine," *Proc. Natl. Acad. Sci.*, vol. 92, pp. 7297–7301, 1995.
- [51] H. Pollard, J. S. Remy, G. Loussouarn, S. Demolombe, J. P. Behr, and D. Escande, "Polyethylenimine but Not Cationic Lipids Promotes Transgene Delivery to the Nucleus in Mammalian Cells *," *J. Biol. Chem.*, vol. 273, pp. 7507–7511, 1998.
- [52] A. V. Zelenin, A. A. Alimov, I. A. Zelenina, M. L. Semenova, M. A. Rodova, B. K. Chernov, and V. A. Kolesnikov, "Transfer of foreign DNA into the cells of developing mouse embryos by microprojectile bombardment," *FEBS Lett.*, vol. 315, pp. 29–32, 1993.
- [53] S. Mehier-Humbert and R. H. Guy, "Physical methods for gene transfer: Improving the kinetics of gene delivery into cells," *Adv. Drug Deliv. Rev.*, vol. 57, pp. 733–753, 2005.
- [54] H. J. Kim, J. F. Greenleaf, R. R. Kinnick, J. T. Bronk, and M. E. Bolander, "Ultrasound-mediated transfection of mammalian cells," *Hum. Gene Ther.*, vol. 7, pp. 1339–1346, 1996.

- [55] Y. Ogawa, N. Morikawa, A. Ohkubo-Suzuki, S. Miyoshi, H. Arakawa, Y. Kita, and S. Nishimura, "An epoch-making application of discharge plasma phenomenon to gene-transfer.," *Biotechnol. Bioeng.*, vol. 92, pp. 865–70, Dec. 2005.
- [56] Y. Sakai, V. Khajooee, Y. Ogawa, K. Kusuhara, Y. Katayama, and T. Hara, "A novel transfection method for mammalian cells using gas plasma.," *J. Biotechnol.*, vol. 121, pp. 299–308, Feb. 2006.
- [57] M. R. Capecchi, "High efficiency transformation by direct microinjection of DNA into cultured mammalian cells," *Cell*, vol. 22, pp. 479–488, 1980.
- [58] T. M. Klein and S. Fitzpatrick-Mcelligott, "Particle bombardment: A universal approach for gene transfer to cells and tissues," *Curr. Opin. Biotechnol.*, vol. 4, pp. 583–590, 1993.
- [59] J. A. O. Brien and S. C. R. Lummis, "Biolistic transfection of neuronal cultures using a hand-held," *Nat. Protoc.*, vol. 1, pp. 977–981, 2006.
- [60] N. S. Yang and W. H. Sun, "Gene gun and other non-viral approaches for cancer gene therapy," *Nat Med*, vol. 1, pp. 481–483, 1995.
- [61] F. Klein, T. Laroche, M. E. Cardenas, J. F. Hofmann, D. Schweizer, and S. M. Gasser, "Localization of RAP1 and topoisomerase II in nuclei and meiotic chromosomes of yeast," *J. cell Biol.*, vol. 117, pp. 935–948, 1992.
- [62] Y. Shirahata, N. Ohkohchi, H. Itagak, and S. Satomi, "New Technique for Gene Transfection Using Laser Irradiation," *J. Investig. Med.*, vol. 49, pp. 184-190, 2001.
- [63] H. Schneckenburger, A. Hendinger, R. Sailer, W. S. L. Strauss, and M. Schmitt, "Laser-assisted optoporation of single cells," *J. Biomed. Opt.*, vol. 7, pp. 410–416, 2002.
- [64] M. Wallace, B. Evans, S. Woods, R. Mogg, L. Zhang, A. C. Finnefrock, D. Rabussay, M. Fons, J. Mallee, D. Mehrotra, F. Schödel, and L. Musey, "Tolerability of Two Sequential Electroporation Treatments Using MedPulser DNA Delivery System (DDS) in Healthy Adults," *Mol. Ther.*, vol. 17, pp. 922–928, 2009.
- [65] M. Leduc, D. Guay, S. Coulombe, and R. L. Leask, "Effects of Non-thermal Plasmas on DNA and Mammalian Cells," *Plasma Process. Polym.*, vol. 7, pp. 899–909, 2010.
- [66] T. Nakajima, H. Yasuda, H. Kurita, K. Takashima, and A. Mizuno, "Generation of

- Bactericidal Factors in the Liquid Phase and Approach to New Gene Transfer Technology by Low-temperature Plasma Jet Treatment,” *Int. J. Plasma Environ. Sci. Technol.*, vol. 5, pp. 42–49, 2011.
- [67] Y. Ikeda, H. Motomura, Y. Kido, S. Satoh, and M. Tachibana, Kunihide Jinno, “Effect of the radical species for gene transfection by discharge plasma irradiation,” in Abst. 22nd International Symposium on Plasma Chemistry ISPC (P-III-10-10), 2015.
- [68] H. Arakawa, M. Fukagawa, S. Miyoshi, N. Morikawa, S. Nishimura, Y. Ogawa, A. Ohkubo, S. Satoh, and J. Zenkou, “ Method of transferring selected molecules,” Patent Number WO/2002/0647672002.
- [69] M. Jinno, Y. Ikeda, H. Motomura, Y. Kido, K. Tachibana, and S. Satoh, “The Necessity of Radicals for Gene Transfection by Discharge Plasma Irradiation,” *J. Photopolym. Sci. Technol.*, vol. 27, pp. 399–404, 2014.
- [70] M. Leduc, D. Guay, R. L. Leask, and S. Coulombe, “Cell permeabilization using a non-thermal plasma,” *New J. Phys.*, vol. 11, pp. 1-12, 2009.
- [71] M. Jinno, Y. Ikeda, H. Motomura, Y. Kido, and S. Satoh, “Investigation of plasma induced electrical and chemical factors and their contribution processes to plasma gene transfection,” *Arch. Biochem. Biophys.*, In press, pp. 1-8, 2016.
- [72] Y. Ikeda, H. Motomura, Y. Kido, S. Satoh, and M. Jinno, “Effects of molecular size and chemical factor on plasma gene transfection,” *Japanese J. Appl. Physics*, vol. 55, pp. 07LG06-5 2016.
- [73] M. Jinno, K. Tachibana, H. Motomura, N. Saeki, and S. Satoh, “Improvement of efficiency and viability in plasma gene transfection by plasma minimization and optimizing electrodes configuration,” *Japanese J. Appl. Physics*, vol. 55, pp. 07LG06-6, 2016.
- [74] S. Sasaki, M. Kanzaki, and T. Kaneko, “Highly efficient and minimally invasive transfection using time-controlled irradiation of atmospheric-pressure plasma,” *Appl. Phys. Express*, vol. 7, 2014.

CHAPTER 2

EXPERIMENTAL CHARACTERIZATIONS BY OPTICAL EMISSION SPECTROSCOPY OF AIR MICROPLASMA USED FOR GENE TRANSFECTION

2.1 Introduction

The Monte Carlo poration model requires in particular the knowledge of the fluxes and the energy of the main species emanating from the successfully low-temperature microplasma and impacting the membrane structure. In others words, it requires the use of some plasma diagnostic and characterization tools such as experimental optical emission spectroscopy (OES). Indeed, OES is a well-established, non-intrusive diagnostic method to investigate temperatures and densities of some excite species within plasmas. The spectra emitted by the plasma involve many important information on the estimation of plasma parameters such as rotational T_{rot} , vibrational T_{vib} and electron T_e temperatures and the identification of existing excited active species (charged particles, atoms, molecules, radicals) as well as their population density in some peculiar case when calibration is possible.

In this chapter, and after the description of the experimental setup used for the optical emission spectroscopy measurements, I am first interested by the determination of rotational T_{rot} and vibrational T_{vib} temperatures of the air microplasma by comparing experimental and synthetic

spectra of specific UV molecular emission bands. Indeed, OH (A-X), N_2^+ first negative system (FNS: 0, 0) at 391.4 nm and N_2 second positive system (SPS: 0, 0) at 337 nm are considered in the case of T_{rot} estimations. In addition, N_2^+ (FNS: 0, 0) and N_2^+ (FNS: 1, 1) head bands at respectively 391.4 nm and 388.4 nm allow us the estimations of T_{vib} . Furthermore, the electron temperature T_e is estimated from an interesting approach based on experimental ratio of the closest nitrogen emission spectra N_2 (SPS: 2, 5) at 394.4 nm and N_2^+ (FNS: 0, 0) at 391.4 nm. This is based on one hand, on a balance equation between creations and losses of excited upper levels of these two UV spectra and on the other hand, on the electron impact rates of the creation of these upper levels calculated from solution of multi-term Boltzmann equation in humid air.

Then, the densities of plasma charged particles are estimated. First, by using the measured H α spectrum, electron density n_e versus the inter-electrode position is estimated from Stark broadening under our gas temperature condition. In addition, the density of molecular nitrogen ion in its background state $N_2^+(X^2\Sigma^+_g)$ is also estimated from the experimental ratio of the intensities of the two close previous molecular nitrogen emission bands N_2 (SPS: 2, 5) at 394.4 nm and N_2^+ (FNS: 0, 0) at 391.3 nm. This ratio intensity will be correlated to the density of background states ion $N_2^+(X^2\Sigma^+_g)$ and neutral molecule $N_2(X^1\Sigma^+_g)$ assuming an *a priori* known excitation temperature T_{ex} .

The present experimental plasma characteristics can be used for a better understanding of the mechanisms and the processes involved during plasma gene transfection. It have been used as input data for the specific Monte Carlo poration model developed to simulate the membrane permeabilization and pore formation when the cells are impacted by the present microair plasma fluxes.

2.2 Experimental setup used for plasma spectroscopy measurements

Figure 2-1 displays a scheme of the experimental setup used for plasma spectroscopy measurements and a picture of the generated plasma discharge. The configuration of the studied plasma source is identical to the one already tested for gene transfection and described in chapter 1. A SUS 304 tube of 0.2 mm inner diameter and 0.7 mm for outer diameter (22 G injection needle without bevel) was used for the HV (high voltage) electrode. A copper plate was used as the grounded (GND) electrode. A Petri dish with diameter of 3.5 cm made of polystyrene was placed on the GND electrode. The dish was filled with deionized water to simulate low conductivity buffer solution (Tris-EDTA used in reference [1]). Reproducibility of emission spectra with and without cells and buffer solutions was confirmed, this is why we have not used cells and buffer solutions for running spectra to save measurement costs. A corona discharge was initiated between the tip of the HV electrode and the water surface. The discharge gap length was set at 2 mm. The applied voltage waveform was sinusoidal with the frequency of 20 kHz. The typical amplitude was fixed at 7 kV. The duration of the HV voltage application was set at 0.1 s with a repetition frequency of 1 Hz.

The optical emission spectra collected from the microplasma between the tip of the HV electrode ($z = 0$ mm) and the water surface ($z = 2$ mm) were measured in order to analyze the axial distribution of the plasma characteristics. The actual size of the microplasma image was projected on the optical fiber using biconvex lens with focal length of 72 mm (see Figure 2 2). The opening diameter of the optical fiber was 0.2 mm, which determines the special resolution. In fact, to collect the light along the inverted plasma image made by the lens on the level of the optical fiber entrance, we used a standard $4 \times f$ setup. Therefore, for each specific position of the plasma ($z = 0$ mm,

used to increase the sensitivity. The focal length of the spectrometer was 250 mm and the grating line density was 1200 mm^{-1} . The FWHM of the instrumental function at the slit width of 0.15 mm was derived as 0.4 nm at 632.8 nm. A gated ICCD (image intensified CCD) camera (Andor, iStar) was used for record the emission spectra. The gate width was set at 0.12 s and the HV voltage application for the plasma initiation was synchronized to the gate signal in order to cover the whole duration of plasma exposure (0.1 s). The emission spectra from 100 times of plasma exposure were accumulated and recorded by the ICCD camera.

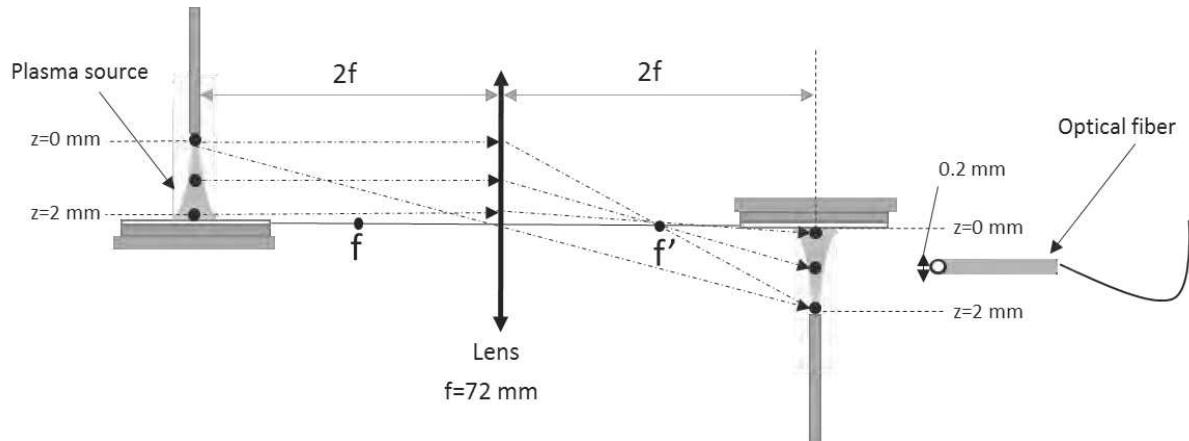


Figure 2-2 Schematic representation of the setup of plasma light collection along the z axis of the image through the lens of the air microplasma.

2.3 Results and discussion

2.3.1 Determination of rotational temperature T_{rot}

The chemistry of the discharge is significantly influenced by the neutral gas temperature T_g since it governs the reaction rate of active species generated through dissociation, excitation, and ionization processes. The rotational temperature T_{rot} is related to collisions between heavy particles such as neutrals and molecules, owing to the fast rotational relaxation, and thus can be seen as an indicator of the gas temperature T_g in non-equilibrium plasmas. Various transitions of O_2 , N_2 , N_2^+ ,

NO (dry air) and OH (humid air) can be used for the determination of the rotational temperature, depending on the level of plasma excitation [2]. In low-temperature humid air plasmas, the emission spectrum of the OH (A-X) transition between 306 to 310 nm provides a particularly convenient way to measure the rotational temperature. At higher temperatures, or in the presence of an electric field, the OH transition is overlapped by strong emission from $N_2(C-B)$ of second positive system. In this case, the rotational temperature can be measured from $N_2(C-B)$ rotational lines. At even higher temperatures or higher electric field excitation, many molecular transitions appear in the spectrum and an accurate spectroscopic model is required to extract individual lines of a particular system [2]. In the case of our microplasma discharge, three radiation transitions were chosen to estimate the rotational temperature: the second positive band system of homonuclear molecule N_2 ($C^3\Pi_u - B^3\Pi_g, v=0, v'=0$), the first negative band system $N_2^+(B^3\Pi_u - X^3\Pi_g, v=0, v'=0)$ and the ultraviolet band system of OH ($A^2\Sigma^+ - X^2\Pi_i, v=0, v'=0$) transitions. The N_2 , N_2^+ and OH rotational temperature estimation methods are described in the following sub-sections 2.3.2.

2.3.2 Estimation of T_{rot} from N_2 (SPS) and N_2^+ (FNS) emission spectra

Nitrogen is a diatomic molecule, thus having several excitation modes: electronic, vibrational and rotational. Electronic excitation is a change in the electronic energy levels, according to the energy level pattern shown in Figure 2-3. The changes in the electronic level are generally accompanied by a change in the vibrational level according to the Frank-Condon principle [3][4]. Vibrations are relative motions of the atomic nuclei composing the molecule, whereas rotations are collective motions of all the atomic nuclei of the molecule. The two latter are sub-levels of the electronic states. The de-excitation from a selected state leads to a specific photon of the exact

energy between the two states. The de-excitation from a ro-vibrational state leads to many different wavelengths, thus creating the bands seen in Figure 2-4. The transition probability between two states is called the Einstein coefficient of spontaneous emission, and can be found in literature, such as in [4].

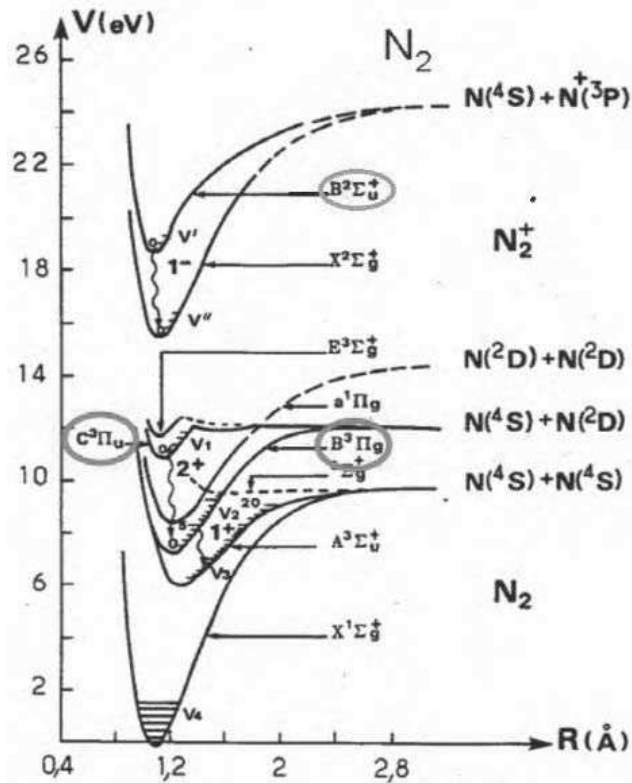


Figure 2-3 Energy diagram of the nitrogen molecule.

Figure 2-3 displays the classical energy diagram of the nitrogen molecule. We can notice the main electronic states of the neutral molecule N_2 (B) and N_2 (C) (surrounded with red circles), and the radiative electronic state of the molecular ion N_2^+ (B) (surrounded with green circle). The main electronic levels have different energies: N_2 (B) 7.35 eV and N_2 (C) 11.03 eV; and at higher energy the molecule is ionized with a threshold energy of 15.58 eV (background level of the ion) or 18.75 eV (excited ion). Each electronic state has ro-vibrational states. The excited species emit

light at a specific wavelength depending on the energy of the upper and lower excitation levels. Two distinct regions can be drawn on a typical spectrum (see Figure 2-4) obtained with our microplasma discharge, the major nitrogen components are: The SPS is the region from 300 nm to 400 nm, corresponding to the de-excitation from the $N_2(C)$ into the $N_2(B)$ state, and the first negative system FNS from the molecular ion $N_2^+(B)$ into the $N_2^+(X)$, corresponding to molecular bands not far from 400 nm.

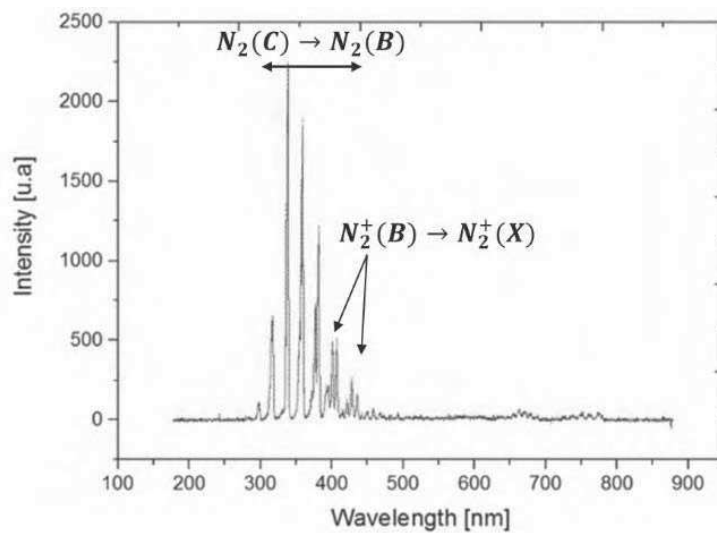


Figure 2-4 Spectrum of N_2 second positive band system SPS and N_2^+ first negative band system FNS by microplasma discharge.

The N_2 (SPS) and N_2^+ (FNS) are one of the most extensively studied band systems. Moreover, these spectra are often used for determination of the gas temperature in atmospheric pressure plasmas by analyzing their rotational structures[2][5]. Indeed, as already stated and due to the low energies needed for rotational states and in the presence of thermal equilibrium, the gas temperature T_g can be associated to the rotational temperature T_{rot} of N_2 (SPS) and N_2^+ (FNS). This association is possible since the relaxation time between rotation and translation energies is very short. However, in the cases of non-thermal equilibrium in filamentary discharges present in our

air microplasma, T_{rot} can be substantially different from gas temperature as it will be seen later. Anyway, we estimated the rotational temperature of our microplasma discharge by comparing the experimentally measured spectra with the simulated synthetic spectrum of the N_2 SPS ($C^3\Pi_u-B^3\Pi_g, v=0, v'=0$) in the range 335.5-337.5 nm, with the head band at 337 nm and N_2^+ FNS($B^3\Pi_u-X^3\Pi_g, v=0, v'=0$) transition emission bands in the range 388-392 nm, with the head band at 391.3 nm. On the other hand, a commercial code of SPECAIR [6] was used to generate the synthetic spectrum of N_2 (SPS : 0,0), while that of N_2^+ (FNS : 0, 0) was generated using a free code of LIFbase [7]. The simulated spectra were calculated to minimize the sum of square error between the measured and those calculated by choosing the best fit for the instrumental function and the rotational temperature. The temperature assuring the best fit between experimental and synthetic spectra was taken as T_{rot} . On the other hand, the instrumental function was tuned for each emission spectrum as follows to obtain the best fitting results. A trapezoid instrumental function with the top width of 25 pm and the bottom with of 80 pm was used for N_2 (SPS) spectrum generation (Specair). A Gaussian profile of the instrumental function with FWHM of 20 pm and 30 pm was used for N_2^+ (FNS) spectrum (LIFbase). For a rotational temperature T_{rot} of 700 K for N_2 (C) and 2000 K for N_2^+ (B), the simulation results show a good agreement with the measured spectra (see Figure 2-5 (a) and 2-5 (b)). The noticed significant non-equilibrium among these molecules N_2 and N_2^+ , will be discussed in the end of this sub-section 2.3.1.

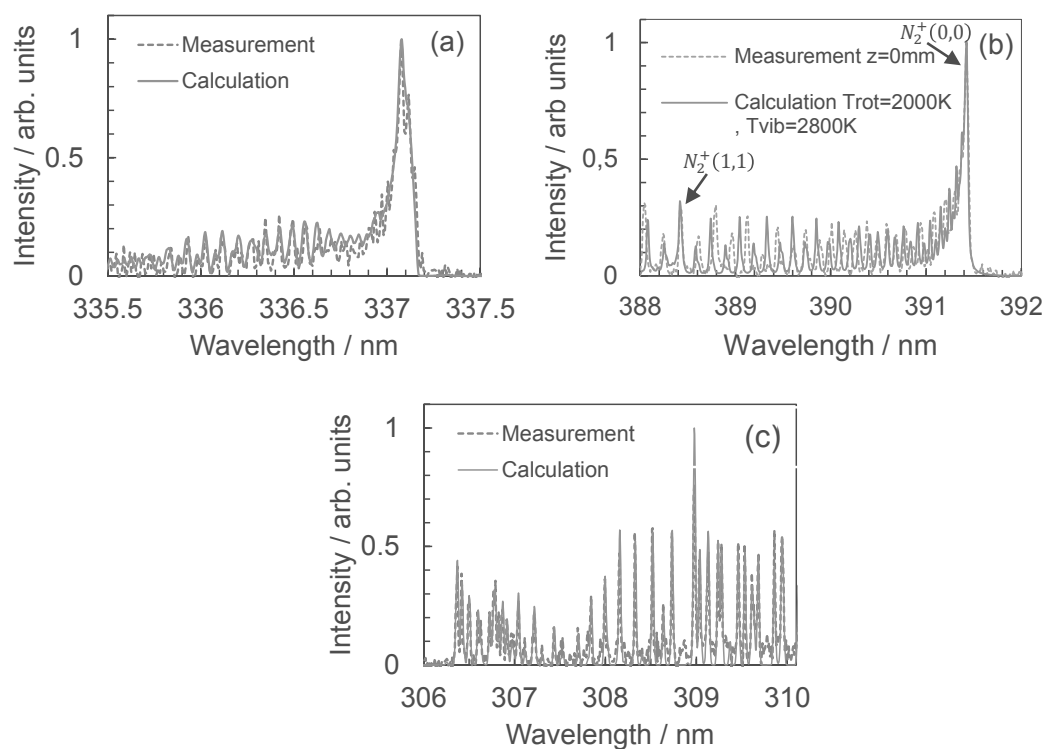


Figure 2-5 Measured and calculated emission spectra for (a) N_2 ($C^3\Pi_u$ ($v=0$) - $B^3\Pi_g$ ($v'=0$)), (b) N_2^+ ($B^3\Pi_u$ ($v=0$) - $X^3\Pi_g$ ($v'=0$)) and (c) OH ($A^2\Sigma^+$ ($v=0$) - $X^2\Pi$ ($v'=0$)) systems. A Rotational temperatures T_{rot} of 700 K for $N_2(C)$ state, 2000 K for $N_2^+(B)$ and 2350 K for OH A state were derived by fitting.

2.3.2.1 Estimation of T_{rot} from OH ultraviolet band system

The OH (A–X) transition is one of most intense systems emitted by low-temperature air plasmas sources containing even a small amount ($\sim 1\%$) of H_2 or H_2O [2]. It corresponds to radiative transitions between the first electronically excited state $A^2\Sigma^+$ and the ground state $X^2\Pi_i$, at 4.046 eV and the ground energy level. The OH ultraviolet band can be obtained under various experimental conditions, and can be easily isolated in order to give useful information on the rotational temperature T_{rot} . Indeed, this technique provides a sensitive thermometer since the OH band shape is more sensitive than that of N_2 band shape with variation of rotational temperature. Another advantage of this technique is that it does not require absolute or relative intensity

calibration because the response of usual detection systems is nearly constant over the small spectral range of interest. However, one should be aware of potential difficulties associated with self-absorption, non-Boltzmann rotational population distribution, and interferences with other species present in the plasma [2]. For the determination of rotational temperature, we are interested in the spectral range from 306.48 to 310 nm, covering the ($A^2\Sigma^+ - X^2\Pi$, $v'=0$, $v''=0$) band. The rotational temperature was obtained by fitting the experimentally spectrum with the simulated one on the entire band of OH (A-X) (see Figure 2-5 (c)). LIFbase code was used for calculations of synthetic spectra. Moreover, as in the case of N_2^+ synthetic spectrum, a Gaussian profile of the instrumental function with FWHM of 20 pm and 30 pm was used for generation of OH(A-X) spectrum. The derived T_{rot} was around 2350 K for OH (A).

The estimation of the rotational temperatures from these molecular spectra of N_2 (SPS), N_2^+ (FNS) and OH(A-X), show a significant non-equilibrium. Indeed, Bruggeman et al. have reported significant differences between the rotational temperatures of OH(A) and N_2 (C) in plasmas contacting with liquids even in the atmospheric pressure ([8],[9]). This phenomenon is attributed to overpopulation of high rotational states. This is also true for N_2^+ (B) upper state. They explained this phenomenon as follows: the rotational population distribution of OH(A) is influenced by the formation process of OH(A), i.e. dissociative recombination of H_2O^+ or H_3O^+ and dissociative excitation of H_2O . Fast quenching rate of OH(A) also inhibits its thermalization [10]. Therefore, the rotational temperature of OH(A) does not relax to the gas temperature T_g and stay at high values. An alcohol thermometer (Nihon Keiryoki, JC-2050) was placed on the GND electrode when exposed to the microair plasma to estimate the gas temperature. The temperature of the thermometer increased and reached thermal equilibrium after 5 min of plasma exposure. The final temperature was 300 K (5 K higher than the initial value). A thermocouple was not used

because strong spark discharge occurred between the HV electrode and the thermocouple. It is suggested that the rotational temperatures of $N_2(C)$ and $N_2^+(B)$ are not also in equilibrium with the gas temperature.

To summarize, the rotational temperatures measured near the anodic tip (for $z=0$ mm) are equal to 2350 K using OH (A-X), 2000 K using N_2^+ (B-X) at 391.4 nm and 700K using N_2 (SPS) at 337 nm. These high T_{rot} in comparison to T_g (300K) are representative of the corresponding excited species generated only inside the thin streamer filaments (around $50\mu\text{m}$ of diameter [11]) propagating from the tip of the high voltage electrode. In fact, these relatively high temperatures do not really affect the ambient temperature of background gas which remains at about 300 K. This is due to an important dilution of these excited species because their densities are very low in comparison to the gas density since we are in the framework of a weakly ionized gas having an ionization degree close to 10^{-5} [11].

2.3.3 Determination of vibrational temperature T_{vib} from N_2^+ (FNS) spectra at 388.4 and 391.4 nm

The vibrational temperature T_{vib} was determined from the N_2^+ (FNS) spectra using N_2^+ (FNS: 1, 1) at 388.4 nm and N_2^+ (FNS: 0, 0) at 391.4 nm. T_{vib} is estimated from the comparison of these two FNS measured spectra with the calculated ones using LIFBase software [28]. The best fit is obtained for a couple of T_{rot} and T_{vib} that are displayed in Table 2-1 versus five different positions of the inter-electrode space between the anodic tip and the cathode plate. T_{vib} is around 3000 K near the tip and increases up to about 7000 K near the plate. This T_{vib} rise is probably due to the increase of vibration-vibration collision frequency that producing high vibration levels when the micro air plasma gradually crosses the gap from the anodic tip to the cathode plate. Furthermore, as it is known T_{rot} depends on the energy transfer between heavy species of the

considered air plasma. Therefore, this is certainly why T_{rot} remains quasi-constant between the anodic tip to the cathode plate because the temperature of the dominant heavy particles is quasi-invariant along the z axis. This is different for T_{vib} behavior since it is initiated by electron impacts and also depends on many other processes such as vibration-vibration and vibration-translation interactions (see e.g. ref [12]). Therefore, the position dependence of T_e (detailed in next subsection 2.3.4) necessarily affects the position dependence of T_{vib} .

Table 2-1 Rotational and vibrational temperatures determined from $N_2^+(FNS)$ spectra for several positions of the inter-electrode space in the case of micro air plasma ($z=0mm$ corresponds to the anodic tip and $z=2 mm$ to the cathode plate)

z (mm)	T_{rot} (K)	T_{vib} (K)
0	2000	2800±500
0.5	2000	3500 ±500
1	2000	4500 ±500
1.5	2000	5500 ±500
2	2000	6500 ±500

Moreover, T_{vib} is obtained when there is a good agreement both for the intensity ratio $I_{N_2^+(FNS:0,0)}/I_{N_2^+(FNS:1,1)}$ of measured and calculated spectra and for the rotational bands of measured and calculated spectra of $N_2^+(FNS: 0,0)$ which depend on T_{rot} . We also used the comparison between the surface covered by the experimental and synthetic spectra that corresponds in fact to the integral of the normalized spectra over the wavelength. An example of comparison of these $N_2^+(FNS: 1, 1)$ at 388.4 nm and $N_2^+(FNS: 0, 0)$ at 391.4 nm is shown in Figure 2-5(b).

2.3.4 Determination of electron temperature T_e from N_2 (SPS) and N_2^+ (FNS) emissions

The electron temperature is the translational temperature of free electrons. It is among the most fundamental parameter in gas plasma discharges and plays a very important role in understanding the discharge physics and optimization of the operation of plasma [13]. Different methods are available to measure the electron temperature of which the most commonly used are Langmuir probe, microwave interferometer, Laser Thomson Scattering (LTS) and optical emission spectroscopy (OES) [14].

At atmospheric- pressure plasma discharges, both the probe and the microwave based methods are difficult to use due to the small plasma dimension and strong collision process [13] while the LTS laser technique which is well adapted for our air microplasma requires a specific setup that we do not have in our laboratory. Therefore, we used an OES approach based on nitrogen spectra and data analysis for measurements of electron temperature T_e along the z axis of our air microplasma used for gene transfection. This interesting OES approach requires first the use of the two close molecular nitrogen emission bands $N_2(\text{SPS})(C^3\Pi_u, v=2, v'=5)$ and $N_2^+(\text{FNS})(B^2\Sigma_u^+, v=0, v'=0)$ with head bands at respectively 394.3 nm and 391.4 nm (see Figure 2-6).

More precisely, it is based on relation between the ratio of these measured head band intensities spectra and more particularly the electron rate coefficients of creations and losses of $N_2(C^3\Pi_u)$ and $N_2^+(B^2\Sigma_u^+)$ upper states and the electron temperature T_e .

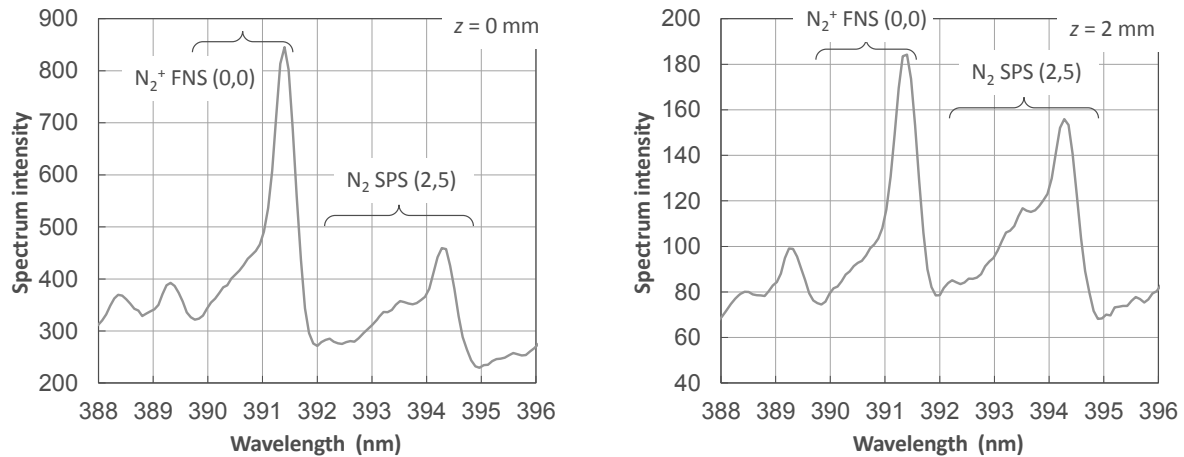


Figure 2-6 N_2 (SPS: 2, 5) and N_2^+ (FNS: 0, 0) spectra with head band at respectively 394.3nm and 391.4 nm emitted near the tip ($z=0\text{mm}$) and the plate ($z=2\text{mm}$) of micro air plasma used for gene transfection at Ehime University.

In fact, there are in the literature similar methods to obtain electron temperature from optical emission spectra (OES). The reader can find in the typical review of Zhu et al 2010 [15] an overview on such methods. There is for instance an emphasis on the so-called corona model method which has some similitudes with the present method such as:

- The studied two emissive states that are populated only by electron impacts and depopulated by radiative decays.
- The use of balance equation to obtain a relation between ratio of emissive states and excitation rate coefficients.
- The use of the T_e dependence of excitation rate coefficients.

But, the present work approach involves some differences with the literature such as:

- The emissive states are depopulated by both radiative decays and also collisional quenching.
- The excitation rate coefficients are calculated without assuming a Maxwell distribution for electrons but are accurately calculated from Multi-term solution of Boltzmann equation [16].

It is known that in molecular gases such as N_2 or O_2 , electron energy distribution (EEDF) can substantially deviate from a Maxwellian distribution particularly in the high energy region (or for the distribution tail) that strongly affects the accuracy of excitation rate coefficients [17].

- The use of two emissive states having close wavelengths (N_2^+FNS at 391 nm and $N_2 SPS$ at 394 nm) in order to fulfill the conditions detailed in subsection 2.3.4.3 and allowing to get a direct relation between ratio of spectra intensities and electron temperature via the excitation rate coefficients (see Eq-2-8 and subsection 2.3.4.3).

The present approach to determine T_e from $N_2 (SPS)$ and $N_2^+ (FNS)$ emission spectra is detailed in the following.

2.3.4.1 Reactions involved in creations and losses of upper levels of $N_2(SPS)$ and $N_2^+(FNS)$ emissions

The considered microplasma behaves as air corona discharges. It is a low-temperature and non-equilibrium plasma with a low ionization degree. It is in fact a weakly ionized gas in which the most energetic particles are electrons impacting a background gas that remains at a temperature close to ambient one.

On the basis of such considerations, we assumed that the reactions contributing to the creation of the upper levels of second positive system $N_2 (C \ ^3\Pi_u, v'=2, v''=5)$ and first negative system $N_2^+(B \ ^2\Sigma_u^+, v'=0, v''=0)$ emissions of molecular nitrogen (see Figure 2-7) are mainly populated by direct electron impacts, while these upper levels are lost following specific radiative de-excitation and collisional quenching. These reactions of creation and loss of these excited species are summarized in the following.

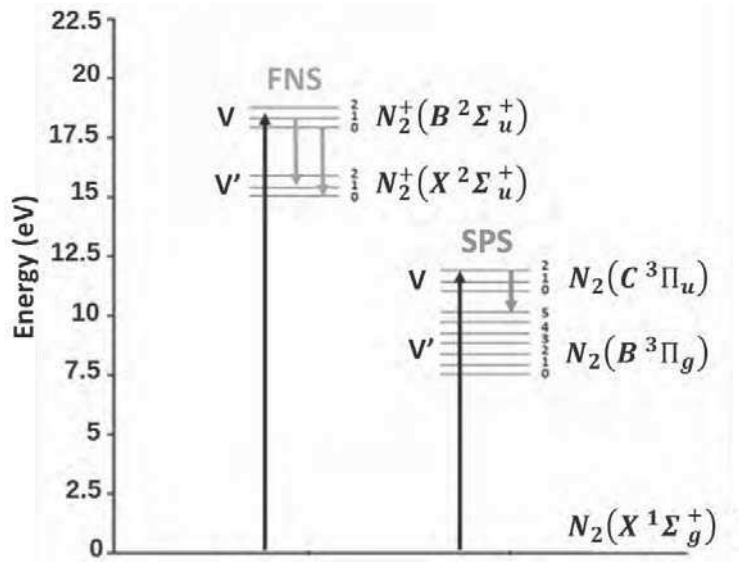


Figure 2-7 Schematic diagram of molecular transition leading to N_2 (SPS) and N_2^+ (FNS) emissions.

A. Electron impacts

Among the various inelastic collisions occurring between electrons and nitrogen ground state $N_2(X^1\Sigma_g^+)$, we considered the direct formation by electron impacts of the upper level of N_2 (SPS) i.e. $N_{2,v}(C^3\Pi_u)$ noted $N_2(C)$ and also the upper level of N_2^+ (FNS) emission i.e. $N_{2,v}^+(B^2\Sigma_u^+)$ noted $N_2^+(B)$. The two assumed reactions of direct formation of $N_2(C)$ and $N_2^+(B)$ by electron impacts can be written as following with their respective rate constants $k_1(T_e)$ and $k_2(T_e)$:

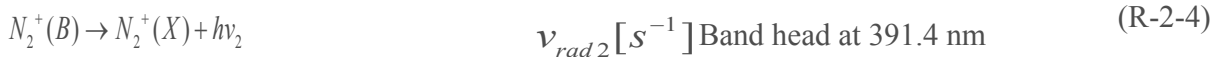
$$e + N_2 \rightarrow N_2(C) + e \quad k_1(T_e) = \left(\frac{2}{m}\right)^{1/2} \int \sigma_1 f(\varepsilon, T_e) \varepsilon^{1/2} d\varepsilon \quad [cm^3/s] \quad (R-2-1)$$

$$e + N_2^+ \rightarrow N_2^+(B) + e \quad k_2(T_e) = \left(\frac{2}{m}\right)^{1/2} \int \sigma_2 f(\varepsilon, T_e) \varepsilon^{1/2} d\varepsilon \quad [cm^3/s] \quad (R-2-2)$$

Where k_1 and k_2 denote the rate constants by electron-impacts depending on the electron kinetic temperature T_e , σ_1 and σ_2 the collision cross sections for reactions (R-2-1) and (R-2-2) respectively, ε the electron kinetic energy, m the electron mass and $f(\varepsilon, T_e)$ the electron energy distribution function (EEDF) at T_e .

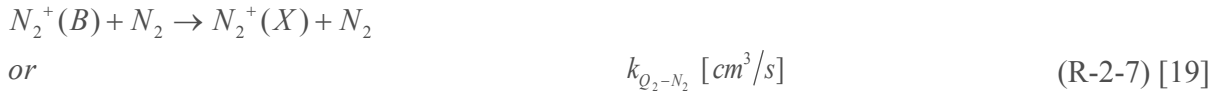
B. Radiative decays

$N_2(C)$ and $N_2^+(B)$ can be lost following spontaneous emissions of respectively second positive system and first negative system corresponding to the measured spectra (see Figure 2-6). These two reactions are given with their frequencies ν_{rad1} and ν_{rad2} :



C. Quenching

$N_2(C)$ and $N_2^+(B)$ species can be also lost by quenching collisions with molecular background nitrogen $N_2(X)$ and oxygen O_2 . These reactions are listed hereafter with their rate constants:



2.3.4.2 Relations between $N_2(C)$ and $N_2^+(B)$ densities and rates of creations and losses

At equilibrium, there is obviously a balance between rates of creations and losses of $N_2(C)$ and $N_2^+(B)$ states. When their respective densities are noted as $[N_2(C)]$ and $[N_2^+(B)]$, the balance equations take the following form:

In the case of $N_2(C)$ balance:

$$[e] \cdot [N_2] \cdot k_1(T_e) = \nu_{rad1} \cdot [N_2(C)] + k_{Q_1-N_2} \cdot [N_2(C)] \cdot [N_2] + k_{Q_1-O_2} \cdot [N_2(C)] \cdot [O_2] \quad (\text{Eq-2-1})$$

- In the case of $N_2^+(B)$ balance:

$$[e].[N_2].k_2(T_e) = \nu_{rad2} \cdot [N_2^+(B)] + k_{Q_2-N_2} \cdot [N_2^+(B)].[N_2] + k_{Q_1-O_2} \cdot [N_2^+(B)].[O_2] \quad (\text{Eq-2-2})$$

From balance equations (Eq-2-1) and (Eq-2-2), densities of $N_2(C)$ and $N_2^+(B)$ can be therefore calculated from:

$$[N_2(C)] = \frac{[e].[N_2].k_1(T_e)}{\nu_{rad1} + k_{Q_1-N_2} \cdot [N_2] + k_{Q_1-O_2} \cdot [O_2]} \quad (\text{Eq-2-3})$$

$$[N_2^+(B)] = \frac{[e].[N_2].k_2(T_e)}{\nu_{rad2} + k_{Q_2-N_2} \cdot [N_2] + k_{Q_2-O_2} \cdot [O_2]} \quad (\text{Eq-2-4})$$

2.3.4.3 Relations between $N_2(C)$ and $N_2^+(B)$ densities and spectra intensities

Furthermore, we can show that density ratio $[N_2(C)] / [N_2^+(B)]$ is proportional to ratio of intensity of $N_2(\text{SPS})$ and $N_2^+(\text{FNS})$ spectra $I_{SPS(394,4nm)} / I_{FNS(391,3nm)}$. But, as it is shown in Figure 2-7, the emitting state or the upper level corresponds to the specific quantum number $v=2$, i.e. $N_2(C^3\Pi_u)$, with its density noted $[N_2(C)]$. Therefore, the classical relation between each spectrum intensity and density of the upper energy state can be written as:

$$I_{SPS(394,4nm)} = C_1 \cdot [N_2(C)] \cdot \frac{hc}{\lambda_{SPS}} \cdot A_{SPS} \quad (\text{Eq-2-5})$$

$$I_{FNS(391,3nm)} = C_2 \cdot [N_2^+(B)] \cdot \frac{hc}{\lambda_{FNS}} \cdot A_{FNS} \quad (\text{Eq-2-6})$$

Where A denotes the radiative transition probabilities, hc/λ the transition energy at wavelength λ (394.3 nm for N_2 SPS or 391.4 nm for N_2^+ FNS) and C_1 and C_2 represent the constants depending on the spectrometer and the wavelength.

In the case of an optically thin medium and when specific conditions are fulfilled, we can assume that $C_1 \approx C_2$. Knowing that the fulfilled conditions are; firstly, the emission wavelengths

need to be quite close to be simultaneously collected in the same spectrum (only about 3 nm between 391.3 nm and 394.4 nm emissions). In fact for the validity of the approximation $C_1 \approx C_2$, the SPS and FNS spectra require to be measured simultaneously under the same spectroscopic parameters (i.e. same time exposure, same slit wide of spectrometer, same distance between the plasma source and the optical fiber of the spectrometer, and finally the same grating). Therefore we can have the following proportionality relation between spectra intensity and density of upper emissive states.

$$\frac{[N_2(C)]}{[N_2^+(B)]} \approx \frac{I_{SPS(394nm)}}{I_{FNS(391nm)}} \times Cst \quad (\text{Eq-2-7})$$

Where Cst is a constant including the transition probabilities (A_{SPS} and A_{FNS}) and the wavelength (λ_{SPS} and λ_{FNS}) i.e. $Cst \approx \frac{A_{FNS}}{A_{SPS}} \times \frac{\lambda_{SPS}}{\lambda_{FNS}}$ Then, by combining equation (Eq-2-7) with equations

(Eq-2-3) and (Eq-2-4), we can write the following:

$$\frac{k_1(T_e)}{v_{rad1} + k_{Q_1-N_2} \cdot [N_2] + k_{Q_1-O_2} \cdot [O_2]} = \frac{I_{SPS}}{I_{FNS}} \times Cst \times \frac{k_2(T_e)}{v_{rad2} + k_{Q_2-N_2} \cdot [N_2] + k_{Q_2-O_2} \cdot [O_2]} \quad (\text{Eq-2-8})$$

As intensity ratio I_{SPS}/I_{FNS} is experimentally known using OES measurements of our air microplasma (see for instance Figure 2-1), and since that the data of life time and quenching are known from literature (see Table 2-2), it remains *a priori* one unknown, namely, the electron temperature T_e . The problem is to find the best fit of T_e allowing the equality between left and right hand sides of equation (Eq-2-8).

Table 2-2 Data for lifetimes of $N_2(C)$ i.e. $N_2, v=2(C^3\Pi_u)$ and $N_2^+(B)$ i.e. $N_2^+, v=0(B^2\Sigma^+_u)$ and quenching rate constants taken from literature

Lifetime	ν_{rad1}	39×10^{-9}	s
	ν_{rad2}	62×10^{-9}	s
Quenching rates	$k_{O_1-N_2}$	0.46×10^{-10}	cm^3/s
$N_2(C)$	$k_{O_1-O_2}$	3.7×10^{-10}	cm^3/s
Quenching rates	$k_{O_2-N_2}$	2.1×10^{-10}	cm^3/s
$N_2^+(B)$	$k_{O_2-O_2}$	5.1×10^{-10}	cm^3/s

Data for electron reaction coefficients $k_1(T_e)$ and $k_2(T_e)$ are calculated versus T_e using multi-term development of EEDF to numerically solve Boltzmann equation [16]. The use of this rigorous method of Boltzmann equation solution is preferred to basic approximation of Maxwell distribution for EEDF or to the standard two-term solution no more available in molecular gases such as N_2 or O_2 or H_2O having high inelastic processes in comparison to elastic ones. In the case of air involving 50% of humidity, the collision cross sections of electron- N_2 , electron- O_2 and electron- H_2O are taken from [21]. Then, the set of electron- N_2 collision cross sections is completed by using data from [22] for collision cross section σ_1 of reaction (R-2-1) corresponding to $N_2(C)$ formation and for cross section σ_2 of reaction (R-2-2) corresponding to $N_2^+(B)$ formation.

Figure 2-8(a) and 2-8(b) display the best fit obtained for electron temperature T_e from equation (Eq-2-8) when using an experimental data of the intensity ratio I_{FNS}/I_{SPS} for two positions of inter-electrode space between the anodic tip and the cathode plate ($I_{FNS}/I_{SPS} \approx 3.1$ for $z=0$ mm on the tip and $I_{FNS}/I_{SPS} \approx 1.35$ for $z=2$ mm on the plate).

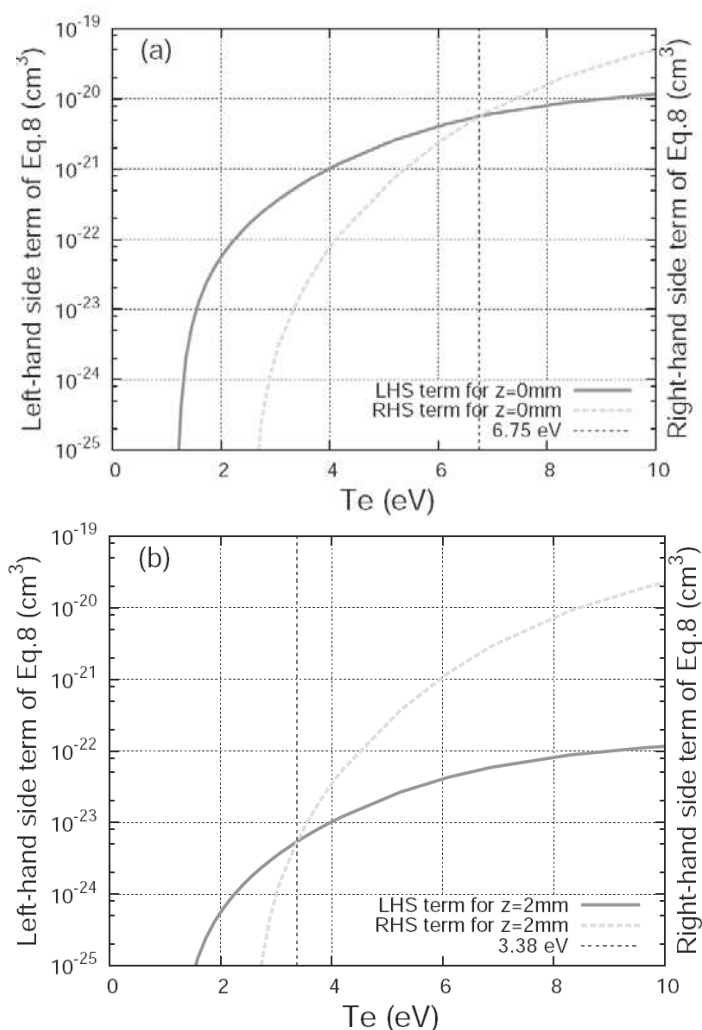


Figure 2-8 Left hand term (or SPS term) and right hand term (or FNS term) of (Eq-2-8) for (a) $z=0\text{mm}$ and (b) $z=2\text{mm}$. N.B.: the crossing between the two curves gives an electron temperature $T_e \approx 6.75$ eV for $z=0\text{mm}$ and $T_e \approx 3.38$ eV for $z=2\text{mm}$.

We used the highest value of the N_2 (FNS) at 391.4nm and N_2 (SPS) at 394.4nm for the estimation of the spectra intensities needed for the ratio I_{FNS}/I_{SPS} . Finally as shown in Figure 2-8, the electron temperature has been estimated from the crossing of the two curves corresponding respectively to left and right hand terms of equation (Eq-2-8). We obtained a mean temperature of around 6.75 eV equivalent to a reduced electric field E/N (where E is electric field and N is concentration of neutral particles) of about 290 Townsend (Td, $1\text{Td}=10^{-17} \text{Vcm}^2$), near the tip of

micro air plasma and $T_e \approx 3.38$ eV near the plate equivalent to E/N of about 120 Td. This equivalence between energy and electric field is confirmed in Figure 2-9 displaying the variation of electron temperature (or mean energy) obtained from solution of multi-term Boltzmann equation [16].

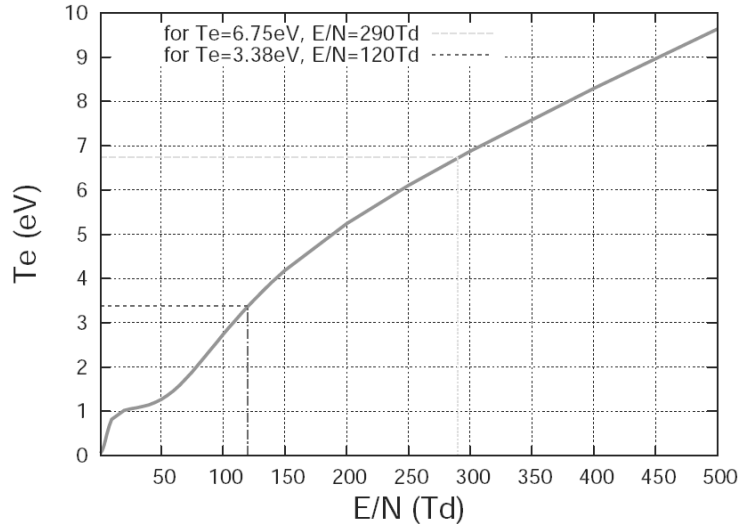


Figure 2-9 Electron mean kinetic temperature (or mean energy) calculated from solution of Multi-term Boltzmann equation in the case of humid air. This shows that $T_e = 6.75$ eV is equivalent to 290 Td and $T_e = 3.38$ eV to 120 Td.

The experimental electron temperature magnitudes using the present method based on spectra intensities are displayed in Figure 2-10 for several positions of the inter-electrode space. We can observe a decrease of T_e from the anodic tip ($z=0$ mm) downwards the cathode plate ($z=2$ mm). Such decrease of electron temperature versus the gap distance is qualitatively coherent with the usual electrical characteristics of air streamer corona discharges [11]. The error bars are also displayed in Figure 2-10. These errors come from; first, the uncertainty on measured spectra due mainly to the systematic spectrometer errors and on the choice of baseline. Secondly, these errors come from the uncertainty on the knowledge of basic data used in Eq-2-8, i.e. radiative life times, quenching rates and collision cross sections used to calculate electron rate coefficients $k_I(T_e)$ and

$k_2(T_e)$. As the spectra measurements are well reproducible, the second error source is the most important. The present error bars on basic data in humid air have been assumed not exceeding 30%.

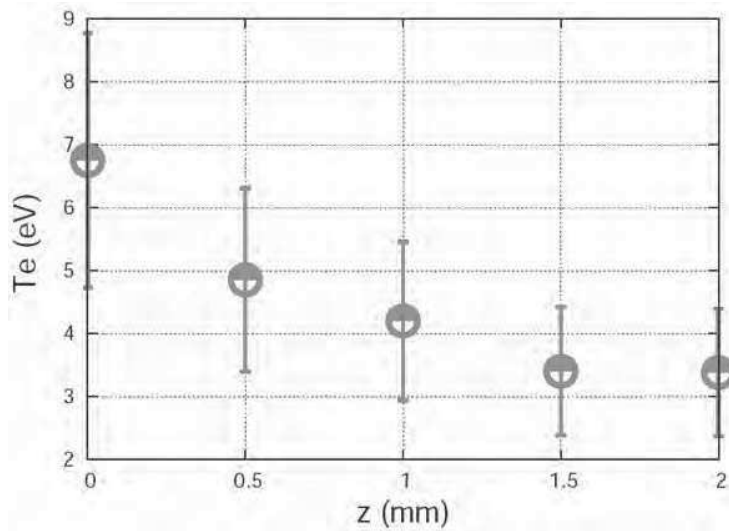


Figure 2-10 Variation of estimated electron temperature T_e from ratio of FNS and SPS spectra versus the gap distance from the anodic tip.

2.3.5 Determination of densities of plasma charged particles

2.3.5.1 Electron density η_e from H_α line

In addition to the electron temperature T_e , the electron density η_e is one of the fundamental plasma parameters. It plays an outstanding role in the study of the degree of thermodynamic equilibrium of the discharge: its value makes it possible to establish how far the plasma is from the local thermodynamic equilibrium conditions. In addition, most of the theoretical models that simulate discharge behaviour require accurate values of electron density to be validated since electron density is important to study the ionization degree of the considered plasma. Moreover, the knowledge of this parameter when the plasma is used in many applications such as chemical analysis, contaminant compound destruction, surface treatment, gene transfection, etc. allow us to

optimize the efficiency of the process [23]. As already emphasised and due to their non-disturbing character, the use of the spectroscopic methods based on the analysis of the light emitted by the plasma are of great interest in the determination of the electron density η_e . Analysis of the Stark broadening of Balmer lines from neutral atoms or ions emitted by the plasma is the most used method to estimate the electron density [24].

In many research studies, hydrogen lines are the first choice for plasma diagnostic applications because of the linear Stark effect and position in visible spectral region where high sensitivity and spectral resolution can be achieved with commercially available spectrometers. In the present study, the electron density η_e of the microplasma was calculated based on the emission of the H_α line at 656.28 nm. The H_α emission was observed with overlap of the band spectrum of N_2 first positive system. The spectral profile of pure H_α emission was determined by subtracting a straight baseline from the measured spectrum as shown Figure 2-11.

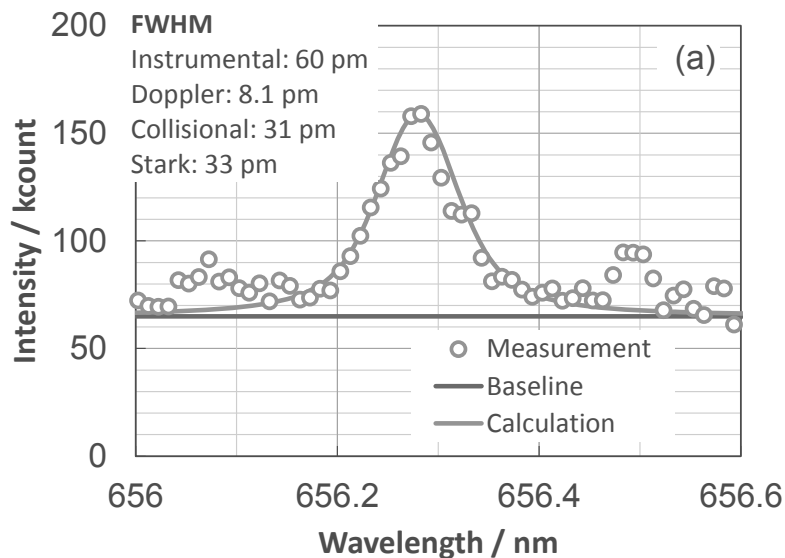


Figure 2-11 Measured emission spectrum at $z = 0$ and fitting of the H_α profile by straight baseline and Voigt profile resulted from the instrumental, Doppler, collisional and Stark broadenings.

Moreover, unlike in a computer simulation, in the experimental conditions it is often not possible to turn on or off different effects at demand; subsequently, the recorded line shapes can be the result or the superposition of several different emission. Typically, line shapes emitted by an atom or ion in a plasma is never infinitely narrow and suffer broadening and shifting either due to the interaction of the emitter with other particles in the plasma, what is usually called the pressure-broadening that includes Stark, van der Waals and resonance broadening, or to the movement of the emitters in the plasma, or even to the usually least important of all, the natural broadening [25]. It is also important to note that for the same plasma conditions the relative importance of those broadening mechanisms can be different for different lines. This is why in order to extrapolate accurate diagnostic information from the recorded line profiles, an evaluation of the importance of the different effects, or even correction, must be performed [25], such approach on processes is discussed in detail in several recent reviews [26][27][28].

Considering the case of atmospheric pressure microplasma discharge, the present measured $H\alpha$ spectrum was broadened by the combination of the following four mechanisms: the instrumental broadening, the Doppler broadening, the collisional broadening and the Stark broadening. Moreover, knowing that, the natural broadening arises due to the finite lifetime of the excited levels and is typically very small, it can be neglected in the case of the present air microplasma. Depending on the plasma conditions an estimation of the Stark component can be a non-trivial task. The choice of the deconvolution procedure as well as uncertainty of the final result depends on the ratio of the Stark component over all others. The deconvolution of the various contributions in the line broadened profile can be carried out based on the fact that, in many cases, the experimentally measured line profiles can be fitted with the Voigt function Eq-2-11 which is the convolution of the two functions: Gaussian and Lorentzian profiles. These profiles are respectively described by

Eq-2-9 and Eq-2-10 with the full width at half maximum FWHM $\Delta\nu_G$ for Gaussian profile and $\Delta\nu_L$ for Lorentzian profile and ν_0 the transition frequency in the center of the H_α line at 656.28 nm.

$$P_G(\nu) = \frac{A}{\Delta\nu_G} \sqrt{\frac{2 \cdot \ln(4)}{\pi}} \exp\left[-2 \cdot \ln(4) \left(\frac{\nu - \nu_0}{\Delta\lambda_G}\right)^2\right] \quad (\text{Eq-2-9})$$

$$P_L(\nu) = \frac{2 \cdot A}{\pi} \left[\frac{\Delta\nu_L}{4(\nu - \nu_0)^2 + \Delta\nu_L^2} \right] \quad (\text{Eq-2-10})$$

$$V(\nu, \Delta\nu_G, \Delta\nu_L) = \int_{-\infty}^{+\infty} G(\nu - x, \Delta\nu_G) \cdot L(x, \Delta\nu_L) \cdot dx \quad (\text{Eq-2-11})$$

Here we will give a short overview of the fundamental characteristics of each broadening mechanism with approximate formulae for evaluation of their profile parameter. Further information on the theory of broadening mechanisms can be found in literature books and articles as for instance [24][29][30] and [31].

A. Instrumental broadening

Any optical instrument has its own resolution and emission lines are necessarily affected by the instrument. Therefore, for an accurate analysis of emission spectroscopy, it is very important to include instrumental broadening of the spectrometer used in the experiment. Instrumental broadening has been measured from the reference single wavelength source such as a mercury lamp or He-Ne laser emission. In most experimental conditions, the apparatus function with instrumental broadening can be successfully expressed with the Gaussian profile with full width at half maximum FWHM as function of the wavelength ($\Delta\lambda_i$). In the case of our microplasma discharge, the measured instrumental function was fit well by the Gaussian profile Eq-2-9 as shown in Figure 2-12 and the FWHM of the instrumental broadening in terms of wavelength, was derived as $\Delta\lambda_i = 60.0$ pm when using He-Ne laser line.

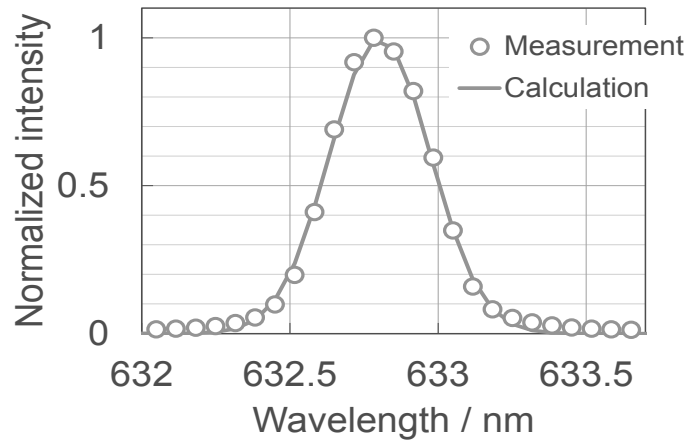


Figure 2-12 Measured emission spectrum of He-Ne laser and fitting by Gaussian profile.

B. Doppler broadening

For atomic spectra in the visible and UV, the limit on resolution is often set by Doppler broadening. With the thermal motion of the atoms (hydrogen atom H in this case), those atoms traveling toward the detector with a velocity v_r will have transition frequencies which differ from those of atoms at rest subjected to the Doppler shift. The distribution of velocities can be found from the Boltzmann distribution. Since the thermal velocities are non-relativistic, the Doppler shift in the angular frequency is given by the simple form:

$$\nu = \nu_0 \left(1 + \frac{v_r}{c} \right) \quad (\text{Eq-2-12})$$

Where v_r is the component of the velocity of the absorbing atom along the line of sight, ν_0 is the frequency of an atom at rest and c is the light speed. The amplitude of the frequency shift, is therefore, given by:

$$\Delta \nu = \nu_0 \frac{v_r}{c} \quad (\text{Eq-2-13})$$

From the Boltzmann distribution, the number of atoms with velocity v_r in the direction of the observed light is given by:

$$n(v_r) dv_r = N \sqrt{\frac{m_H}{2\pi k_B T_g}} \exp\left(-\frac{m_H v_r^2}{2k_B T_g}\right) dv_r \quad (\text{Eq-2-14})$$

Where N is the total number of atoms, m_H the hydrogen particle mass, k_B is the boltzman constant and T_g the gas temperature. Now use the fact that :

$$v_r = \frac{c(\nu - \nu_0)}{\nu_0}, dv_r = \frac{cd\nu}{\nu_0} \quad (\text{Eq-2-15})$$

So that, Eq-2-14 became:

$$n(\nu) d\nu = N \frac{c}{\nu_0} \sqrt{\frac{m_H}{2\pi k_B T_g}} \exp\left(-\frac{m_H c^2 (\nu - \nu_0)^2}{2\nu_0^2 k_B T_g}\right) d\nu \quad (\text{Eq-2-16})$$

The distribution function now refers to the number of particles capable of intercepting photons of frequency ν due to their velocity offset. The distribution of radiation around the center frequency is then given by

$$I(\nu) = I_0 \exp\left(-\frac{m_H c^2 (\nu - \nu_0)^2}{2\nu_0^2 k_B T_g}\right) \quad (\text{Eq-2-17})$$

The spectral profile of Doppler broadening is also in the form of a Gaussian and the FWHM (mm) is given by:

$$\Delta \nu_D = \frac{2\nu_0}{c} \sqrt{2 \ln 2 \frac{k_B T_g}{m_H}} \quad (\text{Eq-2-18})$$

Often it is convenient to express this in terms of wavelength:

$$\Delta \lambda_D = 2 \frac{\lambda_0}{c} \sqrt{2 \ln 2 \frac{k_B T_g}{m_H}} \quad (\text{Eq-2-19})$$

In low-temperature plasma, the gas temperature is $T_g = 300$ K. Thus, by substituting $T_g = 300$ K in Eq-2-19, according to the measurement with an alcohol thermometer described in sub-section 2.3.2.1, the Doppler width was derived as $\Delta \lambda_D = 8.14$ pm.

C. Collisional broadening

If the absorbing atom or ion responsible for an absorption line is suffering frequent collisions with other atoms or ions, the electron energy levels will be distorted. This is another mechanism leading to broadening of emission and absorption lines, called collisional broadening or pressure broadening. The line profile resulting from collisions is a Lorentzian profile (Eq-2-10), and the FWHM of this collisional broadening was estimated in terms of wavelength as:

$$\Delta \lambda_C = \frac{\lambda_0^2}{c} \Delta \nu_C = \frac{\lambda_0^2}{c} \frac{\nu_C}{\pi} \quad (\text{Eq-2-20})$$

Where ν_C is the collision frequency of the hydrogen atoms. This frequency can be estimated as:

$$\nu_C = \nu_{th} n_g \sigma_C = \frac{p}{k_B T_g} \sigma_C \sqrt{\frac{3k_B T_g}{m_H}} \quad (\text{Eq-2-21})$$

We denote v_{th} as the thermal velocity of the hydrogen atoms, p as the atmospheric pressure, n_g the gas density, and σ_c the collision cross section between hydrogen atoms and other molecules. A collision cross section $\sigma_c \approx 1 \times 10^{-18} \text{ m}^2$ was used for rough approximation [32]. Finally, the FWHM for the collisional broadening was estimated as $\Delta\lambda_c = 31 \text{ pm}$.

D. Stark broadening

Due to the distribution of the particles in the plasma, atoms at different points in the discharge experience different electric fields which may fluctuate in time, due to the relative movement between atoms and the charged particles surrounding them. This perturbation electric field changes the eigenvalues of the energies of the atoms, breaking partially the degeneracy of the atomic level, what is known as the Stark effect [33]. This field also affects the selection rules of the optical transitions between two states of each atom [34]. Considering the distribution of emitters and charged perturbers in the plasma, the collective consequence of those changes on the observed spectral lines results in a variation of the line shape, the width and the position depending on the plasma electron density and temperature [25].

On the one hand, and as already stated, the deconvolution of all broadening components from the experimentally measured H_α spectral profile in accordance with equations Eq-2-9, Eq-2-10 and Eq-2-11, enables an estimation of the FWHM of the Stark broadening $\Delta\lambda_s = 33 \text{ pm}$ at $z=0 \text{ mm}$. On another hand, and knowing that in plasma with a relatively high electron density (higher than at least 10^{13} cm^{-3} in the case of atmospheric pressure plasma) the Stark broadening can be directly related to electron density n_e as follow [35]:

$$n_e = 8.02 \times 10^{12} \text{ cm}^{-3} \left(\frac{\Delta\lambda_s}{\alpha_{1/2}} \right)^{3/2} \quad (\text{Eq-2-22})$$

The reduced wavelength $\alpha_{1/2}$ is tabulated as a function of electron density and temperature in [11]. This data set for $\eta_e \approx 10^{15} \text{ cm}^{-3}$ was extrapolated to 300 K, because the table contains only for the temperature higher than 5000 K, and $\alpha_{1/2} = 1.103 \text{ pm}$ was derived. Using this value and according to Eq-2-22, the electron density η_e as a function of the position z was estimated as shown in Figure 2-13

The estimated axial profile of the electron density shows a maximum near the water surface ($z = 1.5 \text{ mm}$). This could be possibly attributed either to a physical process (as i.e. secondary electron emission at the water surface) or to fitting uncertainties resulted from convolution of four broadenings whose FWHM are in the similar order of magnitude. There are also uncertainties due to the choice of the baseline used to estimate the experimental FWHM. Such errors are dependent of the resolution of $\text{H}\alpha$ spectra measurements.

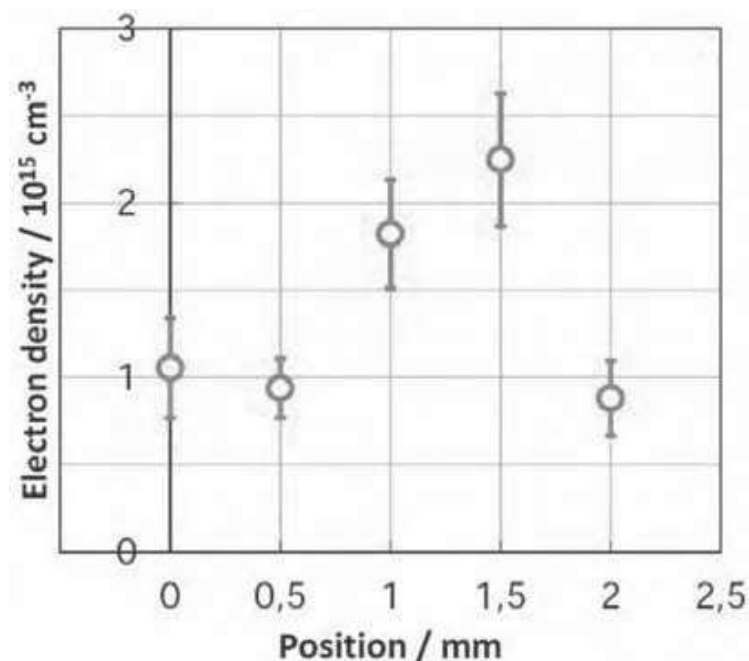


Figure 2-13 Derived electron density as a function of the position z . The open circles and the error bars show the average and the standard deviation respectively over four measurements at each z position.

In the case of present spectroscopy measurements, the total uncertainties including the estimations of the four physical broadenings and the good base line choice are of about 50%. In fact, the electron density behavior versus gap position has to be analyzed with many cautions because the present method based on Stark broadening of H_{α} emission spectrum is not well adapted for accurate determination of electron density lower than about 10^{14}cm^{-3} (see e.g. ref [36]). This method gives only an interesting estimation for the order of magnitude.

2.3.5.2 Estimation of Nitrogen ion density from N_2 (SPS) and N_2^+ (FNS) spectra

Second positive system $N_2(C^3\Pi_u - B^3\Pi_g, v=2, v'=5)$ and first negative system $N_2^+(B^2\Sigma^+_u - X^2\Sigma^+_g, v=0, v'=0)$ spectra can also be used to estimate ion density (see e.g. [37]). In the present work, the spectra intensities of head bands at 394.3 nm for N_2 (SPS: 2, 5) and 391.4nm for N_2^+ (FNS: 0, 0) (see Figure 2-6) are used to estimate density of N_2^+ ($X^2\Sigma^+_g$) ion on its ground state energy from the anodic tip to the cathode plate for the air microplasma used for gene transfection at Ehime University [1].

First of all the densities of upper emissive states $[N_2(C)]$ and $[N_2^+(B)]$ are expressed by Eq-2-22 and Eq-2-24, respectively, as a function of the density of their respective background states using the corresponding partition function and electronic excitation temperature T_{ex} of the air microplasma.

$$[N_2(C)] = \frac{[N_2(X)]}{Z_{N_2}} g_{N_2(C)} \exp\left(-\frac{\varepsilon_{N_2(C)}}{T_{ex}}\right) \quad (\text{Eq-2-23})$$

$$[N_2^+(B)] = \frac{[N_2^+(X)]}{Z_{N_2^+}} g_{N_2^+(B)} \exp\left(-\frac{\varepsilon_{N_2^+(B)}}{T_{ex}}\right) \quad (\text{Eq-2-24})$$

$[N_2(X)]$ and $[N_2^+(X)]$ are the densities of the ground energy states, Z_{N_2} and $Z_{N_2^+}$ their partition functions, $g_{N_2(C)}$ and $g_{N_2^+(B)}$ their statistic weights, and $\varepsilon_{N_2(C)}$, $\varepsilon_{N_2^+(B)}$ their energy of excited states. Moreover, by substituting (Eq-2-23) and (Eq-2-24) in (Eq-2-5) and (Eq-2-6), we can obtain the following relation under the same assumptions already given in sub-section 2.3.4.3 about the wavelength proximity of the two considered head bands at 391.4 nm and 394.3 nm :

$$\frac{I_{FNS(391nm)}}{I_{SPS(394nm)}} = \frac{[N_2^+(X)]}{[N_2(X)]} \frac{Z_{N_2}}{Z_{N_2^+}} \frac{g_{N_2^+(B)}}{g_{N_2(C)}} \frac{A_{FNS,v=0}}{A_{SPS,v=2}} \frac{\lambda_{SPS(2,5)}}{\lambda_{FNS(0,0)}} \exp\left(-\frac{\varepsilon_{N_2^+(B,v=0)} - \varepsilon_{N_2(C,v=2)}}{T_{ex}}\right) \quad (\text{Eq-2-25})$$

By considering the molecular data displayed in Figure 2-6 we can straightforwardly obtain a direct relationship between the ion density and the spectra intensity ratio I_{SPS}/I_{FNS} (Eq-2-26) measured near the tip of microplasma (cf. Figure 2-6), provided the excitation temperature T_{ex} is known:

$$[N_2^+(X)] = 9.463 [N_2(X)] \frac{I_{FNS(391nm)}}{I_{SPS(394nm)}} \exp\left(-\frac{8.2}{T_{ex}}\right) \quad (\text{Eq-2-26})$$

In fact, the unknown T_{ex} is generally assumed higher than vibration temperature T_{vib} of the plasma and lower than the electron temperature T_e . Indeed, in the case of the considered plasma, the electrons lose a fraction of their energy to initiate the excitation of the impacted molecules into a rotation or vibration or optical excitation states characterized by its own temperature (T_{rot} or T_{vib} or T_{ex}). In fact, these temperatures are relative to the internal energy of the associated excited state. While, the electron temperature T_e corresponds to the mean incident electron energy in the studied plasma. When the vibration and optical excitation states are mainly excited by electron impacts, therefore by definition T_e is always higher than the internal energy of the excited states since

electrons can also undergo ionization processes requiring electron energies higher than for excitation processes. This is why it is usually considered that T_{ex} is comprised between T_{vib} and T_e thus fulfilling the inequality: $T_{vib} < T_{ex} < T_e$. Furthermore, it is worth noting that T_{ex} is generally estimated using Boltzmann plots of the atomic line emissions as for instance in the case of an argon plasma when assuming a Boltzmann distribution of the different Ar I excited levels with energy E_i (see e.g. ref [38]). While T_e can be obtained from comparison of two close molecular spectra as shown in sub-section 2.3.4 and also underlined in the topical review of Zhu *et al* [15]. In the present microair plasma, T_{ex} has been estimated as following without using Boltzmann plot because we have not a succession of excited of atomic lines for various energy levels. We estimated the excitation temperature from a linear relation between T_{vib} and T_e having this form:

$$T_{ex} = (1 - weight) \times T_{vib} + weight \times T_e \quad \text{with } weight = 0.058 \quad (\text{Eq-2-27})$$

The constant coefficient *weight* between 0 and 1 (*weight*=0.058) has been chosen in order to have on the anodic tip ($z=0\text{mm}$) an ion density of about 10^{15} cm^{-3} usually obtained from air streamer simulation (see e.g. [39] or [40]) and coherent with an electrically neutral plasma, i.e. with the electron density $\eta_e \approx 10^{15} \text{ cm}^{-3}$ previously measured in sub-section 2.3.5.1.

Figure 2-14 displays, versus inter-electrode position for z varying between 0.5 mm to 2 mm, an estimation of nitrogen ion density $[N_2^+(X)]$ based on (Eq-2-26) by assuming that the excitation temperature T_{ex} is linearly weighted between vibration and electron temperatures as given by (Eq-2-27).

Error bars of about 50% are displayed in Figure 2-14. The error bars on the ion density estimation are simply a juxtaposition of the errors of the different terms used in Eq-2-26. The first incertitude comes from spectra measurements and can be considered as the lowest in comparison

to the other errors since there is a good reproducibility on the spectra measurements. The second error is linked to the estimation on T_{ex} and the third source of errors comes from the used molecular data used in Table 2-3 (partition function, statistic weight, etc.). In fact, the main error is normally due to T_{ex} estimation since a small decrease of T_{ex} magnitude (for instance 10%) leads to an important decrease of ion density (about 75%) due to the exponential dependence of ion density on T_{ex} . For all these reasons, the error bar for ion density estimation is important and can be considered in the best case close to 50%. The uncertainty of such approximation for ion density determination can therefore overpass 50% which means that such a method rather gives an order of magnitude.

Table 2-3 Molecular data used for the estimation of nitrogen ion density [$N_2^+(X)$]

Partition function	Z_{N_2}	1	<i>Approximately equal to the ground state multiplicity</i>
	$Z_{N_2^+}$	2	
Statistic weight	$g_{N_2(C)}$	6	<i>g = Spin multiplicity</i>
	$g_{N_2^+(B)}$	2	<i>* A-type doubling</i>
Radiative transitions probabilities	$A_{SPS,v=2}$	$(1/39) \times 10^9$	s^{-1}
	$A_{FNS,v=0}$	$(1/62) \times 10^9$	s^{-1}
Energy of exited states	$\mathcal{E}_{N_2(C,v=2)}$	11.3	<i>eV</i>
	$\mathcal{E}_{N_2^+(B,v=0)}$	3.1	<i>eV</i>

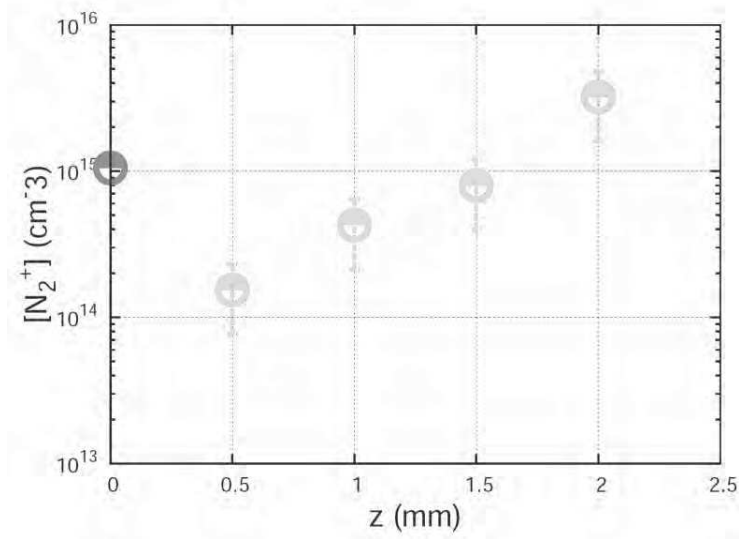


Figure 2-14 Nitrogen ion density $[N_2^+(X)]$ estimated from equation (Eq-2-26) versus inter-electrode position for z varying between 0.5mm to 2mm (green circles) when the ion density for $z=0$ mm (red circle) is estimated from streamer dynamics simulations.

2.4 Conclusion

During this second chapter, the air microplasma discharge, that already shows the best efficiency in the field of gene transfection in comparison to other plasma sources, has been experimentally characterized using optical emission spectroscopy (OES). The air microplasma is a corona discharge generated in ambient air from the tip of an anodic copper tube of 70 μm for outer diameter. The latter is powered by a pulsed AC high voltage with an amplitude of 7 kV, a frequency of 2 kHz and pulse duration of 0.1s. Moreover, a petri dish containing deionized water is placed on grounded electrode 2 mm under the anodic tip. The optical emission spectroscopy provided an estimation of the rotational T_{rot} , vibrational T_{vib} and the electron T_e , temperatures and also the densities of charged particles such as electrons and molecular nitrogen ions.

Indeed, this chapter was first devoted to the estimation of plasma rotational temperatures T_{rot} . It was determined from comparison of experimental and synthetic spectra in the case of UV

molecular emissions of OH(A-X), N₂⁺(FNS: 0, 0) at 391.4 nm and N₂(SPS: 0, 0) at 337 nm. The derived rotational temperatures determined near the anodic tip are equal to 2350K in the case of OH(A-X), 2000 K for N₂⁺(FNS: 0, 0) and 700 K for N₂(SPS: 0, 0). There is practically no T_{rot} variation along the inter-electrode space due to the dependence of T_{rot} on mainly the interactions between the heavy particles. These rotational temperatures higher than gas temperature clearly underlines significant thermal non-equilibrium between the different excited species that are generated inside the thin streamer filaments developed from the high voltage tip. However, as the density of these excited species are low (about 10⁵ lower than background gas density), the gas temperature measured using a standard thermometer remains close to ambient temperature i.e. 300 K. Furthermore, the spatial variation of the vibration temperature T_{vib} from around 3000 K near the tip electrode up to about 6500 K near the plate has been determined using N₂⁺(FNS: 0, 0) and N₂⁺(FNS: 1, 1) head bands spectra at 391.4 nm and 388.4 nm.

Then, the electron temperature T_e is estimated by using an interesting approach based on OES spectra previously emphasized in the literature. The present method uses two close molecular nitrogen emission bands N₂(SPS: 2, 5) and N₂⁺(FNS: 0, 0) with band heads at respectively 394 nm and 391.4 nm. We assumed that upper levels N₂(C³Π_u) and N₂⁺(B²Σ_u⁺) of these emission spectra are populated by direct electron impacts and lost either by radiative de-excitation or collisional quenching. We therefore obtained, at the balance between creations and losses, an interesting equation between the ratio of measured head band intensities of N₂(SPS: 2, 5) and N₂⁺(FNS: 0, 0) spectra and more particularly the electron rate coefficients of creations of N₂(C³Π_u) and N₂⁺(B²Σ_u⁺) that depend on electron temperature T_e . The solution of this balance equation leads to $T_e \approx 6.75$ eV near the anodic tip when the variation of electron rate coefficients versus T_e has been rigorously calculated using multi-term solution of Boltzmann equation in humid air. The

electron temperature decrease versus the inter-electrode distance from the tip to the cathode plate. This result is coherent with electron energy in the case of streamer corona discharges in the region close the high voltage tip. Noting that the error bar on electron temperature estimation is equal to about 50%.

In addition, in this chapter we determined the densities of plasma charged particles (electrons and ions). Firstly, the electron density η_e is estimated from the measured spectrum of H α line. The full width at half maximum (FWHM) of Stark broadening is extracted from experimental H α spectrum after a prior estimation of instrumental broadening using a standard He-Ne laser, Doppler broadening and collisional broadening using classical relations involving more particularly the known gas temperature. The use of a smooth extrapolation of literature data of reduced wavelength is performed to estimate η_e under our gas temperature condition. The obtained electron density $\eta_e \approx 1 \times 10^{15} \text{cm}^{-3}$, is coherent with the usual magnitude of electron density in the streamer head developed near the tip of corona discharge. The present estimations of the spatial variation of the electron density cannot be considered as accurate measurements but as a good order of magnitude of the electron density within an average error bar of about 50%.

Last, the density of molecular nitrogen ion in its background state $\text{N}_2^+(\text{X}^2\Sigma^+_g)$ is also estimated from the experimental ratio of the intensities of the two close previous molecular nitrogen emission bands $\text{N}_2(\text{SPS}: 2, 5)$ at 394.4 nm and $\text{N}_2^+(\text{FNS}: 0, 0)$ at 391.3 nm. This ratio intensity has been correlated to the density of background states ion $\text{N}_2^+(\text{X}^2\Sigma^+_g)$ and neutral molecule $\text{N}_2(\text{X}^3\Sigma^+_g)$ assuming a prior knowledge of the excitation temperature T_{ex} . In this case, when assuming a prior estimation or calibration of the ion density of about 10^{15}cm^{-3} at $z=0\text{mm}$ based on literature streamer dynamics simulations, the spatial variation of the ion density along z axis has been determined in the whole electrode gap distance within an error bar of about 50%.

As already emphasis, these plasma characteristics are required as input data for a specific Monte Carlo method developed for cell membrane poration and permeabilization. This developed model is described in the following chapter 3. The aim of this model is; from various parametric studies, the better understanding of the gene transfection mechanisms during the interactions of the present microplasma with cell membranes.

Finally, these optical emission spectroscopy characterizations of the air microplasma used for simulation of cell membrane poration was recently published in *Plasma Physics and Controlled Fusion* [42] and will be presented in international conference [43].

2.5 References

- [1] M. Jinno, Y. Ikeda, H. Motomura, Y. Kido, K. Tachibana, and S. Satoh, “The Necessity of Radicals for Gene Transfection by Discharge Plasma Irradiation,” *J. Photopolym. Sci. Technol.*, vol. 27, pp. 399–404, 2014.
- [2] C. O. Laux, T. G. Spence, C. H. Kruger, and R. N. Zare, “Optical diagnostics of atmospheric pressure air plasmas,” *Plasma Sources Sci. Technol.*, vol. 12, pp. 125–138, 2003.
- [3] E. Condon, “Theory of intensity distribution in band systems,” *Phys. Rev.*, vol. 28, pp. 1182-1201, 1926.
- [4] F. R. Gilmore, R. Laher, and P. J. Espy, “Franck-Condon Factors, r-Centroids, Electronic Transition Moments, and Einstein Coefficients for Many Nitrogen and Oxygen Band Systems,” *J. Phys. Chem. Ref. Data*, vol. 21, pp. 1005–1107, 1992.
- [5] Z. Machala, L. Les, M. Morvova, and V. Martis, “Emission spectroscopy of atmospheric pressure plasmas for bio-medical and environmental applications,” *J. Mol. Spectrosc.*, vol. 243, pp. 194–201, 2007.
- [6] C. O. Laux, “Radiation and nonequilibrium collisional-radiative models,” in *Physico-Chemical Modeling of High Enthalpy and Plasma Flows*, Rhode-Saint-Genese Belgium,

- 2002.
- [7] L. Luque, "LIFBASE: Database and spectral simulation (version 1.6)," 1999.
- [8] P. Bruggeman, J. Liu, J. Degroote, M. G. Kong, J. Vierendeels, and C. Leys, "Dc excited glow discharges in atmospheric pressure air in pin-to-water electrode systems," *J. Phys. D. Appl. Phys.*, vol. 41, p. 215201, 2008.
- [9] P. Bruggeman, D. Schram, M. Á. González, R. Rego, M. G. Kong, and C. Leys, "Characterization of a direct dc-excited discharge in water by optical emission spectroscopy," *Plasma Sources Sci. Technol.*, vol. 18, p. 25017, 2009.
- [10] P. Bruggeman, D. C. Schram, M. G. Kong, and C. Leys, "Is the Rotational Temperature of OH(A-X) for Discharges in and in Contact with Liquids a Good Diagnostic for Determining the Gas Temperature?," *Plasma Process. Polym.*, vol. 6, pp. 751–762, 2009.
- [11] O. Eichwald, O. Ducasse, D. Dubois, A. Abahazem, N. Merbahi, M. Benhenni, and M. Yousfi, "Experimental analysis and modeling of positive streamer in air: towards an estimation of O and N radical production," *J. Phys. D. Appl. Phys.*, vol. 41, p. 234002, 2008.
- [12] A. Komuro, R. Ono, and T. Oda, "Kinetic model of vibrational relaxation in a humid-air pulsed corona discharge," *Plasma Sources Sci. Technol.*, vol. 19, p. 55004, 2010.
- [13] R. Shrestha, R. B. Tyata, and D. P. Subedi, "Estimation of Electron Temperature in Atmospheric Pressure Dielectric Barrier Discharge Using Line," *J. Sci. Eng. Technol.*, vol. 8, pp. 37–42, 2012.
- [14] K. Kano, M. Suzuki, and H. Akatsuka, "Spectroscopic measurement of electron temperature and density in argon plasmas based on collisional-radiative model," *Plasma Sources Sci. Technol.*, vol. 9, pp. 314–322, 2000.
- [15] X. M. Zhu and Y.-K. Pu, "Optical emission spectroscopy in low- temperature plasmas containing argon and nitrogen : Determination of the electron temperature and density by the line-ratio method," *J. Phys. D. Appl. Phys.*, vol. 43, 2010.
- [16] M. Yousfi and M. D. Benabdessadok, "Boltzmann equation analysis of electron-molecule collision cross sections in water vapor and ammonia," *J. Appl. Phys.*, vol. 80, pp. 6619, 1996.

- [17] M. Yousfi, A. Bekstein, N. Merbahi, O. Eichwald, O. Ducasse, and M. Benhenni, "Basic data for atmospheric pressure non-thermal plasma investigations in environmental and biomedical," *Plasma Sources Sci. Technol.*, vol. 19, pp. 034004.1–034004.8, 2010.
- [18] M. S. Bak, W. Kim, and M. A. Cappelli, "Quenching of Excited Electronic States of Molecular Nitrogen in Nanosecond Pulsed Discharges in Atmospheric Pressure Air," in *49th AIAA Aerospace Sciences Meeting including the New Horizons Forum and Aerospace Exposition*, pp. 1–7, 2011.
- [19] R. C. Flagan and J. P. Appleton, "Excitation Mechanisms of the Nitrogen First-Positive and First-Negative Radiation at High Temperature," *J. Chem. Phys.*, vol. 56, pp. 1163–1173, 1972.
- [20] J. L. Fox and A. Dalgarno, "The Vibrational Distribution of N_2^+ in the Terrestrial Ionosphere," *J. Geophys. Res.*, vol. 90, pp. 7557–7567, 1985.
- [21] G. Ruíz-Vargas, M. Yousfi, and J. de Urquijo, "Electron transport coefficients in the mixture of H_2O with N_2 , O_2 , CO_2 and Dry Air for the Optimization of Non-Thermal Atmospheric Pressure Plasmas," *J. Phys. D. Appl. Phys.*, vol. 43, pp. 455201.1–455201.6, 2010.
- [22] Y. Itikawa, "Cross sections for electron collisions with nitrogen molecules," *J. Phys. Chem. Ref. Data*, vol. 35, pp. 31–53, 2006.
- [23] C. Yubero, M. C. García, and M. D. Calzada, "On the use of the $H\alpha$ spectral line to determine the electron density in a microwave (2.45GHz) plasma torch at atmospheric pressure," *Spectrochim. Acta Part B At. Spectrosc.*, vol. 61, pp. 540–544, 2006.
- [24] H. R. Griem, "Spectral line broadening by plasmas," New York ; London : Academic Press, 1974.
- [25] A. Y. Nikiforov, C. Leys, M. A. Gonzalez, and J. L. Walsh, "Electron density measurement in atmospheric pressure plasma jets: Stark broadening of hydrogenated and non-hydrogenated lines," *Plasma Sources Sci. Technol.*, vol. 24, p. 034001, 2015.
- [26] N. Konjević, M. Ivković, and N. Sakan, "Hydrogen Balmer lines for low electron number density plasma diagnostics," *Spectrochim. Acta - Part B At. Spectrosc.*, vol. 76, pp. 16–26,

- 2012.
- [27] N. Konjević, “Plasma broadening and shifting of non-hydrogenic spectral lines: present status and applications,” *Phys. Rep.*, vol. 316, pp. 339–401, 1999.
- [28] N. Konjević, M. Ivković, and S. Jovićević, “Spectroscopic diagnostics of laser-induced plasmas,” *Spectrochim. Acta - Part B At. Spectrosc.*, vol. 65, pp. 593–602, 2010.
- [29] H. R. Griem, “Plasma Spectroscopy,” *New York: McGraw-Hill*, 1964.
- [30] R. G. Breene, “The Shift and Shape of Spectral Lines,” *New York: Pergamon Press*, 1961.
- [31] G. W. F. Drake, “Springer Handbook of Atomic, Molecular, and Optical Physics,” *Springer-Verlag, New York*, 2006.
- [32] M. A. Lieberman and A. J. Lichtenberg, “Principles of Plasma Discharges and Materials Processing,” *New York: John Wiley & Sons, Inc.*, 1994.
- [33] L. D. Landau and M. E. Lifshits, “Quantum Mechanics Non-relativistic Theory,” Transl. from the Russian by J. B. Sykes and J. S. Bell 2nd edn., *Oxford: Pergamon Press*, 1959.
- [34] H. A. Bethe and E. E. Salpeter, “Quantum Mechanics Of One And Two Electron Atoms,” *New York: Plenum*, vol. 168, 1977.
- [35] J. Ashkenazy, R. Kipper, and M. Caner, “Spectroscopic measurements of electron density of capillary plasma based on Stark broadening of hydrogen lines,” *Phys. Rev. A*, vol. 43, pp. 5568–5574, 1991.
- [36] J. M. Palomares, S. Hübner, E. A. D. Carbone, N. de Vries, E. M. van Veldhuizen, A. Sola, A. Gamero, and J. J. A. M. van der Mullen, “H β Stark broadening in cold plasmas with low electron densities calibrated with Thomson scattering,” *Spectrochim. Acta Part B At. Spectrosc.*, vol. 73, pp. 39–47, 2012.
- [37] D. Staack, B. Farouk, A. Gutsol, and A. Fridman, “Spectroscopic studies and rotational and vibrational temperature measurements of atmospheric pressure normal glow plasma discharges in air,” *Plasma Sources Sci. Technol.*, vol. 15, pp. 818–827, 2006.
- [38] G. Wattieaux, M. Yousfi, and N. Merbahi, “Optical emission spectroscopy for quantification of ultraviolet radiations and biocide active species in microwave argon

- plasma jet at atmospheric pressure,” *Spectrochim. Acta - Part B At. Spectrosc.*, vol. 89, pp. 66–76, 2013.
- [39] N. Y. Babaeva and G. V Naidis, “Two-dimensional modeling of positive streamer dynamics in non-uniform electric fields in air,” *J. Phys. D. Appl. Phys.*, vol. 29, pp. 2423, 1996.
- [40] C. Li, J. Teunissen, M. Nool, W. Hundsdorfer, and U. Ebert, “A comparison of 3D particle, fluid and hybrid simulations for negative streamers,” *Plasma Sources Sci. Technol.*, vol. 21, pp. 55019, 2012.
- [41] P. Paris, M Aints, F Valk, T Plank, A Haljaste, K.V. Kozlov and H-E. Wagner, “Intensity ratio of spectral bands of nitrogen as a measure of electric field strength in plasmas’,” *J. Phys. D. Appl. Phys.*, vol. 38, pp. 3894–3899, 2005.
- [42] A. Zerrouki, H. Motomura, Y. Ikeda, M. Jinno, and M. Yousfi, “Optical emission spectroscopy characterizations of micro-air plasma used for simulation of cell membrane poration,” *Plasma Phys. Control. Fusion*, vol 58, pp. 075006.1–075006.12, 2016.
- [43] A. Zerrouki, H. Motomura, Y. Ikeda, M. Jinno, and M. Yousfi, “OES spectroscopic measurements of temperatures and densities of charged particles in micro-air plasma for gene transfection,” in 6th Internatinal Conference on plasma Medicine (ICPM6), 2016.

CHAPTER 3

DESCRIPTION OF MONTE CARLO MODEL OF MEMBRANES PORATION BY PLASMA SPECIES FLUXES

3.1 Introduction

As specified in the first chapter, the aim of the present thesis is to study the mechanisms of plasma-induced membrane permeabilization. This is achieved by simulating numerically the membrane permeabilization and pore formation when the cells are impacted by the micro air plasma fluxes. Thus, the goal of this chapter, is to describe the developed Monte Carlo model of membrane poration by interactions with plasma species fluxes.

The first part of this chapter is devoted to a review on the progress made so far on the numerical modeling of cold plasma interactions with cells and tissues. However, we will interest firstly on the different literature researches on the molecular dynamics on electroporation for gene transfection. Indeed, it have been shown that this method is suitable for investigating electroporation phenomena. In addition, this atomic level investigations are an important contribution towards a better understanding of the basic phenomena and processes occurring on a lipid film when being exposed to the bombardment of plasma species. It is known that most bio-

organisms, including bacteria, are coated by lipid film surrounding them. This means that many interactions occur between plasma species and the lipid layer before the plasma species reach the inner parts of the bio-organisms. Thus, a part of this overview is dedicated to the different literature works on the reactive molecular dynamics simulations to study the interactions mechanisms of some active plasma chemical species such as O, OH, O₃ and HO₂ radicals, with different types of biomolecules as for instance lipids or DNA, or water, or peptidoglycan.

In the second part of this chapter, we are mainly interested by the description of the developed Monte Carlo method for the simulation of pore formation. The latter has been inspired from literature researches performed in low pressure plasmas and used for deep silicon etching for application to power electronic devices. It's aimed to statistically simulate, at a global (or macro) scale, the pore formation during atmospheric pressure plasma interactions with cell membrane. The plasma species interacting with membrane come from a low-temperature microplasma generated in air at atmospheric pressure and used for gene transfection. This new Monte Carlo technique is applied for the first time to the case of interactions between plasma species and multilayer membrane of a biological cell. In the framework of this simulation model, the plasma species are considered as a succession of super-particles. Each super-particle corresponds to a great number of elementary species impacting the membrane. The three kinds of considered plasma active species are electrons, ions and neutral radicals with fluxes estimated from a plasma reaction kinetic model and optical emission spectroscopy OES. The membrane is discretized following a great number of super-sites. In each super-site can take place different kinds of macro-process such as the activation or the opening of the membrane super-site and the recombination or the reflection of the plasma super-particle when colliding the considered super-site. Furthermore, the displacement of the active plasma species through the membrane are governed by classical laws

using stochastic formalisms while the interactions processes are defined by their probabilities of impacts determined from random numbers.

3.2 Overview on the numerical modeling of cold plasma interaction with cells membrane and tissues

This subsection is aimed to provide an overview of the various simulations that have been carried out in the context of plasma–biomolecule interactions. A reasonable number of studies have been devoted to molecular processes in electroporation, and a few studies also addressed reactive interactions of plasma species with biomolecules.

3.2.1 Molecular dynamic studies on electroporation of cell membranes for gene transfection

Electroporation or electropermeabilization of cell membranes is a topic of considerable interest. Indeed, the natural formation of transient aqueous-filled pores in biological membranes is crucial to many important processes on the cellular level, such as for instance ensuring ion transport across the membrane and maintaining osmotic balance by assisting pumps and ion channels [1] [2]. Alternatively, as mentioned in the first chapter, electroporation can also be induced artificially by high-intensity electric field pulses, permitting bio-medical applications, including for instance drug, antibody and plasmid delivery into cells (gene transfection)[3].

A significant number of MD molecular dynamics studies have been performed to study electroporation of cell membranes at the molecular level (see e.g. [4] or [5]). Their goals are to quantitatively model and understand some effects of the high electric field on biological membranes at the nanosecond time scale. These research studies were more particularly aimed to better clarifying the pore formation process, and possible ionic transports either via nano-pores or through the bio-membrane structure.

Hu *et al* [4] employed coarse-grained simulations based on the Groningen molecular simulation (Gromos) force field software [6] to study electroporation in a lipid membrane composed of dipalmitoylphosphatidylcholine (DPPC) lipid molecules surrounded by water molecules. He carried out two types of simulations: the first one using a variable field strength with an average value of 0.01Vnm^{-1} during 10 ns, and the second one by using a fixed field simulation with a field strength of 0.5Vnm^{-1} . The used system is the same as in the simulations by Tieleman *et al* [5], except that Tieleman *et al* employed a united-atom description. The last is based on a particle that incorporates a group of atoms and can approximately represent the molecular mechanical properties of the group on a scale of size that is larger than atomic scale, called pseudo-atom.

In addition, Tieleman *et al* [5] employed the Optimized Potentials for Liquid Simulations force field (OPLS) to study the formation of water-filled pores under mechanical and electrical stress. The membranes studied consisted of DPPC and Dioleoylphosphatidylcholine (DOPC) lipid molecules which are similar to most other MD simulations of electroporation of membranes [1].

Figure 3-1 and Figure 3-2 show respectively one of the obtained results by Hu *et al* [4] and Tieleman *et al* [5] when using a fixed field of 0.5Vnm^{-1} . These results are in good agreement. Indeed pore formation is observed to occur after a few nanoseconds, mostly on the anodic side of the electrically stressed membrane. Moreover, defects start to appear at the anodic side of the membrane, due to the interaction of the dipole moments of the polar heads with the electric field, disturbing the alignment of the lipid tails. After the initial breakthrough, the poration process occurs quickly on the nanosecond time scale.

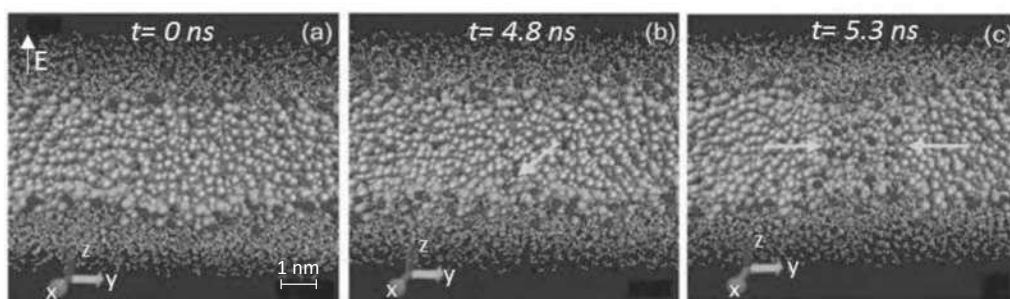


Figure 3-1 Simulated pore formation by applying an electric field in a classical MD simulation with non-reactive force field. The electric field (in this example 0.5 Vnm^{-1}) is perpendicular to the membrane, as indicated by the white arrow in (a); (a) Initial configuration at $t=0 \text{ ns}$ (b) structural rearrangement begins at the membrane bottom (anode side) at about $t=4.8 \text{ ns}$; (c) a pore predicted to form at $t=5.3 \text{ ns}$. The turquoise, green, purple and gold spheres denote methylene, glycerol, choline and phosphate groups, respectively, while the small red and white spheres represent oxygen and hydrogen. It is clear from (c) that a pore is formed in the membrane, lined with the polar heads of the lipids [4][1].

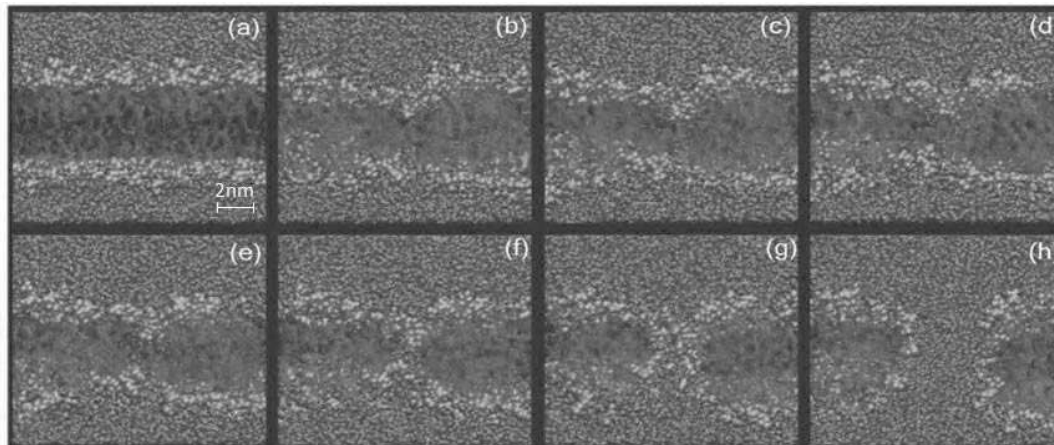


Figure 3-2 Pore formation in the DOPC simulation with an applied electric field of 0.5 Vnm^{-1} : (a) structure at $\sim 2.40 \text{ ns}$, no obvious defects; (b) $\sim 3.04 \text{ ns}$, water penetration from both sides and significant deformation of the bilayer; (c-e) ~ 3.08 to $\sim 3.15 \text{ ns}$, two defects from opposite sides of the bilayer form a single file across the bilayer; (f) $\sim 3.25 \text{ ns}$ and (g) $\sim 3.35 \text{ ns}$, further rearrangement of the phospholipids and increasing size of the water column; (h) $\sim 3.55 \text{ ns}$, final size of the defect and nearly complete rearrangement of the phospholipids [5].

Furthermore, in a recent study, Hu *et al* [7] revealed that the electroporation is really a two-stage process. Indeed, it was shown that the electric field causes a Maxwell stress at the membrane, leading to lipid dipole rearrangement and pore opening. More precisely, the initial step in the pore formation is the formation of a ‘single file defect’, where a chain of water molecules span the membrane. It is observed that water penetration increases significantly even before the actual pore formation. It is suggested that the electric field stabilizes water defects, because of the favorable interaction of small water clusters with the electric field. Bockmann *et al* [8] used the Gromos force field to study palmitoyl-oleoyl-phosphatidylcholine POPC-based bilayers, applying an electric field of 0.04–0.7 Vnm⁻¹. Based on these simulations, a detailed four-state pore formation model was formulated (see Figure 3-3), and good agreement between simulations and experiment was reached.

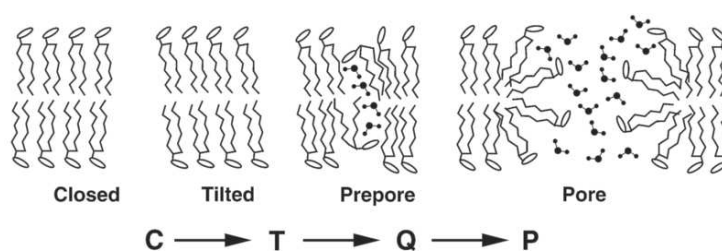


Figure 3-3 Kinetic model of pore formation. In a first step, resulting in intermediate T, the polar lipid head-groups become tilted. Tilting occurs in opposite directions for the two leaflets. In a second step, Q, one or two lipid head-groups and a few water molecules intrude into the bilayer and form a polar chain. Pore formation, P, is the last step [8].

While the above mentioned simulations are very useful for understanding the basic mechanisms of pore formation under the influence of electrical stress in basic membranes, real membranes are more complex, as they also contain a number of other components. This is in part addressed in the simulations by Tarek *et al* [9] and Vernier *et al* [10].

Tarek *et al* [9] employed the molecular mechanics program (CHARMM) force field to study electroporation in different lipids bilayers, for instance, a standard bare bilayer composed of equilibrated fully hydrated dimyristoyl-phosphatidylcholine (DMPC) lipids, a bilayer containing a peptide nanotube channel, and a bilayer with a peripheral DNA double strand. Electroporation was studied by applying electric fields of 0.5 and 1.0 Vnm⁻¹. These MD simulations demonstrate that while the applied field effectively creates electroporation, the internal structure of both the peptide tube and the DNA fragment are hardly affected. Resealing and reconstitution of the membrane is observed when switching off the field. Figure 3-4 displays the obtained results. We notice a formation of ‘fingers’ of water that penetrate the hydrophobic core of the bilayer, from either side, and irrespective of the direction of the applied electric field. These fingers expand and form water wires, and the hydrophilic heads start to line the pore. Concurrently, a fast reorientation of the solvent molecules and a slow reorientation of the lipid head group dipoles is observed. These results are similar to the those obtained by Tieleman *et al* [5] and Hu *et al* [4].

Vernier and co-workers employed a combination of MD simulations and experiments on live cells to study electroporation [10]. In this case, the computational bilayers are composed by fully hydrated 1-palmitoyl-2-linoleoyl-sn- glycerol-3-phosphatidylcholine (PLPC) and oxidized PLPC. Forces are derived from the OPLS force field. The goal of this study was to determine if bilayers containing oxidized lipids electroporate more easily. Indeed, the electropores were invariably formed in immediate association with one or more oxidized lipids. The electric field range was chosen to be 0.3–0.5Vnm⁻¹, and the lowest value to observe electroporation was 0.360 Vnm⁻¹, which is lower than the threshold value determined by Tieleman *et al* [5]. This indicates that the electric field threshold needed for electroporation may depend on the precise structure and composition of the membrane. Finally, while summarizing, these simulations provide support for

stochastic pore formation theories in which the stress imposed on the membrane is released by the formation of the nanometre sized hydrophilic pores [1]. Moreover, these pores could be formed after a few nanoseconds [4] with diameters ranging from a few to 10 nm could be witnessed [5][11].

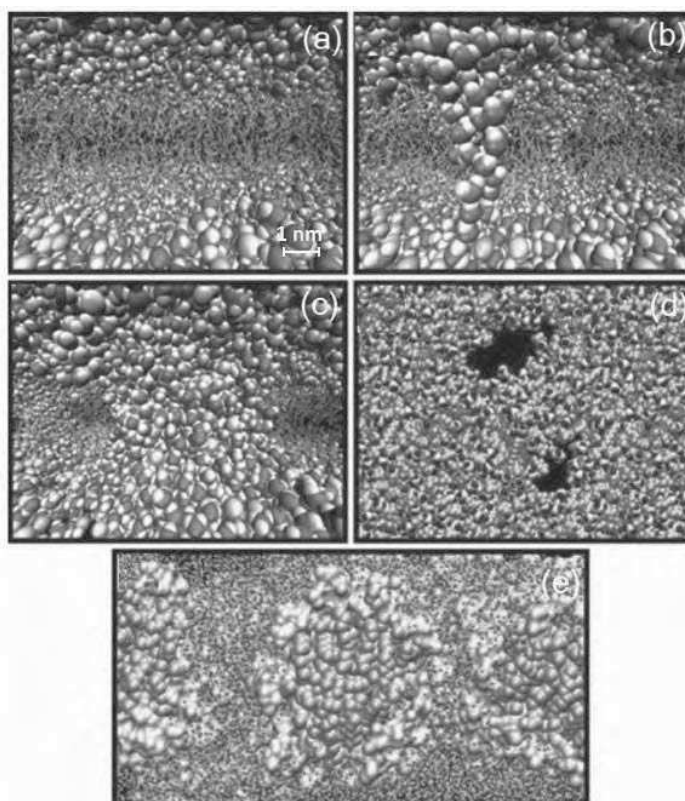


Figure 3-4 Configurations from the MD simulations for the large DMPC bilayer drawn in perspective. (a) Bilayer at equilibrium. (b) Formation of water wires at the initial stage of the electroporation process when the bilayer is subject to a transverse electric field. (c) Formation at a later stage of large water pores stabilized by lipid head groups. Topology of the water pores (d) top view (e) side view. In the first three panels, water molecules (O red; H white), lipid phosphate (yellow), and nitrogen (green) atoms are represented by van der Waals radii, and the acyl chains (cyan) by stick representation. In the last panel, the hydrophilic lipid head group (yellow) and the hydrophobic acyl chains (cyan) are represented by van der Waals spheres to underline the topology and nature of the water pores. Due to the use of perspective views, atoms in the front appear bigger than those in the back [9].

However, despite these numerous literature researches based on molecular dynamics MD performed to study electroporation of cell membranes at the molecular level, there are no similar scientific papers based on MD simulation to study the membrane poration during interactions with low-temperature plasma species. The existing literature researches are based on the reactive MD simulations of the interactions between plasma species and biomolecules without targeting applications to membrane poration. In fact, these papers are devoted to some active plasma chemical species such as O, OH, O₃, H₂O₂ which interact with different types of biomolecules as for instance lipids [12], or peptidoglycan [13] or DNA [14], or water [15].

3.2.2 Reactive MD simulations of the interactions between plasma species and biomolecules

In order to study the chemistry of the interaction of reactive species at the molecular level with biomolecular structures, the simulation needs to be able to form and break chemical bonds, thus requiring reactive force fields. In the following we will focus on the MD simulations using reactive force fields, studying chemical processes when plasma species interact with different types of biomolecules.

3.2.2.1 Reactive MD simulations for reactive species interacting with lipids

Babaeva *et al* [12] employed reactive MD simulations to study the interactions of energetic ions with a very simple model for a lipid film. Indeed, it was displayed that ions with energies in excess of 60 eV may reach the surface. The MD simulations are based on a combination of the reactive Brenner potential or so-called ‘Reactive Empirical Bond Order’ (REBO) potential [16] for C–H interactions and a purely repulsive Moliere potential for Ar-interactions. The lipid film is modelled as an array of vertically aligned acyl chains. Reactive MD studies on the interactions of reactive oxygen species ROS with lipids were carried out by van der Paal *et al* [17]. Using the Reax force

field, simulations were performed to investigate the interaction of O and OH radicals with α -linolenic acid, which is a fatty acid typical for the topmost layer of the human skin, the stratum corneum. These simulations demonstrate that the radicals abstract hydrogen atoms, which leads to the increase of the hydrophilic character of the lipids and thereby alters the homeostatic function of the skin.

More recently, Yusupov *et al* [18] studied the interactions of reactive oxygen and nitrogen species RONS with a phospholipid bilayer (PLB), which is the simple model system for the cell membrane (see Figure 3-5). They investigated these interactions by means of atomic scale reactive using density functional based tight binding (DFTB) method [19] and non-reactive molecular dynamics simulations. The latter is based on coarse-grained model applying the Martini force field developed by the research group of Marrink and Tieleman [20]. The obtained results showed that ROS, namely OH radicals can break an important bonds in the hydrophilic head group as well as in the lipid tails, modifying/oxidizing the structure. Moreover, the investigation of the long-time behavior of the modified PLB structure (due to oxidative and nitrosative stress), applying a long timescale simulation technique, i.e., a coarse-grained model, allows the exploration of processes such as the membrane permeability and fluidity, as well as the pore formation. Indeed, it shows that upon increasing the degree of oxidation of the lipid bilayers, pores can be formed when a certain threshold is exceeded.

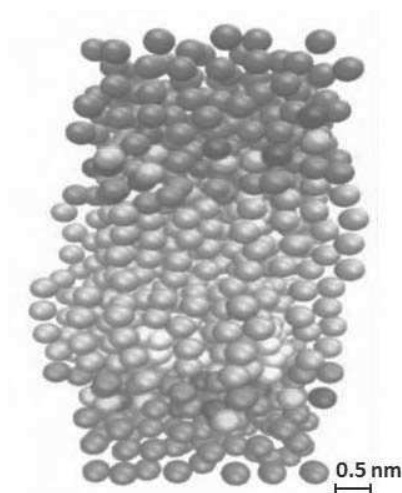


Figure 3-5 Schematic representation of the PLB used in the coarse-grained model. It is surrounded by water, with cholesterol imbedded in it. The grey beads represent water molecules, the yellow beads represent cholesterol. The PLB consists of a NC3 head group (dark blue beads), a phosphate group (green beads), a diacylglycerol linker (red beads) and two lipid tails (light blue beads)[18].

3.2.2.2 Reactive MD simulations for reactive species interacting with peptidoglycan

In the aim to better understand the destruction of the bacterial cell surface and subsequently the plasma disinfection mechanisms, the interaction of ROS with prokaryotic peptidoglycan has been studied [13]. This corresponds to the case of Gram-positive bacteria that possess an outer protective barrier composed of peptidoglycan PG. Yusupov *et al* [13] studied the interactions of O, O₂ and O₃ with peptidoglycan, using the Reax force field [21]. The obtained results show that the dissociation of structural bonds (C–C, C–O and C–N) proceeds by prior H-abstraction by either O or O₃ plasma species. Most of the bond-breaking processes occur in the disaccharides. To limit the simulation time in these reactive simulations, a liquid water layer surrounding the peptidoglycan was not included.

In a complementary study, Yusupov *et al* [22] studied the interactions of O, O₂, O₃, OH, H₂O and H₂O₂ with peptidoglycan, by using also ReaxFF. The obtained results show that H₂O and O₂ are not reactive as expected. However, O, O₃ and OH species abstract a hydrogen atom from the peptidoglycan, which eventually leads to breaking up of the structure by a sequence of bond reorganizations. This is shown in Figure 3-6. The H₂O₂ molecules, on the other hand, react differently. Indeed, H₂O₂ molecules react with each other leading to the formation of HO₂, OH and H₂O. Then the formed HO₂ reacts with the PG structure. In order to save simulation time, as previously, the authors do not use liquid water layer.

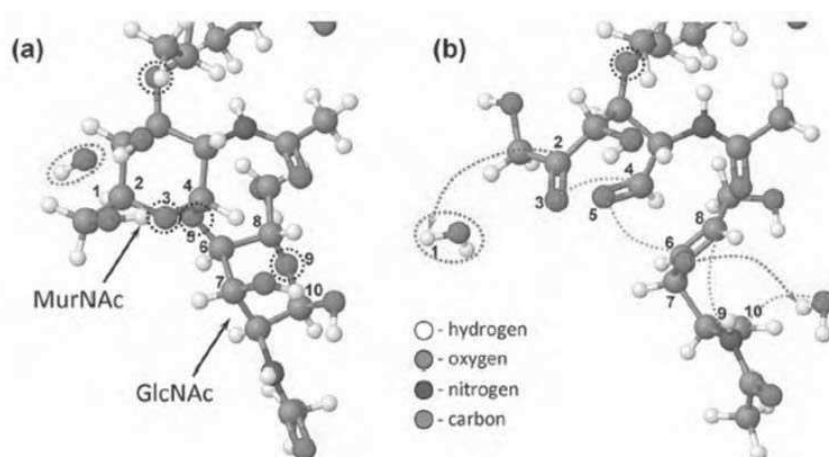


Figure 3-6 H-abstraction by an impinging OH radical (see red dashed oval in (a)) from the N-acetyl-muramic acid group of the peptidoglycan structure, leading to the breakup of the structure in (b), as predicted by reactive classical MD simulations [28]. The C and O atoms are numbered to better visualize the breakup of three ether bonds, i.e., the O₃-C₄, O₅-C₆, C₈-O₉ bonds are broken (see green dashed lines in (b)) and consequently some double C = O bonds are formed, i.e., C₂=O₃ and C₄=O₅ [22].

3.2.2.3 Reactive MD simulations for interaction of reactive species with DNA

A number of interesting simulation studies on the interactions of reactive species with DNA have been carried out as well. Abolfath and Brabec [23] carried out a series of Car-Parrinello and ReaxFF-based classical MD simulations to study the interactions of OH radicals with DNA. In a first study, the influence of the spin state of the DNA-deoxyribose sugar component on its interaction with OH radicals was studied. They found that by pumping the triplet state, hydrogen abstraction from the sugar was blocked, due to the formation of a free energy barrier. In their classical simulations [14], they show that OH radicals induce hydrogen abstraction from DNA, which leads to the formation of carbonyl and hydroxyl groups creating holes in the sugar rings. The oxygen from the OH radical weakens the C–N bond that attaches the sugar component to the nucleotide base, which finally leads to single and double strand break. This result was also reproduced in their later investigations [24].

3.2.2.4 Reactive MD simulations for interaction of reactive species with liquids

Biostructures are usually surrounded by a liquid, mainly consisting of water and complemented by a variety of other components. Many simulations addressed the adsorption, distribution and diffusion of various species at the air/water interface as well as in bulk water [25], [15], [26], [27] and [28].

Specifically in the context of plasma medicine, ReaxFF simulations of the behaviour of O, OH, and OH₂ and H₂O₂ species in water were carried out by Yusupov *et al* [15]. It was shown that OH, HO₂ and H₂O₂ easily travel through the water, in contrast to the O atoms, which immediately react with water molecules, resulting in the formation of two OH radicals. Furthermore, O, OH and HO₂ abstract H from water molecules, whereas no H-abstraction reaction was found to take place in the

case of H_2O_2 . Diffusion coefficients of 0.84 and $0.13 \text{ \AA}^2\text{ps}^{-1}$ are determined for OH and H_2O_2 . Their data are in good agreement with literature values. For OH_2 a diffusion coefficients of $0.07 \text{ \AA}^2 \text{ ps}^{-1}$ was calculated. OH is seen to diffuse by a continuous process of H-abstractions from water, thereby continuously creating new OH molecules. OH radicals are not observed to react within the simulated time scale of 100 ps. HO_2 radicals, however, react with each other, with the formation of H_2O_2 and O_2 . H_2O_2 radicals are also observed to react with each other with the formation of HO_2 and H_2O .

The adsorption of various species relevant for plasma medicine at the air/water interface was studied by Vacha *et al* [26]. Using classical MD simulations, the free energy profile of both hydrophilic OH, HO_2 and H_2O_2 species and hydrophobic O_2 , N_2 and O_3 molecules were calculated. A free energy minimum was obtained for all species at the interface, leading to an accumulation of all species in this region. The air/water interface may thus provide a reservoir of potentially reactive species.

These reactive MD simulations can give very interesting information about more particularly the bond-breaking of the molecular structure following a sequence of bond reorganizations [1]. Nevertheless, this needs for input data complex reactive force fields without for the moment any relevant link with transient pore creation. In other words, there are no literature MD simulations devoted to membrane permeabilization and pore formation when impacted by plasma actives species. Therefore, in order to contribute to a better understanding of the pore formation through cell membranes due to interactions with micro air plasma, we developed for the first time in literature a specific Monte Carlo poration model based on a macroscopic concept to simulate formation pores of few nanometer of width through cell multilayer membranes when impacted by air plasma species.

3.3 Monte Carlo poration model of cell membranes for application to plasma gene transfection

3.3.1 Descriptions of input data and Monte Carlo model

As already emphasized, the present Monte Carlo model, inspired from previous model for plasma deep silicon etching [29], is aimed to statistically simulate the pore formation during the interactions of the different plasma species with the membrane structure. Before the description of the Monte Carlo model, it is useful to give information on the method of estimation of the fluxes of plasma species impacting the membrane, the reaction processes between plasma species and cells membrane structure with the corresponding discretization domain.

3.3.1.1 Estimation of fluxes of plasma species impacting the cell membrane

The plasma species impacting the membrane come from a low-temperature air microplasma generated at atmospheric pressure. This plasma setup has been already used for gene transfection [30]. It can be considered as a pulsed corona discharge generated in ambient air from the tip of an anodic copper tube of 70 mm for outer diameter. An AC high voltage of 14 kV is applied between the anodic tube and the cathode well containing the treated cells with an electrode separation of 1 mm while the AC voltage frequency is equal to 20 kHz and the pulse frequency to 25Hz corresponding to a duty cycle of 1%. Further details on the power supply characteristics can be found elsewhere (cf. chapter 2 and [30]).

Due to the action of the high electric field close the anodic tip (see Figure 3-7 displaying the geometric electric field profile in the inter-electrode space), a pulsed corona discharge is developed at each cycle in ambient air. These discharges correspond to the well-known streamer mechanisms which allow the propagation of strong ionization waves until the cells placed at 1 mm in front of the tip inside one well of the 96-well microplate. The ionization waves generated in ambient air

and impacting the cell membranes involve various plasma species as electrons, ions and active neutral species as radicals (O, OH, etc.) or air by products (ozone, hydrogen peroxide, nitrogen oxides, etc.). In the following, in order to estimate the fluxes of plasma species impacting the membrane, we used a reaction kinetic model already developed in the case of corona discharges in flue gases[31] and adapted to the case of air microplasma used for gene transfection [30]. Furthermore, we also used the optical emission spectroscopy results obtained from the estimation of more particularly charged particles temperatures and densities, already detailed in chapter 2.

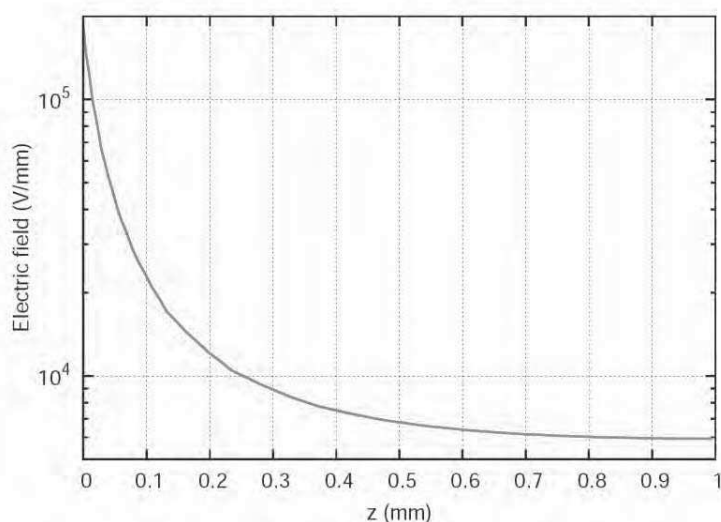


Figure 3-7 Variation of geometric electric field versus the inter-electrode space along the axis of the microplasma tube generating the corona discharge in humid ambient air for an applied anode voltage of 14 kV. This initial electric field initiating the discharge from the anodic tip ($z=0$) is calculated from solution of Laplace equation before the streamer propagation towards the cathode ($z=1\text{mm}$).

In fact, the proportion of the three considered plasma species (electrons, ions, and radicals) arriving to the membrane and assumed playing a role on the membrane poration are estimated from their fluxes calculated with the help of reaction kinetic model. We assumed only three kinds of plasma species in order to reduce the complexity of the Monte Carlo poration model at the

present stage of its development. However in the future, various kinds of species can be considered without any change on the basic concepts of the Monte Carlo model developed in the present work.

The main reactions, involved in this microplasma discharge in ambient air assumed involving 50% of humidity, have been considered in the reaction kinetic model. The reactions in the gas phase just before the plasma impacts with the cell membranes are:

1. Electron interactions with ambient air including N_2 , O_2 and H_2O and leading to gas dissociation, excitation, ionization, attachment and also recombination between electron and positive ions.
2. Interactions of ions and gas leading to charge transfer, ion conversion, electron detachment and recombination between negative and positive particles.
3. Interactions involving long living excited species and leading for instance to ionization.
4. Reaction between dissociated neutral species as radical and gas molecules.

The reaction kinetic model needs the *a priori* knowledge of:

1. The reaction coefficients of all the previously listed interactions between plasma species and ambient air: the reaction coefficients involving electrons interacting with molecules of ambient humid air are calculated using a multi-term solution of Boltzmann equation [32] using sets of electron-molecule (N_2 , O_2 and H_2O) collision cross sections taken from [33] and [23].
2. The profile of electron energy that initiates and starts all these various interactions: the electron energy profile has been calculated using streamer dynamics model already developed [34] and adapted to the case of plasma generated in humid air by the microplasma electrode configuration. This streamer dynamics model based on local energy approximation is quite similar to another literature model [35]. Figure 3-8 displays an

example of the time evolution of electron mean energy near the cathode well. This can reach several eV in the streamer head as already given in OES results of chapter 2. While the neutral species remains close to the gas temperature (around 310 K) and the ion species have a temperature slightly higher than gas temperature. This is because our low-temperature plasma has, as expected, the properties of weakly ionized plasmas with a low ionization degree dominated by the concentration of neutral background molecules. Such energy profile has been confirmed by using OES of the microplasma, given in chapter 2.

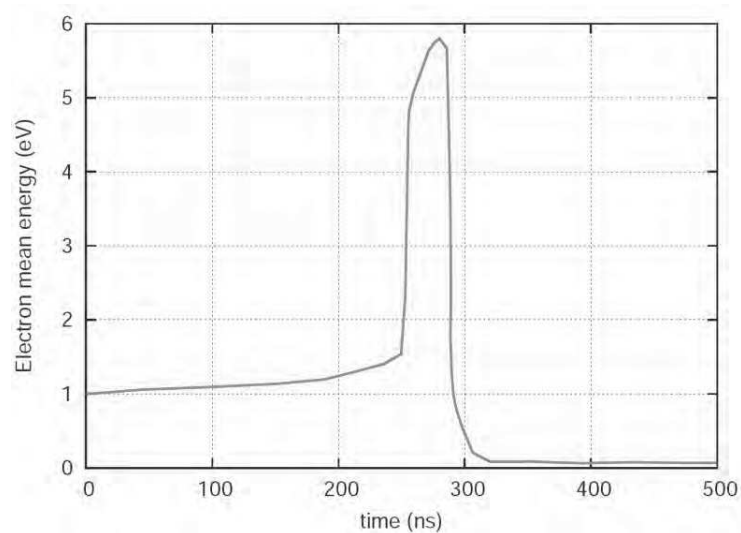


Figure 3-8 Time evolution of electron mean energy in a streamer-like propagated from the micro-tube up to the cathode for the case of corona discharge in humid ambient air and for a position near the cathode.

3. The reaction coefficients of heavy particles (radicals or ions or excited species) impacting molecules of background: these gas data have taken from ref [31] while the specific data of ions interacting with background gas has taken from ref [34].

Therefore, using reaction kinetic model coupled with electron energy profile estimated from streamer dynamics model, the fluxes of electrons, ions, and radicals impinging the cell membrane

surface can be estimated as the products of their respective densities and drifts or mean velocities. The densities of electrons (about 10^{14} cm^{-3}), positive ions (about $5 \times 10^{14} \text{ cm}^{-3}$) and radicals (10^{15} cm^{-3}) are calculated from kinetic reaction model. These obtained magnitude of electrons and ions densities are coherent with those obtained from OES spectroscopy measurements presented in the second chapter of the present thesis. The mean velocity of charged particles (electrons and ions) are determined from streamer dynamics model and the mean velocity of radical is assumed equal to thermal gas velocity. The electron flux (equal to about $2.5 \times 10^{21} \text{ cm}^{-2}/\text{s}$) is the dominant one while the ion flux (close to $5 \times 10^{19} \text{ cm}^{-2}/\text{s}$) is about 2 decades lower than electron flux and the radical flux (close to $5 \times 10^{18} \text{ cm}^{-2}/\text{s}$) 3 decades lower. The estimated fluxes will be summarized with further simulation input data in Table 4.1 of sub-section 4.2

3.3.1.2 Reaction processes with cell membrane

Knowing that the density of plasma species can be very high (around 10^{14} cm^{-3} for electron density for instance) in the case of the considered microplasma at atmospheric pressure, it is not possible to consider in the Monte Carlo poration model each plasma particle at the individual scale. This is why we adopted in our model a macroscopic concept with a coarse grained approximation. Thus each species is considered as a macro-species (or super-particles or pseudo-particles) representing a large number of particles. A super-particle is a computational particle that represents a lot of real particles. Essential physics can be captured with a much smaller number of particles than that in a real plasma. The number of real particles corresponding to a super-particle must be chosen such that sufficient statistics can be collected on the particle motion. Noting that the idea of pseudo-particles was already used for instance in the case of PIC-Monte Carlo simulations of radio-frequency electrical discharges at low pressure applied to thin film deposition in micro-electronics device [36]. Furthermore, the membrane is assumed like a multi-layer structure and

each layer is assumed like homogeneous medium of macromolecules of either lipids or proteins. The successive interactions with membrane layers is assumed as global or macro-processes involving the incident plasma super-particles (electrons or ions or radicals) arriving to the membrane surface.

Therefore, the interactions between the plasma species and the membrane are described in a statistical way. In fact, the super-site concept assumes that, when an event occurs between the plasma particle and the super-site, it is like if a large number of N particles from the plasma interact in the same way with N real sites composing the considered super-site.

The assumed macro-processes during the interactions of plasma particles with the membrane layers can be:

1. Non-activated layer mesh (or virgin site) opening: this corresponds to the breaking of the molecular bonds during the plasma species impacts.
2. Layer mesh (or site) activation leading to activated site: during this process, the incident plasma species contribute to weaken the molecular bonds. It is a kind of bio-polymer excitation which decreases the breaking potential (or the activation energy) of the chemical bond in the aim to prepare its breaking during impacts with the next incident plasma species. In other words, an activated site is more suitable for the event of an opening process.
3. Layer mesh (or site) opening of activated site: as already stated and after the activation of a site, the latter is ready to be opened by impact with another plasma species. It is equivalent to bond-breaking at the level of the molecular organization.

4. Particle recombination or neutralization with layer mesh (or site): it can be considered equivalent to the formation of new molecular bonds when the plasma particle is physically or chemically adsorbed by the surface matter at the scale of the considered site.
5. Particle reflection on the pore surfaces: it is a change of the incident direction during the impact with the membrane matter at the scale of the considered site.

The event probabilities of these different processes depend on the considered particle (electrons or ions or radicals) and also on the layer nature (phospholipid for layers 2 and 3 or protein for layers 1 and 4), see in Figure 3-9. In the case of a reflection process, the particle is generally subjected to new displacements until to reach an occupied (or full) site inside the membrane layer.

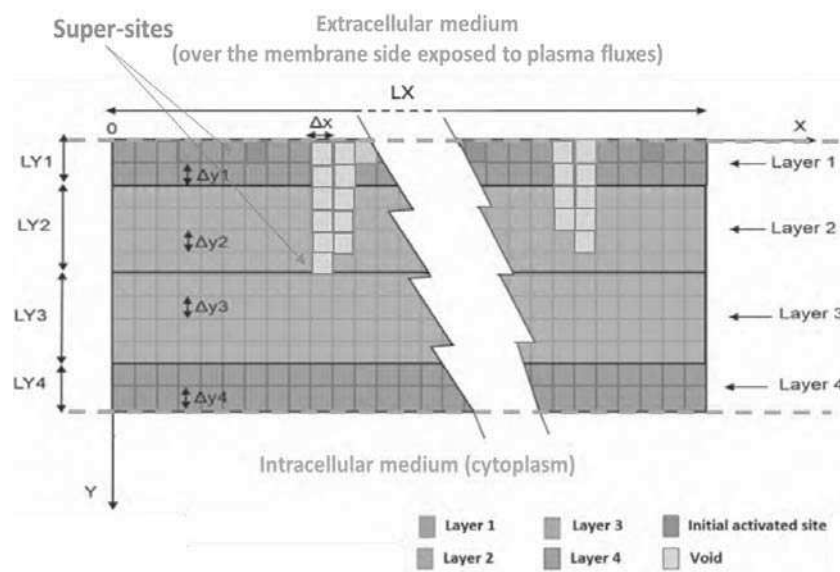


Figure 3-9 Multilayer membrane model and discretization domain.

In fact, a specific probability of occurrence of each macro process is assigned to each super-particle based on a large parametric study of the whole considered processes between plasma species and membrane. It is noteworthy that the different reaction probabilities have been chosen in coherence with the bio-physical composition (phospholipids or proteins) of each layer of the

membrane. This consists to establish a relation between for instance the magnitude of the opening probability of activated site and the density of the layer (phospholipid or protein) on which the activated site is opened when impacted by the considered plasma species. The smaller the layer density, the higher is the necessary amplitude of the opening probability. In other words, the opening probability magnitude has been assumed inversely proportional to the layer density.

3.3.1.3 Membrane structure and discretization domain

A very simple membrane model is considered to develop the Monte Carlo model of membrane cell poration. The membrane structure is assumed as a "sandwich" of a phospholipid bilayer covered on each side by a thin protein layer [37]. Obviously, this simplified membrane model is not representative of real membrane which can have a more complex structure composed by a bilayer phospholipid crossed by trans-membrane scaffold protein [38]. More generally, membrane is described [39] as an assembly of lipids, proteins and carbohydrates self-organized into a thin barrier that separates the interior of cell compartments from the outside environment. The main lipid constituents of natural membranes are phospholipids that arrange themselves into a bilayer. In the present Monte Carlo code, the structure of the membrane which is an input data is totally interchangeable and will be therefore changed in a future work by a more complex membrane model.

Figure 3-9 displays the 2D simulation domain represented by a superposition of four layers (two external protein layers represented in blue with thicknesses LY1 and LY4 and two wider internal lipid layers in green with thicknesses LY2 and LY3). The sum of the four layer thicknesses is chosen coherent with usual membrane thickness (for instance LY1+LY2+LY3+LY4 close to 10 nm). The simulation domain is discretized into small meshes called super-sites with regular step sizes Δx and Δy along x and y axes. The step sizes can be chosen regular or not. Each mesh

represents a large number of macro-molecules proportional to the density of the real number of molecules of lipids or proteins of the considered layer. As previously emphasized and in the framework of this coarse grained approximation, the interactions are assumed occurring between plasma super-particles and macro-molecules of the different layer meshes. This macroscopic concept does not require a definition at the molecular or atomic scale of the membrane.

At the beginning of the simulation, a given plasma super-particle interacts first with the surface of layer 1. This is why the surface of layer 1 is initialized by an *a priori* known distribution of activated sites that are the starting point of the pore formation. The fraction of the activated sites uniformly distributed over the surface of layer 1 can be chosen for instance from experimental observations of the membrane surface morphology at the microscopic-scale using for instance the fluorescence microscopy or atomic force microscopy observations. When these initial activated sites are impacted by incident plasma particles, they can be transformed into void site (or opened site) thus starting the sequences of membrane opening.

It is worth noting that each super-site (or mesh) is numerically defined by a reduced matrix of numbers associated to the state of the mesh before or after the interactions with every plasma species. The different possible states of a given super-site inside a given layer can be for instance non-activated (i.e. virgin) site or activated site or void (i.e. opened) site.

3.3.2 Description of Monte Carlo poration model

3.3.2.1 Flowchart of the Monte Carlo poration model

Figure 3-10 displays a simplified flowchart of the developed Monte Carlo poration model that describes the successive simulation steps from the interactions with the surface of layer 1 up to the pore formation when crossing the four considered layers following the previously evocated different reaction processes already described in sub-section 3.3.1.2.

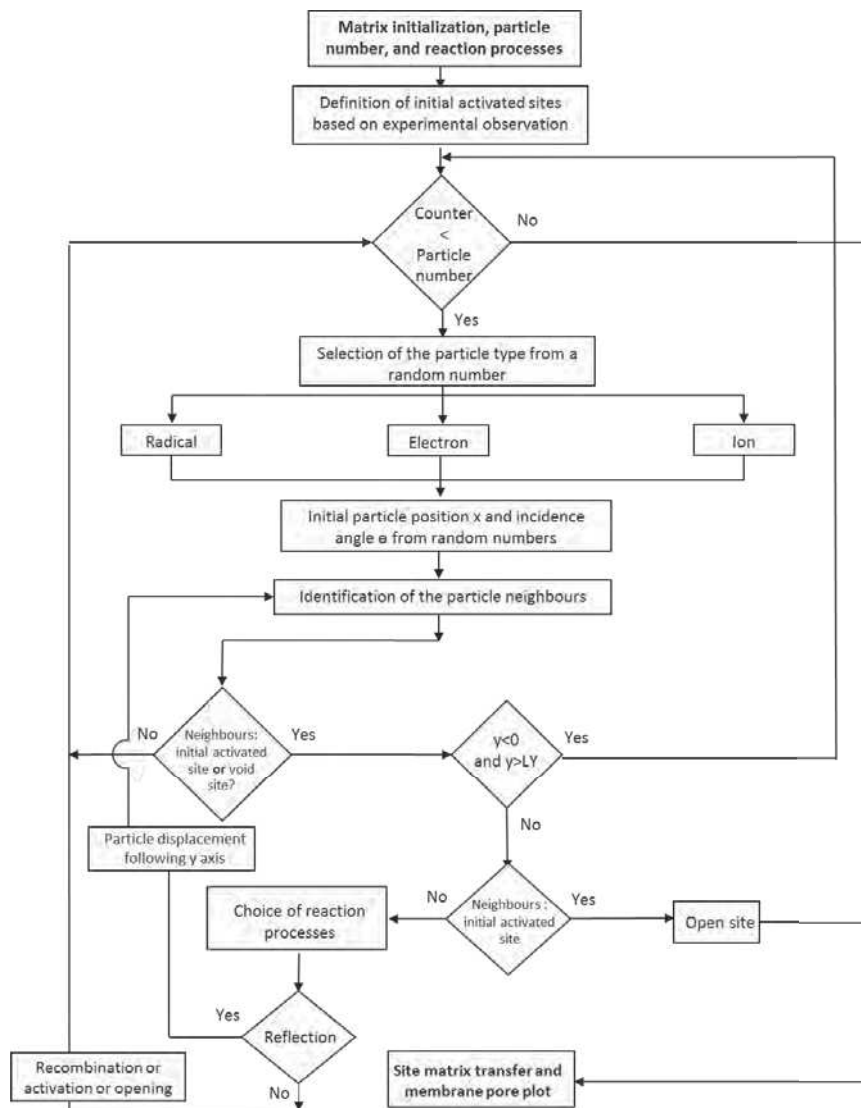


Figure 3-10 Simplified flowchart of Monte Carlo method for pore formation.

For each super-particle (electrons or ions or radicals), a given number of initial particles is chosen proportional to the corresponding particle flux. The plasma particle interacting with the layer surface is selected from uniform random number compared to the fraction of particle flux over total flux. The position $(x_{p,s}, y_{p,s})$ of the super-particle p along x axis inside the super-site s and the distribution of the incident angle $\theta_{p,s}$ are also determined from random numbers. In this case we assume that plasma flux arrives on the surface membrane with a uniform distribution along

x axis. Noting that $x_{p,s}$ varies between 0 and surface length LX , following a uniform distribution. While $y_{p,s}$ was assumed constant for the interactions with the first surface layer and equal to a fraction of the mesh step size ($y_{p,s}=\Delta y/10$) in the beginning of the simulation at the domain entrance (surface layer 1). Furthermore, the incident angle $\theta_{p,s}$ follows in the case of electron flux a strongly anisotropic distribution having a Gaussian distribution with a very small full-width at half maximum (FWHM). This favors the forward direction of the plasma flux i.e. the direction perpendicular to the surface membrane. Due to a lower magnitude of ion and radical temperatures which are close to the gas temperature in comparison to electron temperature, the anisotropy of ion and radical fluxes are chosen less sharp with a small opening angle (10°) in the forward direction. This assumption is coherent with the considered microplasma [30] that behaves as a corona discharge between the anodic tip and cell membranes. Indeed, the electron energy (or kinetic temperature) can reach several eV in the streamer head of the present air corona discharge (see e.g. chapter 2). Moreover, the plasma fluxes move in the forward direction toward the cell membranes, first by the charged particle transport and second by the known self-induced electric wind that moves all the plasma species (charged or neutral) with a velocity of several m/s or even more due to momentum transfers between charged and neutral species [40].

3.3.2.2 Identification of the targeted super-particle neighbours

The interactions between super-particles and super-sites are treated using predefined reaction probabilities for the different macro-processes based on a parametric study (for more details see section 4.3 of chapter 4). Before and after each process occurring in a super-site, the entire four nearest super-particle neighbours need to be identified, as displayed in Figure 3-11

It is worth mentioning that each super-particle can interact with only one of the four neighbours. The choice of the target neighbour site is based on the uniform random number depending on the

neighbour site state, the particle type, the layer composition and the predefined reaction probabilities.

After each interaction between plasma particle and a given neighbour site, the new matrix numbers are stored in order to take into account the change occurring inside the considered super-site (or mesh). When the considered super-activation particle interacts with a full (i.e. occupied) site and undergoes a specific end-process (as site activation or recombination or opening, etc.), a new particle, is therefore, selected. The Monte Carlo simulation is stopped when the entire considered number of each kind of super-particle are treated. During Monte Carlo simulation, each selected super-particle is displaced until to interact with the first super-site of the surface or with a full (or occupied) super-site corresponding to the pore walls or to the bottom of a given pore. The elementary particle displacement dl for an elementary variation along x and y axis is defined as:

$$dl = (\Delta x^2 + \Delta y^2)^{1/2} \quad (\text{Eq-3-1})$$

The new position $x_{p,s+1}$ of the current super-particle p is determined from its initial coordinates $x_{p,s}$, $y_{p,s}$, the incidence angle $\theta_{p,s}$ and a factor f modulating the magnitude of displacement:

$$x_{p,s+1} = x_{p,s} + f \times dl \times \cos(\theta_{p,s}) \quad (\text{Eq-3-2})$$

$$y_{p,s+1} = y_{p,s} + f \times dl \times \sin(\theta_{p,s}) \quad (\text{Eq-3-3})$$

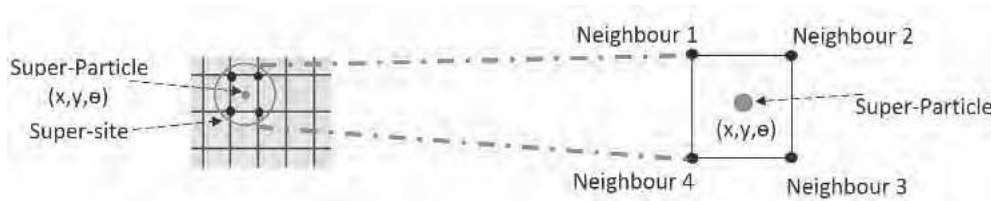


Figure 3-11 Reduced matrix of super-site scheme and the 4 nearest neighbours.

3.4 Conclusion

This chapter has first of all devoted to a literature review, where we have underlined the current status of simulations in the field of plasma biomolecules interactions. This is a highly complex field, and until now, not so many simulation studies have been carried out. A reasonable number of studies have been devoted to molecular processes in electroporation, and a few studies also addressed reactive interactions of plasma species with biomolecules. However, there is no previous modeling of membrane poration when living cells are impacted by low-temperature plasma species. Moreover, as already stated in the literature the plasma-induced mechanisms of more particularly the membrane poration and the control of pore sizes are not clear enough. Therefore, in order to contribute to a better understanding of the pore formation through cell membranes due to interactions with micro-air plasma, we developed a specific Monte Carlo poration model.

Thus, the major aim from this chapter was to give a description of the developed Monte Carlo poration model. The latter was inspired from literature researches performed in low pressure plasmas used for deep silicon etching in power electronic devices. This simulation model of membrane permeabilization was based on macroscopic concepts using a coarse grained approximation. The three kinds of considered plasma species (electrons, ions, and radicals) are assumed as super-particles. Each super-particle (electron or ion or radical) groups a large number of particles. This avoids huge computational times since the density of each particle can be higher than 10^{14}cm^{-3} in the considered air microplasma already used elsewhere in experimental gene transfection. Furthermore, we considered a simplified membrane model involving four thin layers including two phospholipid internal layers sandwiched by two external protein layers. Each layer is assumed composed by a succession of super-sites in which can occur, during their impacts with super-particles, several kinds of macro processes (recombination, reflection, activation of

supersite, opening of super-site). The electron flux, as well as ion and radical fluxes are estimated from optical emission spectroscopy OES coupled to a reaction kinetic model using as input data an electron mean energy profile reaching several eV and calculated using a standard streamer dynamics model. In addition, in the framework of the air microplasma, the dominant particle flux impacting the membrane is the electron flux (equal to about 2.5×10^{21} cm⁻²/s) one while the ion flux (close to 5×10^{19} cm⁻²/s) is about 2 decades lower than electron flux and the radical flux (close to 5×10^{18} cm⁻²/s) 3 decades lower. For each super-particle (electrons or ions or radicals), a specific number of initial particles is chosen proportional to the corresponding estimated particle flux. The type of the particle p , its position $(x_{p,s}, y_{p,s})$ along x axis inside the super-site s and the angular distribution of the incident angle $\theta_{p,s}$ are determined from random numbers. The different successive simulation steps of the developed Monte Carlo poration model was presented in a simplified flowchart. The steps start from the interactions of the super-particle with the first layer up to the pore formation crossing the four considered layers and following the different reaction processes. In addition, among the most important steps in the exploitation of the present Monte Carlo poration model, the estimation of probability of occurrence of whole predicted macro-processes is more than necessary. For this purpose, the following chapter, will be devoted more particularly to a wider parametric study, involving the different reaction processes between super-particles and layer-meshes to better emphasize processes playing the main role in membrane poration and permeabilisation.

3.5 References

- [1] E. C. Neyts, M. Yusupov, C. C. Verlaack, and A. Bogaerts, "Computer simulations of plasma–biomolecule and plasma–tissue interactions for a better insight in plasma

- medicine,” *J. Phys. D. Appl. Phys.*, vol. 47, pp. 293001, 2014.
- [2] A. A. Gurtovenko and I. Vattulainen, “Pore Formation Coupled to Ion Transport through Lipid Membranes as Induced by Transmembrane Ionic Charge Imbalance: Atomistic Molecular Dynamics Study,” *J. Am. Chem. Soc.*, vol. 127, pp. 17570–17571, 2005.
- [3] J. C. Weaver, “Electroporation: A general phenomenon for manipulating cells and tissues,” *J. Cell. Biochem.*, vol. 51, pp. 426–435, 1993.
- [4] Q. Hu, S. Viswanadham, R. Joshi, K. Schoenbach, S. Beebe, and P. Blackmore, “Simulations of transient membrane behavior in cells subjected to a high-intensity ultrashort electric pulse,” *Phys. Rev. E*, vol. 71, pp. 031914, 2005.
- [5] D. P. Tieleman, H. Leontiadou, A. E. Mark, and S.-J. Marrink, “Simulation of Pore Formation in Lipid Bilayers by Mechanical Stress and Electric Fields,” *J. Am. Chem. Soc.*, vol. 125, pp. 6382–6383, 2003.
- [6] W. F. Van Gunsteren and H. J. C. Berendsen, “Groningen Molecular Simulation (GROMOS),” in *Library manual (Nijenborgh, Groningen)*, pp. 1–221, 1987.
- [7] Q. Hu, Z. Zhang, H. Qiu, M. G. Kong, and R. P. Joshi, “Physics of nanoporation and water entry driven by a high-intensity, ultrashort electrical pulse in the presence of membrane hydrophobic interactions,” *Phys. Rev. E*, vol. 87, pp. 032704.1–032704.9, 2013.
- [8] R. a Böckmann, B. L. de Groot, S. Kakorin, E. Neumann, and H. Grubmüller, “Kinetics, statistics, and energetics of lipid membrane electroporation studied by molecular dynamics simulations.,” *Biophys. J.*, vol. 95, pp. 1837–1850, 2008.
- [9] M. Tarek, “Membrane electroporation: a molecular dynamics simulation.,” *Biophys. J.*, vol. 88, pp. 4045–53, 2005.
- [10] P. T. Vernier, Z. A. Levine, Y. H. Wu, V. Joubert, M. J. Ziegler, L. M. Mir, and D. P. Tieleman, “Electroporating fields target oxidatively damaged areas in the cell membrane,” *PLoS One*, vol. 4, pp. e796.1–e796.8, 2009.
- [11] L. Delemotte and M. Tarek, “Molecular dynamics simulations of lipid membrane electroporation,” *J. Membr. Biol.*, vol. 245, pp. 531–543, 2012.
- [12] N. Y. Babaeva and M. J. Kushner, “Intracellular electric fields produced by dielectric barrier

- discharge treatment of skin,” *J. Phys. D. Appl. Phys.*, vol. 43, pp. 185206.1–185206.12, 2010.
- [13] M. Yusupov, E. C. Neyts, U. Khalilov, R. Snoeckx, A. C. T. Van Duin, and A. Bogaerts, “Atomic-scale simulations of reactive oxygen plasma species interacting with bacterial cell walls,” *New J. Phys.*, vol. 14, pp. 093043.1–093043.18, 2012.
- [14] R. M. Abolfath, A. C. T. van Duin, and T. Brabec, “Reactive Molecular Dynamics Study on the First Steps of DNA Damage by Free Hydroxyl Radicals,” *J. Phys. Chem. A*, vol. 115, pp. 11045–11049, Oct. 2011.
- [15] M. Yusupov, E. C. Neyts, P. Simon, G. Berdiyrov, R. Snoeckx, A. C. T. van Duin, and A. Bogaerts, “Reactive molecular dynamics simulations of oxygen species in a liquid water layer of interest for plasma medicine,” *J. Phys. D. Appl. Phys.*, vol. 47, pp. 25205, 2014.
- [16] B. Ni, K-H. Lee, and S. B. Sinnott, “A reactive empirical bond order (REBO) potential for hydrocarbon–oxygen interactions,” *J. Phys. Condens. Matter*, vol. 16, pp. 7261, 2004.
- [17] J. Van der Paal, S. Aernouts, A. C. T. van Duin, E. C. Neyts, and A. Bogaerts, “Interaction of O and OH radicals with a simple model system for lipids in the skin barrier: a reactive molecular dynamics investigation for plasma medicine,” *J. Phys. D. Appl. Phys.*, vol. 46, pp. 395201, 2013.
- [18] M. Yusupov, J. Van Der Paal, C. C. W. Verlackt, N. Khosravian, E. C. Neyts, and A. Bogaerts, “Plasma interaction with phospholipid bilayer : molecular dynamics simulations,” in *22nd international symposium on plasma chemistry (ISPC)*, 2015.
- [19] M. Elstner, D. Porezag, G. Jungnickel, J. Elsner, M. Haugk, T. Frauenheim, S. Suhai, and G. Seifert, “Self-consistent-charge density-functional tight-binding method for simulations of complex materials properties,” *Phys. Rev. B*, vol. 58, pp. 7260–7268, 1998.
- [20] S. J. Marrink, H. J. Risselada, S. Yefimov, D. P. Tieleman, and Alex H. de Vries, “The MARTINI Force Field: Coarse Grained Model for Biomolecular Simulations,” *J. Phys. Chem. B*, vol. 111, pp. 7812–7824, 2007.
- [21] A. Bogaerts, M. Eckert, M. Mao, and E. Neyts, “Computer modeling of the plasma chemistry and plasma-based growth mechanisms for nanostructured materials,” *J. Phys. D. Appl. Phys.*, vol. 44, pp. 174030, 2011.

- [22] M. Yusupov, A. Bogaerts, S. Huygh, R. Snoeckx, A. C. T. van Duin, and E. C. Neyts, "Plasma-Induced Destruction of Bacterial Cell Wall Components: A Reactive Molecular Dynamics Simulation," *J. Phys. Chem. C*, vol. 117, pp. 5993–5998, 2013.
- [23] R. M. Abolfath and T. Brabec, "DNA-Backbone Radio Resistivity Induced by Spin Blockade Effect," *J. Comput. Chem.*, vol. 31, pp. 2601–2606, 2010.
- [24] R. M. Abolfath, D. J. Carlson, Z. J. Chen, and R. Nath, "A molecular dynamics simulation of DNA damage induction by ionizing radiation," *Phys. Med. Biol.*, vol. 58, pp. 7143–7157, 2013.
- [25] S. Chalmet and M. F. Ruiz-López, "The structures of ozone and HOx radicals in aqueous solution from combined quantum/classical molecular dynamics simulations," *J. Chem. Phys.*, vol. 124, pp. 194502, 2006.
- [26] R. Vácha, P. Slaviček, M. Mucha, B. J. Finlayson-Pitts, and P. Jungwirth, "Adsorption of Atmospherically Relevant Gases at the Air/Water Interface: Free Energy Profiles of Aqueous Solvation of N₂, O₂, O₃, OH, H₂O, HO₂, and H₂O₂," *J. Phys. Chem. A*, vol. 108, pp. 11573–11579, 2004.
- [27] M. G. Campo and J. R. Grigera, "Classical molecular-dynamics simulation of the hydroxyl radical in water," *J. Chem. Phys.*, vol. 123, pp. 084507, 2005.
- [28] S. Du and J. S. Francisco, "Interaction between OH Radical and the Water Interface," *J. Phys. Chem. A*, vol. 112, pp. 4826–4835, 2008.
- [29] G. Marcos, A. Rhallabi, and P. Ranson, "Monte Carlo simulation method for etching of deep trenches in Si by a SF₆/O₂ plasma mixture," *J. Vac. Sci. Technol. A Vacuum, Surfaces, Film.*, vol. 21, pp. 87–95, 2003.
- [30] M. Jinno, Y. Ikeda, H. Motomura, Y. Kido, K. Tachibana, and S. Satoh, "The Necessity of Radicals for Gene Transfection by Discharge Plasma Irradiation," *J. Photopolym. Sci. Technol.*, vol. 27, pp. 399–404, 2014.
- [31] O. Eichwald, M. Yousfi, A. Hennad, and M. D. Benabdessadok, "Coupling of chemical kinetics, gas dynamics, and charged particle kinetics models for the analysis of NO reduction from flue gases," *J. Appl. Phys.*, vol. 82, pp. 4781, 1997.

- [32] M. Yousfi and M. D. Benabdessadok, “Boltzmann equation analysis of electron-molecule collision cross sections in water vapor and ammonia,” *J. Appl. Phys.*, vol. 80, pp. 6619, 1996.
- [33] G. Ruíz-Vargas, M. Yousfi, and J. de Urquijo, “Electron transport coefficients in the mixture of H₂O with N₂, O₂, CO₂ and Dry Air for the Optimization of Non-Thermal Atmospheric Pressure Plasmas,” *J. Phys. D. Appl. Phys.*, vol. 43, pp. 455201, 2010.
- [34] D. Nelson, M. Benhenni, O. Eichwald, and M. Yousfi, “Ion swarm data for electrical discharge modeling in air and flue gas mixtures,” *J. Appl. Phys.*, vol. 94, pp. 96–103, 2003.
- [35] S. Dujko, A. H. Markosyan, R. D. White, and U. Ebert, “High-order fluid model for streamer discharges: I. Derivation of model and transport data,” *J. Phys. D. Appl. Phys.*, vol. 46, pp. 475202, 2013.
- [36] K. Radouane, L. Date, M. Yousfi, B. Despax, and H. Caquineau, “RF discharge modeling in a N₂O/SiH₄ mixture for SiO₂ deposition and comparison with experiment,” *J. Phys. D. Appl. Phys.*, vol. 33, pp. 1332, 2000.
- [37] H. Danielli, and J. F. Davson, “A contribution to the theory of permeability of thin films,” *J. Cell. Comp. Physiol.*, vol. 5 (4), pp. 495–508, 1935.
- [38] T. H. Bayburt, Y. V. Grinkova, and S. G. Sligar, “Self-Assembly of Discoidal Phospholipid Bilayer Nanoparticles with Membrane Scaffold Proteins,” *Nano Lett.*, vol. 2, pp. 853–856, 2002.
- [39] Gennis RB, “Biomembranes: molecular structure and function,” in *Springer*, Berlin Heidelberg New York, 1989.
- [40] J. Batina, F. Noël, S. Lachaud, R. Peyrous, and J. F. Loiseau, “Hydrodynamical simulation of the electric wind in a cylindrical vessel with positive point-to-plane device,” *J. Phys. D. Appl. Phys.*, vol. 34, pp. 1510–1524, 2001.

CHAPTER 4

RESULTS AND DISCUSSION ON MONTE CARLO SIMULATIONS OF MEMBRANES PORATION BY GASEOUS PLASMA SPECIES

4.1 Introduction

During the previous chapter, we presented a detailed description of the present Monte Carlo poration model. The latter was developed to simulate the pore formation of few nanometre of wide through cell multilayer membranes when impacted by air microplasma species. We assumed each plasma species as a super-particle grouping a large number of particles. The membrane layers were assumed as a simple membrane model superposing four layers of phospholipids and proteins. Moreover, each layer was constituted by a succession of super-sites subjected to the known macro-processes (recombination, reflection, activation of site, opening) during the membrane impacts by the plasma super-particles. For an accurate exploitation of our Monte Carlo poration model, the estimation of probability of occurrence of whole predicted macro-processes is absolutely necessary. Thus, in this chapter, a large parametric study is conducted. The target is to evaluate the effects of the initial simulation parameters, as well as the magnitude of the occurrence probabilities of each reaction process on the cell membrane permeabilization and pore formation.

This chapter is initially devoted to a description of the computational simulation conditions taking into account the initial particle number, the simulation domain geometry, as well as the fraction of the initial activated sites. Moreover, we described the considered reaction

probabilities and the notations used of each considered process between plasma super-particles and membrane super-sites. These reaction probabilities are selected in a suitable way based on some biophysical considerations; as for example the magnitude of the layer density (either protein or lipid layer), the plasma super-particle type and energy level. Furthermore, the super-site state is also considered as a factor determining the choice of reaction probabilities.

The second part of this chapter is oriented on discussions and analysis of the Monte Carlo numerical modeling results obtained from the large parametric study. More precisely, we discuss the effects of the initial incidence angle of ions, and radicals, the effect the energy distribution of the electron, as well as the effects of reaction as for instance the role of the reflection process in the case of ions, and radicals, and the importance of the electron in the super-site opening process. Finally, an investigation on the effects of the variation of the initial particle number N_p on the pore formations is analyzed to show some correlations with experimental gene transfection results obtained at Ehime University. This comparison will allow us to discuss the Monte Carlo model validation.

4.2 Computational simulation conditions

Present stochastic poration method is aimed to simulate the pore formation under specific parameters of plasma particles impinging the membrane surface. The simulation parameters are summarized in table 4-1. As already stated in chapter 3, the considered number of initial total super-particles is chosen proportional to the corresponding particle flux. It is varied from $N_p=4 \times 10^5$ to 1.8×10^6 , because it has been empirically observed negligible pore formation for $N_p < 6 \times 10^5$ and a strong membrane removal for $N_p > 1.4 \times 10^6$. The information on the flux fractions of ions F_{ion} and radicals F_{rad} relative to electron flux is chosen coherent with the considered low-temperature plasma, i.e.

$$F_{ion} = \text{Ion flux} / \text{electron flux} = 10^{-2} \quad (\text{Eq-4-1})$$

$$F_{rad} = \text{Radical flux/electron flux} = 10^{-3} \quad (\text{Eq-4-1})$$

Concerning the discretization domain, the membrane length LX was taken equal to 100 nm with thickness LY equal to 10 nm. The latter is divided into external protein layers with thicknesses LY1=LY4=2 nm, and two internal lipid layers with thicknesses LY2=LY3=3 nm. The simulation domain is discretized into 16000 small regular meshes (super-sites) with step sizes $\Delta x = \Delta y = 0.25$ nm. Last, the fraction of the initial activated sites which are the starting points of the pore formation on the first upper layer (layer 1) is chosen equal to 10^{-2} . This corresponds in our simulation to five activated sites uniformly distributed over the surface layer 1.

Table 4-1 Considered parameters in the framework of Monte Carlo simulations.

Total initial Particle number and plasma fluxes	Total number of initial particles $N_p = 4 \times 10^5$ up to 1.8×10^6 (electrons, ions, and radicals)		
	Radical flux/Electron flux	2×10^{-3}	
	Ion flux/Electron flux	2×10^{-2}	
Sizes of Membrane layers	Length LX	100	[nm]
	Membrane thickness LY	10	[nm]
	Layer 1 thickness LY1	2	[nm]
	Layer 2 thickness LY2	3	[nm]
	Layer 3 thickness LY3	3	[nm]
	Layer 4 thickness LY4	2	[nm]
Discretization	Step size $\Delta x = \Delta y$	0.25	[nm]
	Mesh number	16000	
	Fraction of activated sites on layer1 surface	10^{-2}	

4.3 Reaction probabilities in the case of each super-particle

The notations used for the reaction probabilities of the considered processes between plasma super-particles and membrane super-sites are summarized in Table 4-2. In the case of electrons interactions and with an aim of comparison, we assume on the one hand a mono energetic beam with the following notations:

- $P_{e_Act_V-s}$ corresponds to probability of site activation.
- $P_{e_2xAct-s}$ corresponds to probability of double site activation.
- $P_{e_Rec_V-s}$ and $P_{e_Rec_Act-s}$ correspond respectively to recombination or neutralization inside a no activated and an activated site.
- The probabilities $P_{e_Op_V-s}$ and $P_{e_Op_Act-s}$ are associated respectively to opening of no activated and activated site.

On the other hand, we will assumed an energy distribution divided into three electron energy ranges (25% of weak energy, 50% of average energy and 25% of high electron energy). The reaction processes and their notations are almost same as those used for mono-energetic beam :

- $P_{e_weak_Act_V-s}$, $P_{e_avrg_Act_V-s}$, and $P_{e_high_Act_V-s}$ correspond to activation site probability processes. Noting that indexes weak, avrg, and high are, respectively, for weak, average, and high electron energy distribution.
- $P_{e_weak_2xAct-s}$, $P_{e_avrg_2xAct-s}$, and $P_{e_high_2xAct-s}$ are used for double site activation probabilities.
- $P_{e_weak_Rec_V-s}$, $P_{e_avrg_Rec_V-s}$, and $P_{e_high_Rec_V-s}$ are associated to super-particle recombination or neutralization inside a no activated site.
- The probabilities $P_{e_weak_Rec_Act-s}$, $P_{e_avrg_Rec_Act-s}$, and $P_{e_high_Rec_Act-s}$ correspond to recombination inside an activated site.
- $P_{e_weak_Op_V-s}$, $P_{e_avrg_Op_V-s}$, $P_{e_high_Op_V-s}$ and $P_{e_weak_Op_Act-s}$, $P_{e_avrg_Op_Act-s}$, $P_{e_high_Op_Act-s}$ correspond respectively to probabilities of opening of no activated and activated site.

Table 4-2 Notations and data used for the reactions probabilities

Reactions Processes	Notation	Electrons				Radicals	Ions						
		Weak energy		High energy									
Virgin site	Site activation	$P_{e_weak_Act_V-s}$		$P_{e_high_Act_V-s}$		/	/						
	Reaction	Layer1	Layer2	Layer3	Layer4	Layer1	Layer2	Layer3	Layer4	Layer1	Layer2	Layer3	Layer4
	Probabiilit	0.4	0.56	0.56	0.4	0.55	0.77	0.77	0.55	0.65	0.91	0.91	0.65
	Notation	$P_{e_weak_Op_V-s}$		$P_{e_high_Op_V-s}$		$P_{ion_Op_V-s}$		/					
Site opening	Reaction	Layer1	Layer2	Layer3	Layer4	Layer1	Layer2	Layer3	Layer4	Layer1	Layer2	Layer3	Layer4
Probabiilit	0	0	0	0	0	0	0	0	0	0	0	0	
Site recombination	Notation	$P_{e_weak_Rec_V-s}$		$P_{e_high_Rec_V-s}$		$P_{ion_Rec_V-s}$		/					
Reflection on site	Reaction	Layer1	Layer2	Layer3	Layer4	Layer1	Layer2	Layer3	Layer4	Layer1	Layer2	Layer3	Layer4
Probabiilit	0.4	0.3	0.3	0.4	0.35	0.16	0.16	0.35	0.33	0.076	0.076	0.33	
Double Site activation	Notation	$P_{e_weak_Refl_V-s}$		$P_{e_high_Refl_V-s}$		$P_{ion_Refl_V-s}$		/					
Site opening	Reaction	Layer1	Layer2	Layer3	Layer4	Layer1	Layer2	Layer3	Layer4	Layer1	Layer2	Layer3	Layer4
Probabiilit	0.2	0.14	0.14	0.2	0.1	0.07	0.07	0.1	0.02	0.014	0.014	0.02	
Site recombination	Notation	$P_{e_weak_2xAct-s}$		$P_{e_high_2xAct-s}$		$P_{ion_Op_Act-s}$		/					
Reflection on site	Reaction	Layer1	Layer2	Layer3	Layer4	Layer1	Layer2	Layer3	Layer4	Layer1	Layer2	Layer3	Layer4
Probabiilit	0.5	0.7	0.7	0.5	0.6	0.84	0.84	0.6	0.67	0.95	0.95	0.67	
Activated site	Site opening	$P_{e_weak_Op_Act-s}$		$P_{e_high_Op_Act-s}$		$P_{ion_Op_Act-s}$		/					
Site recombination	Reaction	Layer1	Layer2	Layer3	Layer4	Layer1	Layer2	Layer3	Layer4	Layer1	Layer2	Layer3	Layer4
Probabiilit	0.005	0.02	0.02	0.014	0.006	0.03	0.03	0.02	0.01	0.05	0.05	0.035	
Reflection on site	Notation	$P_{e_weak_Rec_Act-s}$		$P_{e_high_Rec_Act-s}$		$P_{ion_Rec_Act-s}$		/					
Site recombination	Reaction	Layer1	Layer2	Layer3	Layer4	Layer1	Layer2	Layer3	Layer4	Layer1	Layer2	Layer3	Layer4
Probabiilit	0.345	0.18	0.18	0.336	0.345	0.095	0.095	0.33	0.319	0	0	0.294	
Activated site	Reflection on site	$P_{e_weak_Refl_Act-s}$		$P_{e_high_Refl_Act-s}$		$P_{ion_Refl_Act-s}$		/					
Site recombination	Reaction	Layer1	Layer2	Layer3	Layer4	Layer1	Layer2	Layer3	Layer4	Layer1	Layer2	Layer3	Layer4
Probabiilit	0.15	0.1	0.1	0.15	0.05	0.035	0.035	0.05	0.001	0	0	0.001	

Furthermore, in the case of air microplasma similar to corona discharges, the electron energy is relatively high as shown in chapter 2. This is why it has been assumed in the present

simulations an electron reflection probability P_{e_Ref} much lower than reflection probabilities of ion and radical.

It is noteworthy that only electrons are assumed playing a role on the site activation due to their high energy (several eV for electrons mean energy: see chapter 2) in comparison to ions, and radicals energies. These latter are close to background gas temperature in the considered air microplasma used for the experimental study of gene transfection [1]. Such hypothesis attributing the main role to the electrons onto cell permeabilization were already evocated in the case of direct plasma exposure [2]. In fact a given super-site, once activated by an electron impact, becomes ready to be opened by the impact of any species which can be either another electron or an ion or a radical. In addition, the probability of recombination of any particle inside a non-activated site is assumed to be slightly higher than the probability of recombination inside an activated site. This choice of probability of recombination is aimed to slightly favor the recombination on non-activated sites in comparison to activated sites.

In the case of radical/super-site and ion/super-site interactions, the predefined reaction probabilities are chosen for these calculations similar since in our low-temperature plasma the energies of ion and neutral species are close to the background gas energy.

Reaction probabilities are $P_{rad_Op_V-s}$ and $P_{ion_Op_V-s}$ (index rad for radicals and ion for ions) for an opening of non-activated site, while $P_{rad_Op_Act-s}$ and $P_{ion_Op_Act-s}$ are those for opening of activated site. $P_{rad_Rec_V-s}$, $P_{ion_Rec_V-s}$, $P_{rad_Rec_Act-s}$, and $P_{ion_Rec_Act-s}$ correspond respectively to particle recombination or neutralization inside non-activated and activated sites while P_{rad_Ref} and P_{ion_Ref} are associated to particle reflection onto the internal walls of the current pore.

The deviation angle distribution during particle reflection is assumed specular ($\theta_p = \text{incidence angle} = \text{reflection angle}$). Moreover, any super-particle can also have the possibility to directly open any site. But for sake of simplification such probability is neglected since it is much lower than probability to open an activated site.

To summarize, once the macro-processes (activation, opening, recombination, and reflection) are defined, the main difficulties are on the good choice of their reaction probability data. As there are no literature data for these probability data, their choice is first based on the following considerations:

- Magnitude of layer density (either protein or lipid layer): For instance, probability of activation or opening process is higher when super-particles interact with super-sites of lower layer density.
- Reflection probabilities of higher energy particles (electrons): it is assumed much lower than those of ions or radicals having lower energy.
- Site activation: only electrons can activate super-sites due to their high energy
- Probability of recombination in non-activated supersite: it is assumed higher than probability of recombination in activated super-site.
- Reaction probabilities of lower energy particles (ions, and radicals): they are assumed equivalent.
- Deviation angle after reflection: it is assumed specular.

As already underlined, the choice of reaction probability data is also based on a parametric study that is also discussed in the following sub-section 4.4.

4.4 Results and discussion

The following results are displayed in graphical views. These graphs show along horizontal axis (x) and vertical axis (y) the pore formation through the membrane layers under the influence of the initial simulation conditions and the considered probabilities of occurrence of each macro-process. The computing times are relatively short. Indeed for N_p of about 1.1×10^6 , the computing time allowing a complete run leading to the generation of 5 pores of about 10 nm diameter, crossing the four membrane layers is approximately equal to 60s. The used processor is Intel (R) Xeon (R) CPU E5-2687W v3 @ 3.10GHz.

4.4.1 Effect of the initial incidence angle of ions, and radicals

First, the effect on the pore formation of the angular distribution of the initial incident angle up at the domain entrance (first meshes of surface of layer 1) is displayed in Figure 4-1 (a–d). We considered two choices of angular distributions in the case of radicals and ions species while the electron Gaussian distribution is kept strongly anisotropic with a very small FWHM. Two ranges of the initial incident angles θ_p were considered in the case of ions, and radicals for two numbers N_p of initial particles corresponding to thin ($N_p = 6 \times 10^5$) and wider pores ($N_p = 1.1 \times 10^6$): $85^\circ < \theta_p < 95^\circ$: anisotropic angular distribution in the forward direction over small angle equal to 10° (Figure 4-1 (a) and (c)) and $0^\circ < \theta_p < 180^\circ$: isotropic distribution on the whole forward direction (0 - 180°) of the plasma fluxes (Figure 4-1(b) and 4.1 (d)).

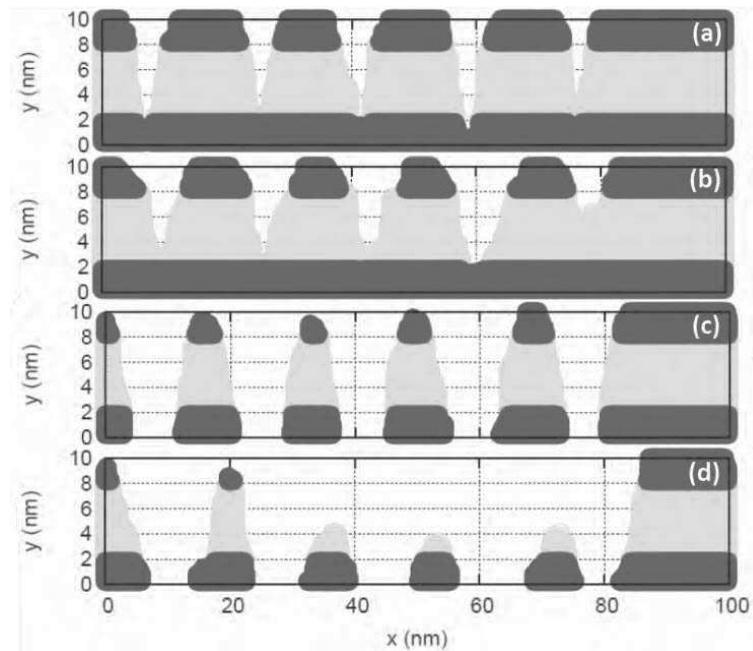


Figure 4-1 Graphical view of the pore formation through the membrane layers illustrating the effect of the initial incidence angle of ions, and radicals for two particle numbers N_p . The other considered data of reaction probabilities are given in Table 4.2. (a) $N_p = 6 \times 10^5$, $85^\circ < \theta_p < 95^\circ$ (forward anisotropic case) with 25% of weak energy, 50% of average energy and 25% of high electron energy distribution, (b) $N_p = 6 \times 10^5$, $0^\circ < \theta_p < 180^\circ$ (forward isotropic case), (c) $N_p = 1.1 \times 10^6$, $85^\circ < \theta_p < 95^\circ$ (anisotropic forward case), (d) $N_p = 1.1 \times 10^6$, $0^\circ < \theta_p < 180^\circ$ (forward isotropic case).

For a given number of particle N_p (see, e.g., either Figure 4-1(a) and 4-1 (b) or 4-1 (c) and 4-1 (d)), the effect of the initial incident angle θ_p , is effective only on the pore width. Indeed, the obtained pores become wider but not deeper for the same initial particle number. We deduced that the angular distribution of initial incidence angle θ_p of plasma incident particle mainly influences the pore width, which is a totally expected result. However, for a better coherence with the air microplasma, we considered in the following simulations an anisotropic distribution of the incident particles $85^\circ < \theta_p < 95^\circ$. The observed effect of N_p variation on the pore formation will be analyzed at the end of this sub-section 4.4. Moreover, we will show some correlation with experimental results on plasma membrane permeabilization for gene transfection.

4.4.2 Effect of electron energy distribution

Figure 4-2 and Figure 4-3 illustrate the role of the electron energy distribution on the pore formation. Knowing that profile of electron energy distribution that initiates and starts all the various interaction processes is specific to each plasma source. Figure 4-2 (a) and 4-2 (b) show the obtained pore when assuming a mono-energetic beam (Figure 4-2 (a)) and an electron distribution having three energy ranges (Figure 4-2 (b)), the proportions of electrons in each range are 25% of weak energy, 50% of average energy, and 25% of high electron energy distribution. Noting that in the case of mono-energetic case, the probabilities of site activation, opening of an activated site, recombination and reflection of both on a non-activated and activated site are equivalent to those used for an average energy electrons.

Furthermore in the case of the three electron energy ranges, the electron probabilities for site activation of a non-activated site $P_{e_Act_V-s}$, double site activation $P_{e_2xAct-s}$, and opening of an activated site $P_{e_Op_Act-s}$ are dependent on each range of electron energy distribution. In other words, the probabilities of process event of site activation and activated site opening are chosen progressively higher from the weak energy range up to the high energy range. This means:

1. $P_{e_weak_Act_V-s} < P_{e_avrg_Act_V-s} < P_{e_high_Act_V-s}$ and $P_{e_weak_2xAct-s} < P_{e_avrg_2xAct-s} < P_{e_high_2xAct-s}$:

For example, in the case of layers 1 and 4, $P_{e_high_Act_V-s}$ is 1.2 times higher than $P_{e_avrg_Act_V-s}$ and 1.6 times higher than $P_{e_weak_Act_V-s}$.

2. $P_{e_weak_Op_Act-s} < P_{e_avrg_Op_Act-s} < P_{e_high_Op_Act-s}$: for example, in the case of layer 1,

$P_{e_high_Act_V-s}$ is 1.8 times higher than $P_{e_avrg_Act_V-s}$ and 2 times higher than $P_{e_weak_Act_V-s}$.

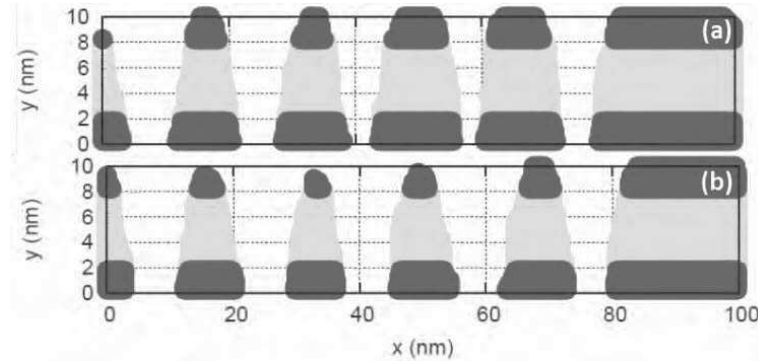


Figure 4-2 Graphical view of the pore formation through the membrane layers illustrating the effect of electron energy distribution for number of particles $N_p=1.1 \times 10^6$, and anisotropic forward scattering of initial ion and radical fluxes: $85^\circ < \theta_p < 95^\circ$. The other considered data of reaction probabilities are given in Table 4-2. (a) mono-energetic electron energy distribution: Noting that $P_{e_Op_V-s} = P_{e_avrg_Op_V-s}$, $P_{e_Rec_V-s} = P_{e_avrg_Rec_V-s}$, $P_{e_Act_V-s} = P_{e_avrg_Act_V-s}$, $P_{e_2xAct-s} = P_{e_avrg_2xAct-s}$, $P_{e_Op_Act-s} = P_{e_avrg_Op_Act-s}$, $P_{e_Rec_Act-s} = P_{e_avrg_Rec_Act-s}$, $P_{e_Refl_V-s} = P_{e_avrg_Refl_V-s}$, $P_{e_Refl_Act-s} = P_{e_avrg_Refl_Act-s}$ (b) 25% of weak energy, 50% of average energy and 25% of high electron energy.

The obtained pores become wider in the case of three different energy regions (Figure 4-2 (b)) when they are compared to those of Figure 4-2 (a) obtained in the case of mono-energetic beam. Further cases of electron energy distributions were also analysed in Figure 4-3 (a–f) that display the pore formation for three different electron energy distributions in the cases of two initial particle numbers $N_p=6 \times 10^5$ (Figure 4-3 (a–c)) and $N_p=1.1 \times 10^6$ (Figure 4-3 (d–f)). When the fraction of electron with a high energy range is chosen two times wider (50% in Figure 4-3(c) and (f)) than the fraction of weak and average energy (25% of weak energy, 25% of average energy distribution), the obtained pores become deeper when we

compare pores of Figure 4-3 (c) to those of Figure 4-3 (a) and 4-3 (b) for $N_p=6 \times 10^5$. Pores become wider when we compare pores of Figure 4.3 (f) to those of Figure 4.3 (d) and Figure 4.3 (e) for $N_p=1.1 \times 10^6$.

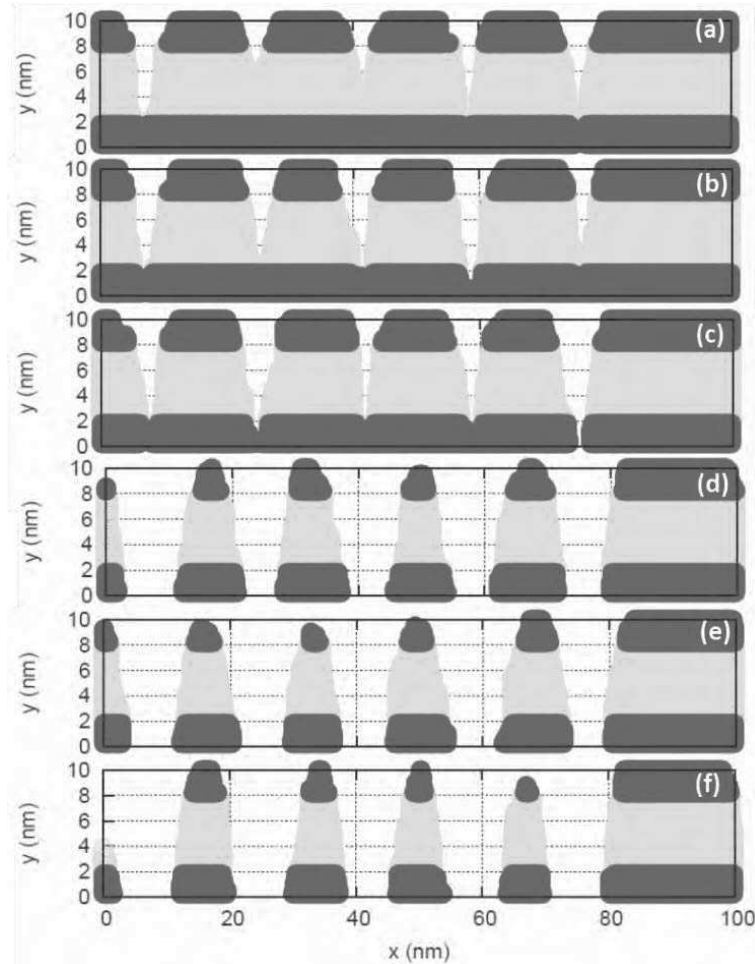


Figure 4-3 Graphical view of the pore formation through the membrane layers illustrating the effect of electron energy distribution for two particle numbers N_p and anisotropic forward scattering of initial ion and radical fluxes: $85^\circ < \theta_p < 95^\circ$. The other considered data of reaction probabilities are given in Table 4-2. (a) $N_p=6 \times 10^5$, 50% of weak energy, 25% of average energy and 25% of high electron energy, (b) $N_p=6 \times 10^5$, 25% of weak energy, 50% of average energy and 25% of high electron energy, (c) $N_p=6 \times 10^5$, 25% of weak energy, 25% of average energy and 50% of high electron energy, (d) $N_p=1.1 \times 10^6$, 50% of weak energy, 25% of average energy and 25% of high electron energy, (e) $N_p=1.1 \times 10^6$, 25% of weak energy, 50% of average energy and 25% of high electron energy, (f) $N_p=1.1 \times 10^6$, 25% of weak energy, 25% of average energy and 50% of high electron energy.

These dependences of the pore formation on the electron energy distribution emphasize the importance of a judicious choice of an electron distribution coherent with the electron energy distribution in air microplasma. Figure 4-4 displays an example of electron energy distribution function calculated using multi-term solution of Boltzmann equation [3] in the case of humid air for the electron mean energy of the streamer head near the cathode plane already shown in Figure 3-7. It is easy to observe that in this real air plasma, the electron distribution is not at all mono-energetic but involves a large distribution of electron of intermediate energy range (bulk distribution) and a smaller part at low and high (tail distribution) energy ranges. This is why the following simulations are performed in the case of an energy distribution with 50% of electrons of intermediate energy range and 25% for the two other energy ranges (low and high). Moreover, the parametric study is also extended to the analysis of the effect of event probabilities of each reaction process, mainly surface processes of reflection and electron opening of an activated site.

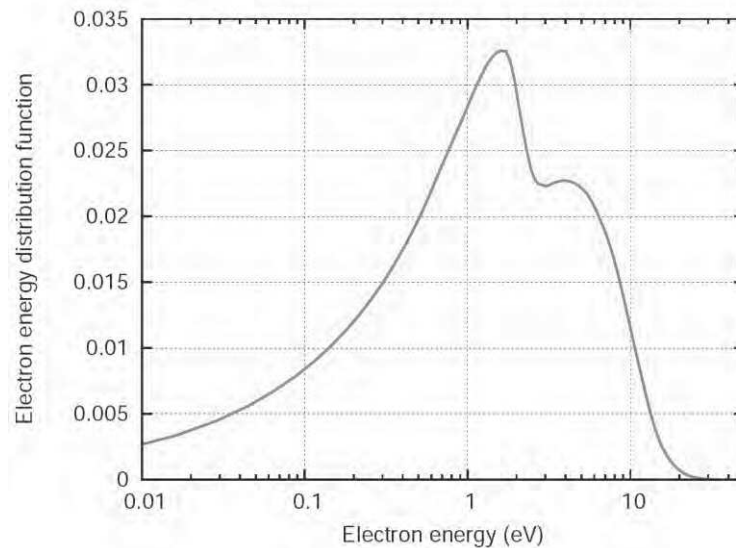


Figure 4-4 Calculated electron energy distribution function from solution of Boltzmann equation [3] in the case of humid air (50% of humidity) for the electron mean energy of the streamer head near the cathode plane.

4.4.3 Effect of the reflection processes in the case of ions, and radicals

As already emphasized, the probability of electron reflection P_{e_Refl} is assumed lower than reflection of ions, and radicals due to the higher electron energy in comparison to energy of ions or radicals. Therefore, only the radical and ion reflection probabilities (P_{rad_Refl} and P_{ion_Refl} respectively) are parameterized. Figure 4-5 (a–d) display the effect of the particle reflection probabilities on the pore formation for two different initial particle numbers $N_p=6 \times 10^5$ (Figure 4-5(a) and 4-5 (b)) and $N_p=1.1 \times 10^6$ (Figure 4-5 (c) and 4-5 (d)). The simulation results clearly underline the role of the reflection probabilities P_{rad_Refl} and P_{ion_Refl} to widen and deepen the pore dimensions.

Indeed, if the reflection probability of the considered particle (ion or radical) becomes higher on the internal walls of the current pore, this particle will diffuse in different directions inside the pore after its impact with the membrane matter. This subsequently contribute to widening and deepening of the current pore. Therefore, in the following simulations we have considered a higher magnitude for the reflection probability of ions or radicals due to their low energy. In addition, ions or radicals are assumed to share with an equiprobable way the occurrence of the different possible reaction processes (reflection or site opening). While the magnitude of their recombination probability is the complement to unit. This is aimed to differentiate between the probability magnitudes on layers 1 and 4 (protein) and layers 2 and 4 (phospholipid) with a probability ratio proportional to the density of the considered layer. In fact, the choice of the collision probability data, that are not available in the literature, is first based on some biophysical evidences already evocated, as for instance, probabilities of activation or opening being higher for the lowest density layer. It is also based on a large parametric study.

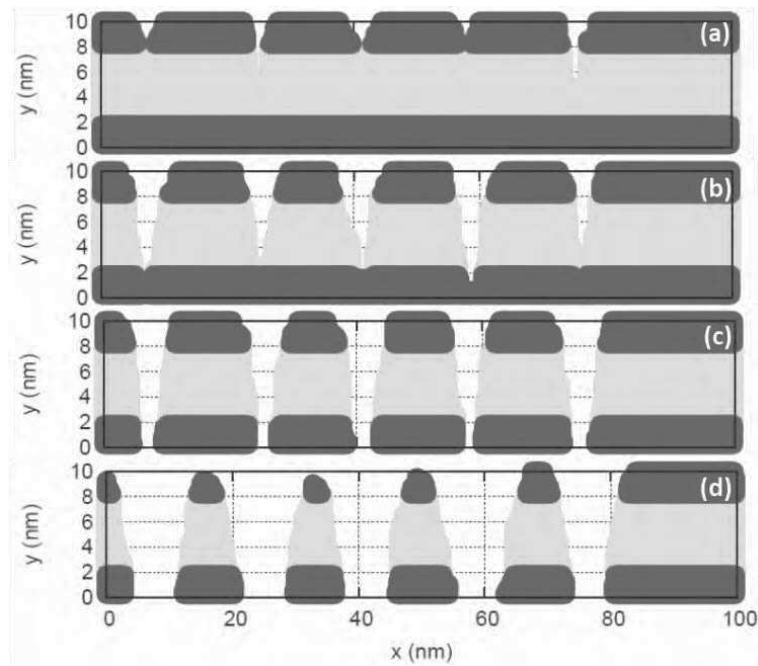


Figure 4-5 Graphical view of the pore formation through the membrane layers illustrating the effect of the reflection processes in the case of ions, and radicals for two particle numbers N_p and anisotropic forward scattering of initial ion and radical particle fluxes: $85^\circ < \theta_p < 95^\circ$. The other considered data of reaction probabilities are given in Table 4-2 except for (a) and (c) where $P_{rad_Refl_V-s} = P_{ion_Refl_V-s} = 0$ and $P_{rad_Refl_Act-s} = P_{ion_Refl_Act-s} = 0$. (a) $N_p = 6 \times 10^5$, 25% of weak energy, 50% of average energy and 25% of high electron energy, (b) $N_p = 6 \times 10^5$, 25% of weak energy, 50% of average energy and 25% of high electron energy, (c) $N_p = 1.1 \times 10^6$, 25% of weak energy, 50% of average energy and 25% of high electron energy, (d) $N_p = 1.1 \times 10^6$, 25% of weak energy, 50% of average energy and 25% of high electron energy.

The probability of each reaction process (activation, opening, recombination and reflection) of each species have been carefully parameterized with the aim to obtain membrane behavior coherent with the measurements representing transfected and surviving cells that will be discussed later. What is very noticeable is the very small range of variation of the probabilities for which it is possible to have coherent results with experimental results.

4.4.4 Role of the processes of electron opening of an activated site

Figure 4-6 (a) and 4-6 (b) show the pore formation without (Figure 4-6 (a)) and with (Figure 4-6 (b)) the effect of electron activated site opening for the same initial particle number $N_p = 1.1 \times 10^6$. In the case of Figure 4-6 (a), we considered only the opening of activated sites by impacts of ions, and radicals. Without the effect of electrons, it is clearly observed in Figure 4-6 (a), the too low width and depth of the obtained pores that for instance cannot allow any DNA transport through the membrane. However, as soon as the electron opening of activated sites is considered, pores become wider and deeper. These simulation results clearly demonstrate that the formation of pores can be accelerated and facilitated due to the action of electrons. This is completely coherent with the magnitude of the considered particle fluxes since in our simulations (see Table 4-1), the electron flux is the dominant one while the ion flux is 2 decades lower than the electron flux and the radical flux 3 decades lower. This is why both in the following simulations and in the previous ones (from Figure 4-1 to Figure 4-7) the opening of activated sites by electron is fully considered in both simulations.

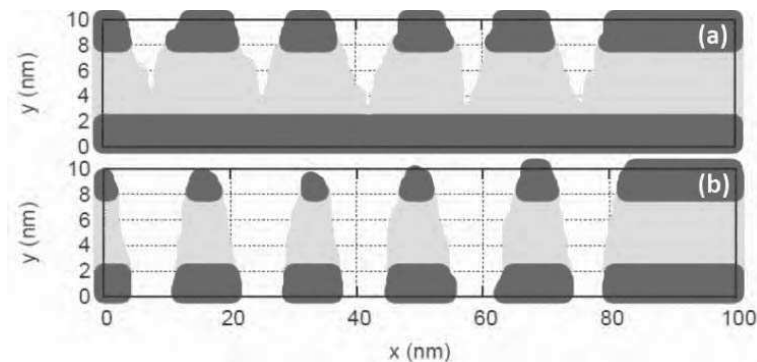


Figure 4-6 Graphical view of the pore formation through the membrane layers illustrating the role of the processes of electron opening of activated sites for particle numbers $N_p = 1.1 \times 10^6$ and anisotropic forward scattering of initial ion and radical particle fluxes: $85^\circ < \theta_p < 95^\circ$. The other considered data of reaction probabilities are given in Table 4-2 except for (a) $P_{e_weak_Op_Act-s} = P_{e_avrg_Op_Act-s} = P_{e_high_Op_Act-s} = 0$. (a) 25% of weak energy, 50% of average energy and 25% of high electron energy, (b) 25% of weak energy, 50% of average energy and 25% of high electron energy.

4.4.5 Effect of the initial particle number N_p

Finally, Figure 4-7 (a–c) emphasize the choice of the initial particle number N_p which varies between 6×10^5 up to 1.4×10^6 , the other parameters concerning probabilities of the different processes were kept the same for the three figures (Figure 4-7 (a–c).)

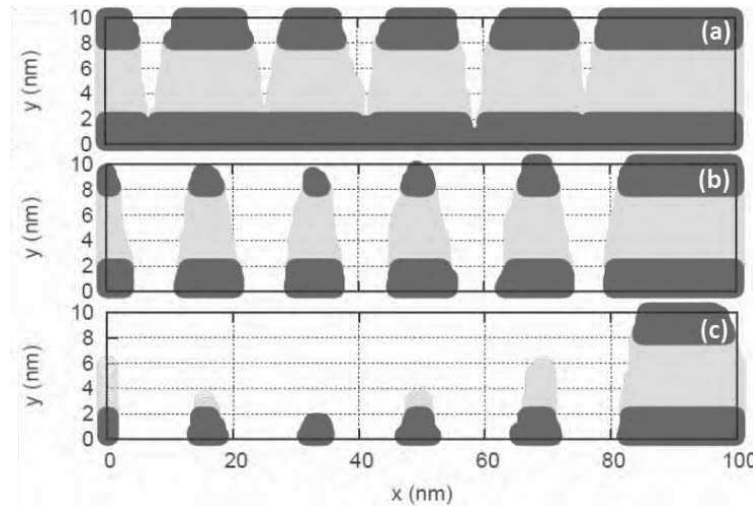


Figure 4-7 Graphical view of the pore formation through the membrane layers illustrating the effect of the initial particle number N_p for an anisotropic forward scattering of initial ion and radical particle fluxes: $85^\circ < \theta_p < 95^\circ$. **(a)** $N_p = 6 \times 10^5$, 25% of weak energy, 50% of average energy and 25% of high electron energy, **(b)** $N_p = 1.1 \times 10^6$, 25% of weak energy, 50% of average energy and 25% of high electron energy, **(c)** $N_p = 1.4 \times 10^6$, 25% of weak energy, 50% of average energy and 25% of high electron energy, Similar used reaction probabilities for the 3 figures, see Table 4-2.

The progressive increase of the depth and width versus the initial particle number N_p is clearly observed. For the smaller N_p (6×10^5), the pore dimensions are too low to allow any DNA transfection through the membrane while for higher N_p (1.4×10^6) the four layers of the membrane are largely removed leading to very wide pores. This latter case certainly corresponds to the cell inactivation or death, since the membrane is quasi-totally perforated and we can easily imagine in that case the cytoplasm effusion outside the cell. For these simulation conditions, the initial particle number can be directly correlated to the exposure time of the cell membrane to the plasma species. For this purpose, an experimental validation study is

conducted. It is based on comparison of the present simulation results of pore formation with measured rates of transfected and surviving cells performed at Ehime University.

The most important obtained results are summarized in the following:

- The angular distribution of initial incidence angle θ_p of ion and radical particle mainly influences the pore width.
- The energetic electrons play the main role on super-site activations and openings due their strong anisotropy in the forward direction.
- The obtained results highlighted the importance to taking into account an electron energy distribution coherent with the used air microplasma for a more realistic estimation of the pore formation.
- The reflection processes due to ions, and radicals, have shown their role to widen and deepen the pore dimension.
- The initial particle number was the most efficient parameter of the membrane poration since the progressive increase of the depth and width versus the initial particle number N_p was clearly observed.

4.5 Experimental validation of the Monte Carlo stochastic simulations of the membrane poration

As already stated, the validation step is based on the comparison of the measured and calculated rates of both surviving and transfected cells versus plasma exposure time used for experiments and particle number N_p used for simulations.

4.5.1 Simulation and experimental conditions

The used simulation conditions were similar to those used in Figure 4-7. The initial particle number N_p was varied from 0.4×10^6 to 1.8×10^6 . The used plasma discharge configuration was previously described in chapter 1, sub-section 1.3.3, and experimentally characterized by OES measurement during the second chapter. The previously system of 96 wells containing the

treated cells was used (see Figure 1-14). The electrical conditions were same as those used in subsection 1.4 (the applied voltage between the electrodes was 14 kV. The output voltage had a 20 kHz sinusoidal waveform which was pulse modulated at 25 Hz with a duty ratio of 1%)

On another hand, the considered cells for gene transfection are L-929 mouse fibroblast cell, which are cultured in the 96 wells. The samples were made by pouring in each well the transfected DNA, which is plasmid pCX-EGFP coded with green fluorescent protein (GFP) with a dilution ratio of 4 $\mu\text{g}/4 \mu\text{L}$. The solution used for cell and DNA immersion is Tris/EDTA (TE) and Phosphate-buffered saline (PBS). The distance from liquid surface of the well to the tip of the microplasma electrode was set to 1 mm. The plasma irradiation duration was varied from 0.05 to 25ms. Moreover, the protocol of gene transfection was the standard one, where both the cells and DNA plasmid are irradiated by the plasma discharge. After plasma treatment, the cells are incubated at 37 °C under 5 % carbon dioxide for 24 hours. Then, observed by fluorescence microscope. Imaging Cytometer method was used for the evaluation of the GFP-expressing cells. As already stated in subsection 1.3.4 of the chapter 1, the average number of living cells (n_l), cells emitting fluorescence (n_f) and the number of cells of the control sample without plasma irradiation (n_0) were counted for 15 wells. Finally, the survival and transfection rates were calculated according to equations (Eq-1-1) and (Eq-1-2) of chapter 1.

4.5.2 Correlation between particle number and plasma irradiation exposure time

The experimental results have shown that when cells are exposed to the micro plasma during a too short time there is not enough gene transfection. While when the exposure or irradiation time is chosen too long, the number of surviving cells decreases rapidly. Figure 4-8 Illustrates such a behaviour since it displays an example of both the surviving cells and the transfected cells versus the irradiation time by using the air microplasma.

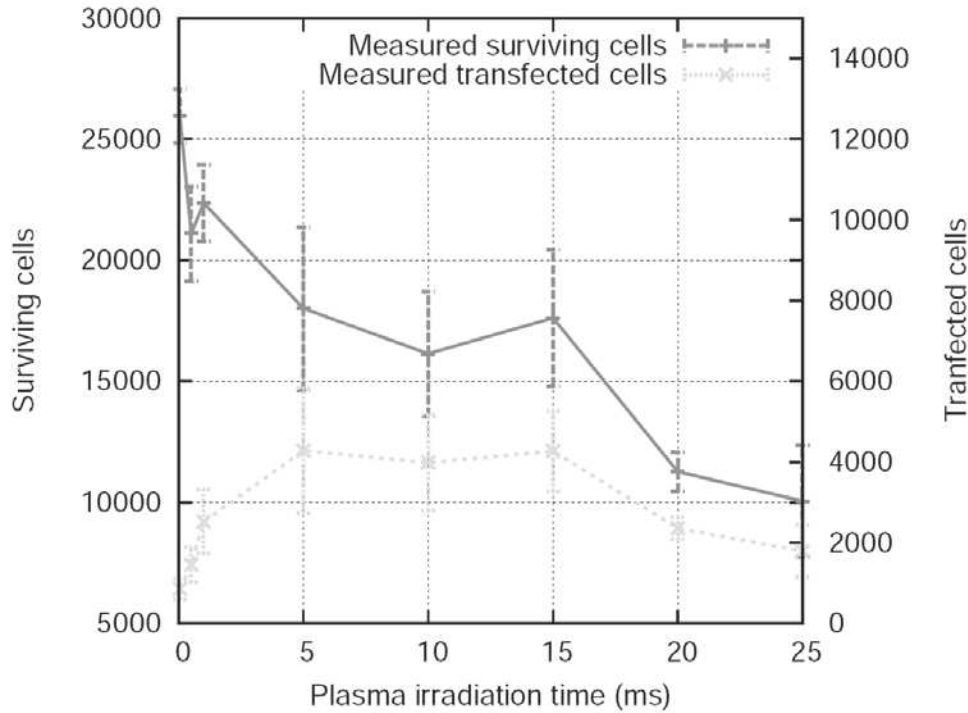


Figure 4-8 Example of measured surviving cells and transfected cells versus irradiation time when using air microplasma.

We can observe that the optimal time of plasma irradiation allowing a good compromise between surviving cells and transfected DNA is around 10 ± 5 ms; this optimal irradiation time is obviously dependent on the experimental conditions, and the microplasma generation (cf. chapter 2). This means that for durations lower than this optimal time, the DNA transfection efficiency is not satisfying while above this optimal time the number of dead cells becomes significant. This what we exactly qualitatively observed from Monte Carlo simulations since if N_p is chosen too low this leads to a pore diameter not large enough to allow any DNA transfer through the formed pore.

On the other hand, if N_p is chosen too high the membrane can be damaged (see Figure 4-7) which normally corresponds to cell death because most part of the membrane is removed. In fact, Monte Carlo simulations of Figure 4-7 showing the pore formation versus particle numbers can be represented differently if we assume that:

1. The rate of surviving cells is proportional to the surface of the remaining membrane (S_{memb}) normalized by the total membrane surface.
2. The rate of transfected cells is proportional to the product of the surfaces of remaining membrane and formed pores (S_{pore}) normalized by the quadratic mean of these two surfaces ($S_{\text{memb}}^2 + S_{\text{pore}}^2$).
3. The optimal transfection corresponds to the case where the pore diameter is close to 10 nm.

Figure 4- displaying these two simulated rates versus the particle number N_p , shows a very interesting qualitative agreement between the measured rates of surviving and transfected cells and the simulated ones. This first successful comparison can be considered as a preliminary validation of the Monte Carlo poration model developed in the present thesis.

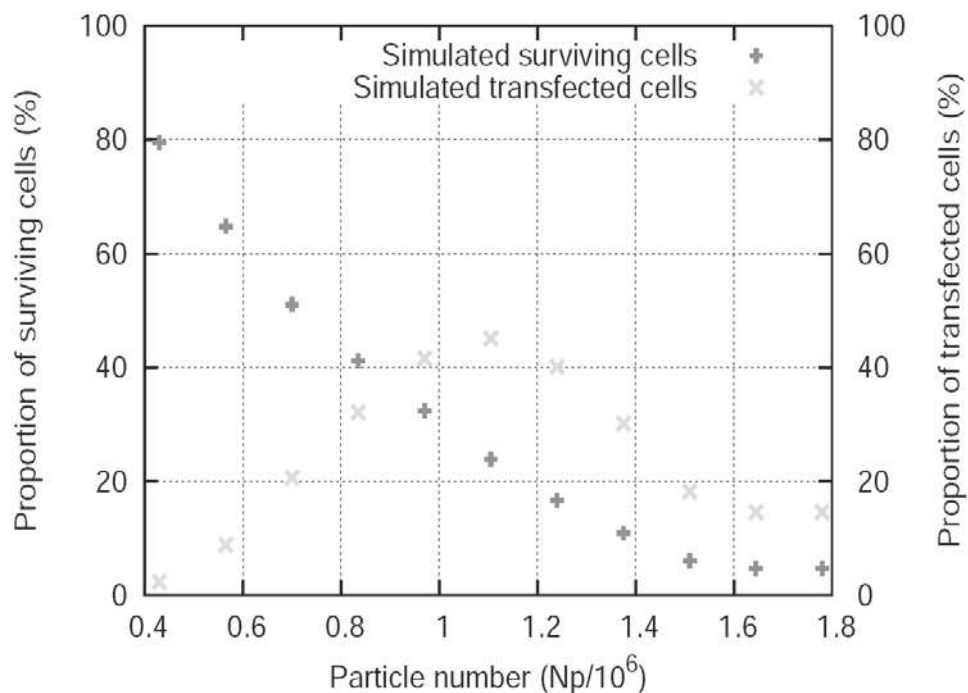


Figure 4-9 Proportion of simulated survived cells and transfected cells versus particle number N_p .

4.6 Conclusion

The operating parameter study conducted during this chapter, enabled to emphasize several important results. First, the strong anisotropy in the forward direction of the incidence angle in the case of energetic electrons and the smoother anisotropy of ions, and radicals (due to their lower energy which is close to background gas temperature), play a non-negligible role on the cell permeabilization and pore formation. Moreover it was also highlighted the importance to taking into account an electron energy distribution coherent with the used air microplasma obtained from solution of multi-term Boltzmann equation for a more realistic estimation of the pore formation. In addition, the parametric variation of event probabilities of the different reaction processes has shown that the pore sizes (width and depth) can be partly controlled by a judicious fit of both the reflection probabilities of ions, and radicals and the electron opening of an activated super-site. We especially underlined the contribution of ion and radical reflection to widen and deepen the pore dimension. Overall, it is more particularly shown that the initial particle number is the most efficient parameter of the membrane poration.

Moreover, we observed a direct correlation between the initial particle number and the exposure time of the cell membrane to the air microplasma. This means that Monte Carlo poration model is an interesting tool of the prediction of the optimal exposure time versus the input data of the low-temperature plasma parameters, the cell membrane structure, and the needed pore sizes. In other words, this optimal time is important to know before plasma gene transfection. Indeed, if this time is too long, cells can be inactivated and if this time is too short the gene transfection rate cannot be efficient. Under our specifically chosen simulation conditions coming from the parametric study, it is shown a dynamics of formation of membrane pores having dimensions compatible for the gene transfection. In other words, the obtained pore width (or diameter) is close to 10 nm. This is coherent with standard diameters generally expected for gene transfection. These results, qualitatively validated from the first comparison

with measured rates of transfected and surviving cells, are therefore very promising for a better understanding of the plasma gene transfection mechanisms.

This stochastic numerical modeling of plasma-induced poration of cell membranes for gene transfection were presented in international conferences [4][5] and [6], and more recently published in *Plasma Processes and Polymer* [7].

4.7 References

- [1] M. Jinno, Y. Ikeda, H. Motomura, Y. Kido, K. Tachibana, and S. Satoh, “The Necessity of Radicals for Gene Transfection by Discharge Plasma Irradiation,” *J. Photopolym. Sci. Technol.*, vol. 27, pp. 399–404, 2014.
- [2] E. Stoffels, Y. Sakiyama, and D. B. Graves, “Cold Atmospheric Plasma : Charged Species and Their Interactions With Cells and Tissues,” vol. 36, pp. 1441–1457, 2008.
- [3] M. Yousfi and M. D. Benabdessadok, “Boltzmann equation analysis of electron-molecule collision cross sections in water vapor and ammonia,” *J. Appl. Phys.*, vol. 80, pp. 6619, 1996.
- [4] A. Zerrouki, M. Yousfi, A. Rhallabi, H. Motomura, and M. Jinno, “Monte Carlo poration model of cell membrane permeabilization for plasma gene transfection,” in *22nd International Symposium on Plasma Chemistry (ISPC)*, 2015.
- [5] A. Zerrouki, M. Yousfi, A. Rhallabi, H. Motomura., and M. Jinno, “Monte Carlo simulation of cell membrane permeabilization by cold plasma,” in *32nd International Conference on Phenomena in Ionized Gases (ICPIG)*, 2015.
- [6] A. Zerrouki, M. Yousfi, A. Rhallabi, H. Motomura, and M. Jinno, “Stochastic simulation and experimental validation of plasma-induced poration of cell membranes for gene transfection,” in *6th International Conference on Plasma Medicine (ICPM)*, 2016.
- [7] A. Zerrouki, M. Yousfi, A. Rhallabi, H. Motomura, and M. Jinno, “Monte Carlo poration model of cell membranes for application to plasma gene transfection,” *Plasma Process. Polym.*, vol. 12, pp. 633–648, 2015.

GENERAL CONCLUSION

The aim of this thesis is to numerically study the mechanisms of plasma-induced membrane permeabilization using the micro-air plasma source successfully used for gene transfection at Ehime University. This aim is achieved by developing, for the first time in literature, a specific Monte Carlo poration model. The latter has been inspired from literature researches in low pressure plasmas used for deep silicon etching and applied to power electronic devices. The present stochastic Monte Carlo model is aimed to simulate at a global (or macro) scale, the pore formation of few nanometre of width through cell multilayer membranes when irradiated by microplasma active species (as electrons, ions, and neutral radicals) generated in ambient air at atmospheric pressure. A comparison of the Monte Carlo obtained results with experimental gene transfection results allows validating the Monte Carlo model.

The first chapter is firstly devoted to a detailed review on the different developed gene transfection methods. For instance, the viral method which is the most commonly used method in clinical research, the chemical transfection methods, widely used in contemporary researches, and the physical transfection methods based on diverse physical tools such as electric or magnetic or acoustic fields to destabilize the cell membrane in order to deliver nucleic acids into the targeted cells. For example, the electroporation regarded as the most widely used physical technology. It is generally based on the application of short pulses of an intense electric field over the cells, allowing the creation of transitory pores through membranes thus allowing nucleic acid to reach the cytoplasm. However, it is proved that each one of these used methods is limited to few experimental systems and can have serious known drawbacks. Moreover, knowing that one of the major difficulties with gene transfection is how to

effectively and safely deliver the genetic material to different cells types, I underlined the main request in gene transfection that is the development of efficient and safe gene delivery method. Therefore, I emphasized to the potentiality of use of non-thermal plasmas generated at atmospheric pressure for the gene transfection applications. An overview on different plasma sources used for gene transfection in literature (Plasma jets or Dielectric barrier discharges using working gas as for instance helium or argon or air) has clearly confirmed that the cold plasma irradiation is effective to gene transfection. Indeed, it is shown that the cells became transiently permeable for DNA plasmid during the plasma exposure. However, the mechanisms leading to membrane permeabilization by to low-temperature plasmas are not well understood. It has been suggested that such mechanisms could be seen as a competition between reactive species and plasma-induced electric field stimulation but provided high enough plasma-induced electric field is present. Anyway, the mechanisms leading to membrane permeabilization during the interactions between plasma species and cell membrane are partly evoked in the literature as twofold mechanisms: cell charging and lipid peroxidation. However, it is also shown, that the plasmas may have unexpected undesirable effects on cells. This clearly means there is a strong demand for a deeper understanding of the mechanisms of plasma-cells interactions. Furthermore, any cold plasma setup used for gene transfection must fulfil various criteria such as the ability to reach the treatment zone by a stable plasma propagation in time and space and to avoid any damage or inactivation of the treated cells. This means that it is important to optimize both the gene transfection efficacy and the rate of surviving cells. To this purpose, the research team of electrical engineering department of Ehime University, developed several types of plasma sources with different designs and configurations (arc plasma discharge using argon carrier gas, atmospheric pressure plasma jet using helium and equipped with 4 jets, dielectric barrier discharge plasma using also helium flow, and last an air microplasma discharge which is a corona discharge). A comparative study between rates of plasmid

transfection and cell viability obtained in the case of each plasma setup shows that the best results (52.5 % of transfection rate and 90.8 % of cell viability rate) are obtained in the case of the air microplasma discharge. These encouraging results were attributed to the potential space and time stability of this air microplasma source in comparison to the other tested plasma sources. Moreover, an experimental parametric study on gene transfection focused on the air microplasma source is conducted at Ehime University. This parametric study is based on different gene transfection protocols. The obtained results from the parametric study showed that the gene transfection occurs effectively only with the presence of two plasma effects (direct and indirect) during the treatment of both DNA plasmid and COS-7 cells by the air microplasma. These obtained results suggest a synergetic relationship between the direct and indirect effect of plasma.

The second chapter is devoted to the experimental characterizations by optical emission spectroscopy OES of the air microplasma used that previously shown the best results for gene transfection. In fact, as already stated, the aim of the present thesis is more precisely to develop and exploit a specific Monte Carlo poration model. This model is aimed to simulate the pore formation when irradiated by the air microplasma discharge fluxes. This developed model requires the prior knowledge of some plasma input data such as the fluxes and the energy of the main plasma species arriving to the cell membrane. This concerns more particularly the knowledge of the density of charged particles (electrons and nitrogen ion N_2^+), and the temperatures of gas T_g and electrons T_e that have been determined using OES in this chapter. The plasma setup is a corona discharge generated in ambient air from the tip of a pulsed high voltage micro-tube placed 2 mm in front of the petri dish containing deionized water and set over a grounded copper plate. The rotational temperature T_{rot} estimated from comparison of synthetic and experimental spectra of OH(A-X) between 306 to 310 nm, N_2^+ (FNS: 0, 0) at 391.4 nm, and N_2 (SPS: 0, 0) at 337nm are respectively equal to 2350K, 2000K, and 700K in the gap

space. This clearly underlines a thermal non-equilibrium of the corresponding excited species generated inside the thin streamer filaments. But, due to the high dilution of these species in the background gas, these high rotational temperatures do not affect the mean gas temperature that remains close to 300K. Moreover, there is practically no rotational temperature variation along the inter-electrode space (z axis) due to the dependence of T_{rot} on mainly the interactions between the heavy particles. Then, N_2^+ (FNS: 0, 0) and N_2^+ (FNS: 1, 1) head bands spectra at 391.4 nm and 388.4 nm allowed to estimate the vibrational temperature T_{vib} . More precisely, T_{vib} was estimated when there is a good agreement both for the intensity ratio $I_{(FNS: 0,0)}/I_{(FNS: 1,1)}$ of measured and calculated spectra and for the rotational bands of measured and calculated spectra of N_2^+ (FNS: 0,0) which depend on T_{rot} . I also used the comparison between the surface covered by the experimental and synthetic spectra that corresponds in fact to the integral of the normalized spectra over the wavelength. The obtained T_{vib} varies between around 3000K near the tip electrode up to about 6500K near the plate. This T_{vib} rise is probably due to the increase of vibration-vibration collision frequency that producing high vibration levels when the micro air plasma gradually crosses the gap from the anodic tip to the grounded plate. Moreover, the electron temperature T_e was estimated from an interesting approach based on the experimental ratio of the closest nitrogen emission spectra of N_2^+ (FNS) at 391.4nm and N_2 (SPS) at 394.3 nm. This is based on one hand a balance equation between creations and losses of excited upper levels of these two UV spectra and on the other hand on the electron impact rates of the creation of these upper levels calculated from a solution of multi-term Boltzmann equation. The solution of this balance equation leads to T_e equal to about 6.75 eV near the anodic tip. Then T_e decreases versus the inter-electrode distance from the tip to the plate. This result is coherent with electron energy in the case of streamer corona discharges in the region close the high voltage tip. Noting that the error bar on electron temperature estimation is equal to about 30%. Then the electron density η_e is estimated from the measured spectrum of $H\alpha$ line. The full width at half maximum

(FWHM) of Stark broadening is extracted from experimental H α spectrum after a prior estimation of instrumental broadening using a standard He-Ne laser, Doppler broadening and collisional broadening using classical relations involving more particularly the known gas temperature T_g . In the case of the present air microplasma, the natural broadening is very small so it was neglected. The obtained electron density n_e equal to about $1 \times 10^{15} \text{cm}^{-3}$ within an average error bar of about 50%, is coherent with the usual magnitude of electron density in the streamer head developed near the tip of corona discharge. Last, the axial variation of the density of molecular nitrogen ion in its background state was also estimated from the experimental ratio of the intensities of the same close wavelength spectra $\text{N}_2^+(\text{FNS: } 0, 0)$ and $\text{N}_2(\text{SPS: } 2, 5)$. This ratio intensity has been correlated to the density of background states ion $\text{N}_2^+(\text{X } ^2\Sigma^+_g)$ and neutral molecule $\text{N}_2(\text{X } ^1\Sigma^+_g)$ assuming a prior knowledge of the excitation temperature T_{ex} . More precisely, the excitation temperature T_{ex} is assumed to be linearly weighted between vibration T_{vib} and electron temperatures T_e . In this case, when assuming a prior estimation of ion density close to 10^{15}cm^{-3} at $z=0 \text{mm}$ based on literature streamer dynamics simulations, the spatial variation of the ion density along z axis has been determined in the whole electrode gap distance within an error bar of about 50%. These present estimations of the spatial variation of the electron n_e and the molecular nitrogen ion densities can be considered as a good order of magnitude. The present experimental air microplasma characteristics are used in the last chapter of the present thesis (Chapter 4) as input data for the exploitation of the Monte Carlo poration model developed in the aim to better understand the mechanisms and the processes involved during plasma gene transfections.

The third chapter was first of all interested in a review on the progress made so far on the numerical modeling of cold plasma interactions with living cells and tissues. I underlined that there are no literature simulations devoted to membrane permeabilization and pore formation when impacted by plasma actives species. However, it is worth noting that several literature

researches based on molecular dynamics MD have been performed to study electroporation of cell membranes at the molecular level. Their goals are to quantitatively model and understand some effects of the high field on biological membranes at the nanosecond time scale. These literature researches were more particularly aimed to better clarify the pore formation process, and possible ionic transports either via nano-pores or through the bio-membrane structure. The obtained results showed that nano-sized pores could typically be formed after a few nanoseconds, with diameters ranging from a few nm to 10nm could be witnessed. However, there are no similar scientific papers based on MD simulation to study the membrane poration during interactions with low-temperature plasma species. The existing literature researches are based on the reactive MD simulations of the interactions between plasma species and bacteria cell surfaces without targeting applications to membrane poration. In fact, these literature researches are devoted to some active plasma chemical species such as O, OH, O₃, H₂O₂ which interact with different types of biomolecules as for instance lipids or DNA or water or peptidoglycan. These reactive MD simulations can give very interesting information about more particularly the bond breaking of the molecular structure following a sequence of bond reorganizations. They are aimed to better understand the inactivation of the bacterial cell surface and subsequently the plasma disinfection mechanisms. Furthermore, these MD simulations need for input data complex reactive force fields without for the moment any relevant link with transient pore creation. Therefore, I developed a specific Monte Carlo poration model based on global or coarse grained concepts involving super-particles colliding super-sites following super-processes. In the framework of this simulation model, each plasma species is assumed as a super-particle grouping a large number of particles. Only three kinds of plasma actives species (electrons, ions and neutral radicals) are considered in order to reduce the complexity of the Monte Carlo poration model at the present stage of its development. However, like a prospect for futures research simulations, various kinds of species can be considered without any change

on the basic concepts of the Monte Carlo model developed in the present thesis. The proportion of these considered plasma species arriving to the membrane and assumed playing a role on the membrane poration are estimated from their fluxes calculated with the help of reaction kinetic model and the OES study conducted in chapter 2. The electron flux (equal to about $2.5 \times 10^{21} \text{ cm}^{-2}/\text{s}$) is the dominant one while the ion flux (about $5 \times 10^{19} \text{ cm}^{-2}/\text{s}$) is about two decades lower than electron flux and the radical flux (close to $5 \times 10^{18} \text{ cm}^{-2}/\text{s}$) three decades lower. The membrane layers were assumed as a simple membrane model superposing four layers of phospholipids and proteins. Moreover, each layer was constituted by a succession of super-sites subjected to specific macro-processes (recombination, reflection, activation of site, opening, etc) during the membrane impacts by the plasma super-particles. It is worth noting that each super-site (or mesh) is numerically defined by a reduced matrix of numbers associated to the state of the mesh before or after the interactions with every plasma species. The different possible states of a given super-site inside a given layer can be for instance non-activated (i.e. virgin) site or activated site or void (i.e. opened) site. The event probabilities of these different processes depend on the considered particle type (electrons or ions or radicals) and also on the layer nature (phospholipid or protein). Moreover, the interactions between super-particles and supersites are treated using predefined reaction probabilities for the different super-processes based on a large parametric study conducted in the last chapter (chapter 4). Before and after each process occurring in a supersite, the entire four nearest super-particle neighbours need to be identified. The Monte Carlo simulation is stopped when the entire considered numbers of each kind of super-particle are treated.

The last chapter (chapter 4) is first devoted to a description of the computational simulation conditions. As for instance, the considered number of initial total super-particles N_p is chosen proportional to the corresponding particle flux estimated from OES spectroscopy measurements (see chapter 2) and kinetic reaction model (see chapter 3). N_p was chosen varying from 7×10^5

to 3.5×10^6 while the information on the flux fractions of ions F_{ion} and radicals F_{rad} relative to electron flux is chosen coherent with the characteristics of the air microplasma. Moreover, the simulation domain geometry was simply represented by a superposition of 4 layers (two external protein layers and two wider internal lipid layers). The sum of the four layer thicknesses is chosen coherent with usual membrane thickness (i.e. 10nm). This simulation domain is discretized into small meshes called super-sites with regular step sizes $\Delta x = \Delta y = 0.25 \text{ nm}$. Each mesh represents a large number of macro-molecules proportional to the density of the real number of molecules of lipids or proteins of the considered layer. As previously emphasized and in the framework of this coarse grained approximation, the interactions are assumed occurring between plasma super-particles and macro-molecules of the different layer meshes. This macroscopic concept does not require a definition of the interactions at the molecular or atomic scale of the membrane. The first interaction of any incident plasma super-particle is with the surface of the layer 1. Thus, in the aim to start the sequences of membrane opening, this surface of layer 1 is uniformly initialized by a fraction of activated sites equal to 10^{-2} . This corresponded in our simulation to 5 activated sites uniformly distributed over the surface of layer 1. Moreover, as previously mentioned, once the super-processes (activation, opening, recombination, and reflection) are defined, the main difficulties are the good choice of the magnitude of their collision probabilities. As there are no literature data for these collision probabilities, their choice is first based on some considerations, as for instance the magnitude of layer density (either protein or lipid layer). Indeed, the probability of activation or opening process is higher when super-particles interact with super-sites of lower layer density. Moreover, the reflection probabilities of energetic electrons is assumed much lower than those of ions or radicals having lower energy. By the way, the reactions probabilities of these lower energy particles (ions, and radicals) are assumed equivalent. Again due to their high energy, only electrons can activate super-sites. In addition, the super-site state is also

considered as a factor determining the choice of reaction probabilities. As an example, the probability of recombination in non-activated supersite is assumed higher than the probability of recombination in activated super-site. For an accurate exploitation of the present Monte Carlo poration model, the estimation of the probability of occurrence of the whole considered macro-processes was also based on a large parametric study. The initial simulation parameters as well as the magnitudes of occurrence probabilities of each reaction processes have been largely parameterized with the aim to characterize their effects on the cell membrane behavior and pore formation. This parametric study enabled to emphasize several important results. First, the effect of the variation of the initial incident angle θ_p of lower energy particles (ions, and radicals) from isotropic ($0^\circ < \theta_p < 180^\circ$) to anisotropic distribution ($85^\circ < \theta_p < 95^\circ$) is effective only on the pore width. Indeed, the obtained pores become wider but not deeper for the same initial particle number. Thus, the angular distribution of initial incidence angle of ion and radical particle mainly influences the pore width, which is a totally expected result. However, for a better coherence with the air microplasma, I considered an anisotropic distribution of the incident particles $85^\circ < \theta_p < 95^\circ$. In addition, energetic electrons play a main role on super-site activations and openings due their strong anisotropy in the forward direction. Indeed, the obtained simulation results clearly demonstrate that the formation of pores can be accelerated and facilitated due to the action of electrons. However, it was highlighted the importance to taking into account an electron energy distribution coherent with the used air microplasma for a more realistic estimation of the pore formation. Thus, the electron energy distribution function was calculated using multi-term solution of Boltzmann equation in the case of humid air. I showed that in this real air plasma, the electron distribution is not at all mono-energetic but involves a large distribution of electron of intermediate energy range and a smaller part at low and high energy ranges. This is why it was assumed an energy distribution with 50% of electrons of intermediate energy range and 25% for the two other energy ranges (low and high).

Furthermore in the case of the three electron energy ranges, the probabilities of process event are chosen progressively higher from the weak energy range up to the high energy range. In addition, due to their lower energy close to background gas, reflection processes due to ions, and radicals have shown their role to widen and deepen the pore dimension. Overall, it was more particularly shown that the initial particle number was the most efficient parameter of the membrane poration. Beyond all, the progressive increase of the depth and width versus the initial particle number N_p was clearly observed. For the smaller N_p (6×10^5), the pore dimensions were too low to allow the gene transfection, while for higher N_p (1.4×10^6) the four layers of the membrane are largely removed leading to very wide pores. This latter case certainly corresponds to the cell inactivation or death, since the membrane is quasi-totally perforated. For these simulation conditions, the initial particle number can be directly correlated to the exposure time of the cell membrane to the plasma species. This means that Monte Carlo poration model is an interesting tool for the prediction of the optimal exposure time versus the input data of the low-temperature plasma parameters, the cell membrane structure, and the needed pore sizes. Precisely, the present Monte Carlo simulation results are qualitatively validated from a first comparison with the measured transfected rate of DNA plasmid and the surviving cell rate in the case of mouse fibroblast cells. The experimental results have shown that when cells are exposed to the microplasma during a too short time there is not enough gene transfection. While when the exposure or irradiation time is chosen too long, the number of surviving cells decreases rapidly. This what it is exactly qualitatively observed from Monte Carlo simulations since if N_p is chosen too low this leads to a pore diameter not large enough to allow any DNA transfer through the formed pore. On the other hand, if N_p is chosen too high the membrane can be quasi-totally damaged. The present Monte Carlo poration method successfully validated, is therefore, a very promising tool for a better understanding of the plasma gene transfection mechanisms. Under the present specific chosen simulation conditions

coming from the parametric study, it is shown a dynamics of formation of membrane pores having dimensions compatible for the gene transfection. In other words, the obtained pore width (or diameter) is close to 10 nm. This is coherent with standard diameters generally expected for gene transfection. Moreover, the most noticeable and encouraging from this parametric study is the small range of variation of the initial parameters and occurrence of probabilities for which it is possible to have coherent results with experimental ones.

Last, after this successful implementation and validation of the Monte Carlo poration model developed in the present research work, it would be interesting to consider as future developments and perspectives:

- A more complex structure of the membrane in order to be closer to biological membranes with for instance a bilayer phospholipid shape involving scaffold protein.
- It is investigated in the present work as a primary step only the direct effect of active air microplasma species. However, the cells are bombarded by various active species either directly produced by the plasma, or indirectly produced by species interactions with the liquid medium before to reach the cell membranes. In other words, the gaseous plasma species when impacting liquid can be transformed in aqueous by-products that in turn interact with the membrane. In addition, the obtained results at Ehime University presented in the first chapter suggested a synergetic relationship between the direct and indirect effect on pore formation and by the way on plasma gene transfection. Moreover, the bio-structures are usually surrounded by a liquid phase. Thus, it would be interesting to consider the membrane poration by interactions with both gaseous species and aqueous species. To reach this step, further optimizations of the developed Monte Carlo model are needed by considering further bio-physicochemical processes but without any change to the basic algorithm and the basic concepts of the model described in the third chapter of this thesis.

- A further experimental validation step could be conducted using comparisons between Monte Carlo simulations of membrane poration and experimental nano-morphology of plasma permeabilized cells using atomic force microscopy experiments.